Numerical modeling to understand the heart

Mark Potse

Habilitation à diriger des recherches

au titre de l'école doctorale Mathématiques et Informatique
de l'Université de Bordeaux

par

Mark POTSE

Numerical modeling to understand the heart

Soutenue le 12 juillet 2024 devant le jury composé de

M. Yves Coudière	Université de Bordeaux	président du jury
M. Rodolphe Turpault	Université de Bordeaux	rapporteur
M. Olivier Bernus	Université de Bordeaux	examinateur
M. François Pellegrini	Université de Bordeaux	examinateur
M. Maxime Sermesant	Inria Sophia-Antipolis	rapporteur
Mme. Maria Guillem	Universidad Politécnica de Valencia	rapporteuse
Mme. Blanca Rodríguez	University of Oxford	examinatrice
M. Ruben Coronel	University of Amsterdam	examinateur
M. Sasha Panfilov	Ghent University	examinateur
Mme. Larissa Fabritz	University of Birmingham	examinatrice

Contents

Résumé

Les maladies cardio-vasculaires sont la première cause de décès dans le monde [230] et la moitié de ces décès sont dus à des arythmies, des dysfonctionnements de la synchronisation électrique du cœur [3]. Derrière cette synchronisation se cache un système très complexe de macromolécules servant de canaux, pompes, et échangeurs ioniques, présents par centaines de milliers dans les membranes externes et internes de chaque cellule musculaire cardiaque. Pour les chercheurs qui la pratiquent il est évident que la modélisation numérique est nécessaire pour comprendre ce système et ses anomalies [141], mais ce sentiment n'est pas partagé par tous les chercheurs dans le domaine de la cardiologie. En revanche, les chercheurs habitués du calcul, et particulièrement du calcul intensif, ne soupçonnent peut-être pas que la cardiologie est un domaine d'application riche et intéressant, et en fait si exigeant que les supercalculateurs et logiciels actuels ne répondent que très partiellement à ces besoins.

C'est pour tous ces chercheurs que ce mémoire discute, dans un premier temps, comment le fonctionnement électrique du cœur est capturé en modèles mathématiques (chapitre 1), et dans un deuxième temps comment la simulation de ces modèles peut aider la recherche en cardiologie.

On peut constater d'abord que les travaux en modélisation cardiaque portent souvent sur des modèles numériques. Sans prétendre à une utilité directe pour les patients, ces travaux répondent à des besoins pratiques, voire à une curiosité scientifique dans le domaine des mathématiques appliquées. Ces études peuvent, par exemple, démontrer qu'un modèle complexe et gourmand en ressources, peut être remplacé par un modèle plus simple. Le chapitre 2 est dédié à la démonstration que les simulations dites « bidomaines » d'un cœur humain peuvent presque toujours être remplacés par des simulations « monodomaines ».

Les modèles numériques peuvent aussi être utiles pour illustrer ce que les théories (physiques et physiologiques) prédisent dans une situation particulière. Ces prédictions sont nécessaires afin de confronter les prédictions à des observations, permettant de réfuter ou corroborer les théories. C'est ce qu'exemplifie le chapitre 4, reproduisant un extrait d'une étude qui rejette l'hypothèse selon laquelle une insuffisance des canaux sodiques du cœur cause une anomalie de l'électrocardiogramme liée au syndrome de Brugada.

Si la théorie a une crédibilité suffisante, les simulations peuvent aussi avoir une valeur éducative. Le chapitre 3 montre ainsi comment l'instant de la repolarisation cardiaque (le retour au repos des cellules après une excitation) ne peut être établi d'un signal électrique que s'il est mesuré directement sur le muscle cardiaque.

Enfin, les modèle numériques peuvent être générateurs d'hypothèses, surtout quand celles-ci ne semblent pas reproduire les observations. Le plus souvent cela implique que le modèle est incorrect, mais le chapitre 5 montre qu'il est aussi possible que les observations ne soient pas assez précises, ce que l'on n'aurait pas soupçonné sans avoir essayé de les reproduire numériquement.

Le mémoire conclut avec une brève exploration des perspectives, notamment le début de la modélisation du cœur comme un ensemble de cellules modélisées individuellement, ce qui permettrait de mieux comprendre les maladies électriques liées aux anomalies structurelles du muscle cardiaque, mais nécessite aussi des collaborations interdisciplinaires et des avancées méthodologiques pour résoudre et même exprimer, numériquement, ces modèles.

Chapter 1

Introduction

Heart disease is one of the two most important causes of death [230]. About half of these deaths are caused by malfunctioning of the electrical activation system that serves to synchronize the contraction of the heart [3]. This system consists of many different types of molecular-scale ion channels, pumps, and exchangers which generate repetitive changes in ion concentrations in the cell and its interior organelles. These changes govern the cell's contraction but also propagate rapidly from one cell to another through intercellular connections, allowing the cells to synchronize their contraction. Pathologies that affect this intricate system can result in life-threatening arrhythmia: situations where the cardiac activation is disorganized and the contraction becomes ineffective. The study of normal and abnormal physiological mechanisms of cardiac electrophysiology and the diagnosis and treatment of its diseases form a vast domain of research with immediate impact on society. Due to the complexity of the system and its emergent behaviours, this research benefits greatly from numerical modeling. Numerical models can contribute to research in different ways, and this text exemplifies four of them, in each of the following chapters.

Before we discuss the role of numerical models in cardiac electrophysiology, it is necessary to give a brief overview of the physiological system itself and the numerical models that have been conceived to represent it. This introduction is provided in the following two sections.

1.1 Cardiac electrophysiology

Almost all biological cells are electrically active [87]. This means that they generate a variable difference in electric potential across membranes, which can be their outer membrane as well as those of intracellular organelles. Most of these cells generate *action potentials*, transient changes in the transmembrane voltage of the cell. The goal of an action potential is usually to open calcium-specific channels in the whole membrane at once to let a wave of calcium ions enter the cell. This calcium then triggers a specific behaviour, such as the contraction of a muscle cell.

The mechanisms behind this electrical activity are bewilderingly complex. Research performed in the second half of the 20th century has shown that each electrically active cell is equipped with about a million ion channels and pumps in its outer

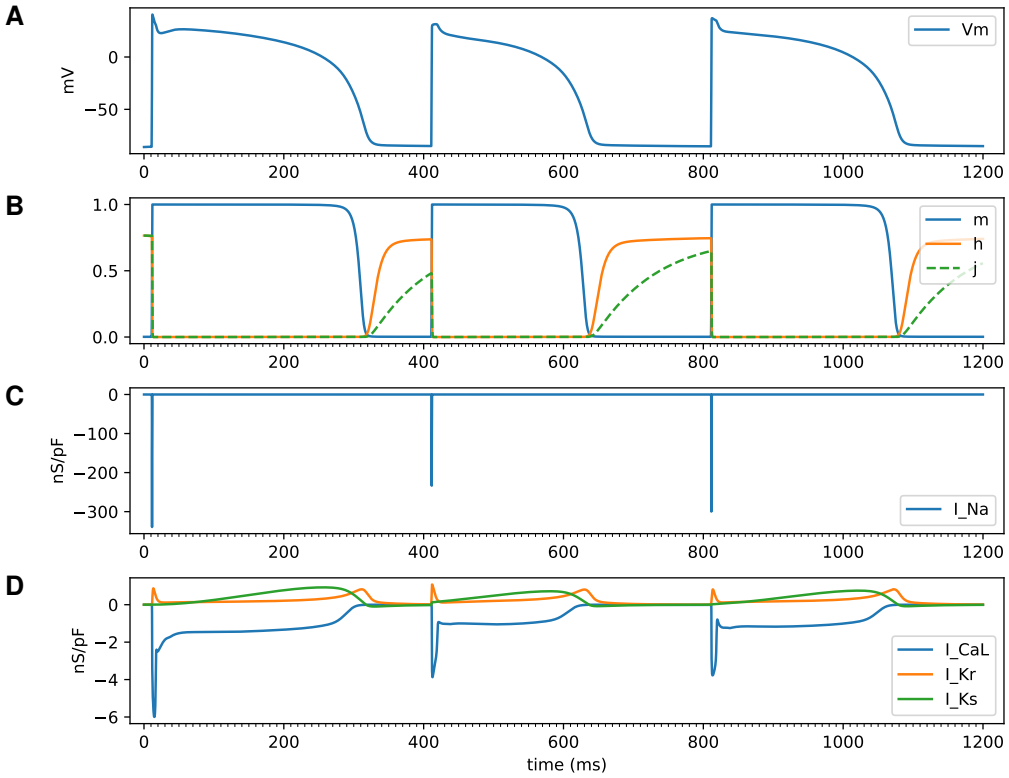

Figure 1.1: *Membrane dynamics of a single cardiac cell. **A:** Transmembrane potential. The cell is paced at 10 ms and then relatively quickly again, at 410 ms. This causes the second action potential (AP) to be smaller and shorter, while the third AP is partially recovered. **B:** The AP changes are explained by the behaviour of the gating variables of the ion channels. Here the three variables of the fast sodium current are shown. We can see that the inactivation variable j has not yet returned to its initial value when the second stimulus comes. **C:** This results in a smaller sodium current, reducing the peak amplitude of the second AP. **D:** Similar effects are visible in the L-type calcium current (I_{CaL}), which maintains the action potential plateau, and the repolarizing currents; the smaller I_{CaL} contributes to a shorter AP.*

membrane alone, and that there are dozens of different types of these channels. These channels open and close in a stochastic way with probabilities and time constants that depend on transmembrane voltage, concentration differences, and various messenger molecules. Through voltage and concentrations, channels influence each other's behaviour. Because of this complexity, numerical modeling has played an important role in the development of our understanding of these systems, and indeed in the prediction of new channel types [141].

The first mathematical model of the electrical behaviour of a cell, c.q. a neuron, was published in 1952 by Hodgkin and Huxley [91], who were later awarded a Nobel prize for their work. In the following decades, models have been gradually refined and have been developed for many other cell types, such as those of the heart [19, 124, 206].

Figure 1.1 illustrates the electrical activity of a human heart muscle cell (cardiomyocyte) as simulated with a physiologically realistic model [206].

The heart has the particularity that its muscle cells are all connected electrically to

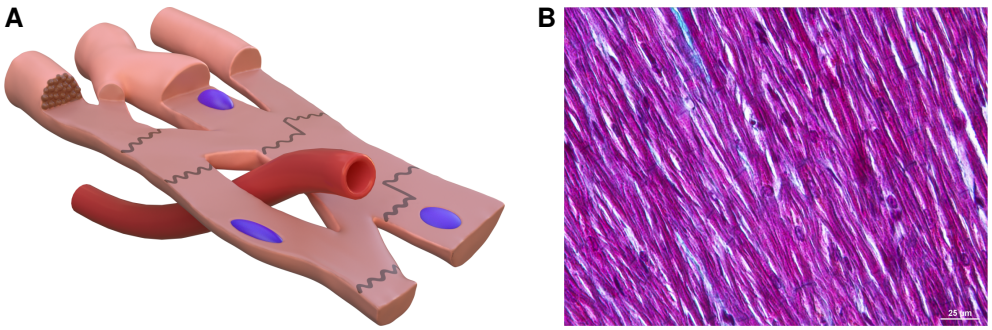

Figure 1.2: ***A:*** *Artist's impression of the cardiac tissue structure on the cellular level; the cells form a network of branching and converging fibers, divided into cells in a seemingly random fashion.* ***B:*** *Microscopic view of the tissue demonstrating how the muscle fibers (purple) are separated at different scales by collagen sheets (white). In diseased tissues these separations grow and transverse connections are lost. Image courtesy of Dr. David Benoist, IHU Liryc.*

their neigbours, by small channels named *gap juctions*. Due to this coupling, together with a self-reinforcing activation mechanism, the activation of the cells can be synchronized to achieve a highly efficient contraction of the heart. However, diseases affecting the gap junctions or the ion channels of the heart can disturb this propagating activation, causing it to run in circles and to make the contraction of the muscle ineffective. Such *cardiac arrhythmia* can lead to death within seconds.

1.2 Numerical models of cardiac electrophysiology

Numerical models of the electrophysiology of the heart aim to reproduce the electrical activity of the cells, its propagation through the muscle, the mechanisms by which this propagation can deteriorate into arrhythmia, and the measurable electrical signals that it produces inside the heart and on the body surface.

Almost all current work in cardiac electrophysiology is based on a continuum approximation called the bidomain model [131, 213]. It approximates the network of interconnected muscle cells embedded in an extracellular matrix and other structures such as fibroblasts and capillaries as two co-located spaces: the intracellular domain, to represent the interior of the cells and the gap junctions that connect them, and the extracellular domain, to represent everything else.

The two domains are characterized by conductivity tensors G_i and G_e, respectively. Their values at each point in the model depend on the fiber direction and account for the partial volume occupation of the two domains. In addition the parameters C_m and β determine the capacitance of the cell membrane and the amount of membrane per unit volume, respectively. The state variables of the model are the potential fields ϕ_i in the intracellular and ϕ_e in the extracellular domain, and a set of variables $\vec{y}$ describing the state of the membrane molecules at each location. Using the auxiliary variable $V_\mathrm{m} = \phi_\mathrm{i} - \phi_\mathrm{e}$ and agreeing that all variables are functions of time and position we can express the bidomain model compactly as

$$\beta^{-1}\nabla\cdot(G_\mathrm{i}\nabla\phi_\mathrm{i}) = C_\mathrm{m}\partial_t V_\mathrm{m} + I_\mathrm{ion}(V_\mathrm{m},\vec{y}) \quad (1.1)$$

$$-\beta^{-1}\nabla\cdot(G_\mathrm{e}\nabla\phi_\mathrm{e}) = C_\mathrm{m}\partial_t V_\mathrm{m} + I_\mathrm{ion}(V_\mathrm{m},\vec{y}) \quad (1.2)$$

$$\partial_t\vec{y} = F(V_\mathrm{m},\vec{y}) \quad (1.3)$$

where the term $C_m \partial_t V_m$ represents the capacitive transmembrane current, the function I_{ion} the density of ionic current flowing between the two domains, and F is a nonlinear vector-valued function describing how the membrane state evolves.

simulating the electrical activity of the heart

The electrical activity of the heart can be simulated by integrating Equation 1.1, Equation 1.2, and Equation 1.3 [221]. This is known as a bidomain reaction-diffusion model. In most of my work a simplified version, a "monodomain" reaction-diffusion model, is used. This model can be derived by assuming that G_i and G_e are proportional [114]. Although this is a gross simplification the effect of this assumption is negligible for most purposes if the model parameters are well chosen [27,52,140,168]. The monodomain model reads

$$\begin{cases} C_m \partial_t V_m = \beta^{-1} \nabla \cdot (G_m \nabla V_m) - I_{ion}(V_m, \vec{y}) \\ \partial_t \vec{y} = F(V_m, \vec{y}) \end{cases} \tag{1.4}$$

where $G_m = G_i G_e / (G_i + G_e)$. With this choice of G_m a monodomain model reproduces a bidomain model very accurately [168].

simulating measurable signals

The potentials ϕ_i and ϕ_e are absolute potentials, which the equations define only upto an arbitrary offset. Differences in ϕ_e between different locations can of course be readily measured. The difference signal between a location in or near the heart and a location far from the heart is practically useful [54,199], and is named a "unipolar" cardiac electrogram (UEG). Differences between closely separated sites in the heart can be useful too and are named "bipolar" electrograms.

The most commonly measured cardiac electric signal, however, is the electrocardiogram (ECG), which measures potential differences between different locations on the skin. The ECG was developed in the early 20th century, when electric amplifiers did not exist yet, and some of the conventions that developed around it result from practical considerations that are no longer relevant today. The ECG that a physician typically sees has 12 traces, representing difference signals between a positive and a negative terminal, where the negative terminal is in most cases an average over two or three electrodes. Thus, an ECG potential $V(t)$ at time t is, more generally, a linear combination $V(t) = \sum_i c_i \phi_e^i$ where c_i are the relative contributions of the two or more electrodes and ϕ_e^i are the potentials at the corresponding positions. The coefficients c_i must fulfill charge conservation, $\sum c_i = 0$.

When a bidomain model is integrated, ϕ_e is one of the variables, but in the (more commonly used) monodomain model it is not. In that case it can be computed by combining Equation 1.1 and Equation 1.2 to yield

$$\nabla \cdot ((G_i + G_e) \nabla \phi_e) = -\nabla \cdot (G_i \nabla V_m). \tag{1.5}$$

This equation can be solved for ϕ_e from a given distribution of V_m. If potentials at few locations are needed, as in a standard ECG, this can be done very efficiently with Green's functions [161], also called "lead fields" in the community.

In Figure 1.3 the various cardiac signals are illustrated.

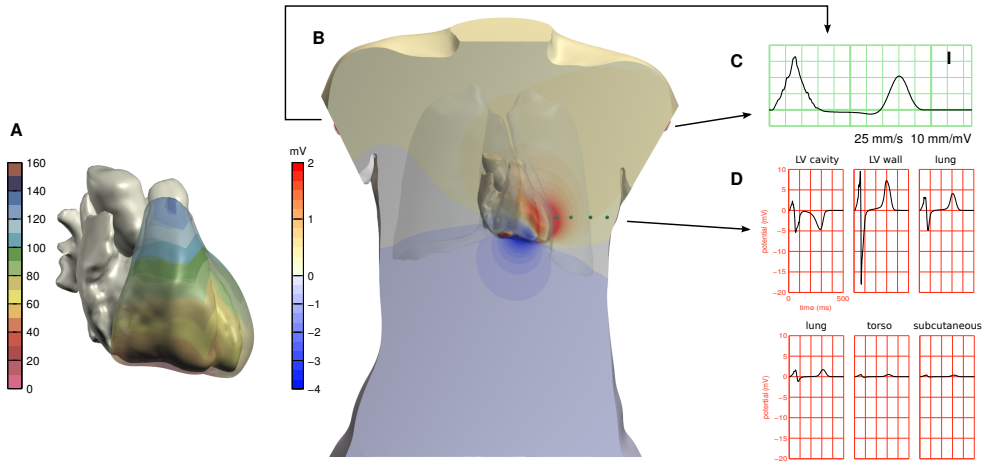

Figure 1.3: *Overview of cardiac electric signals that can be captured at various positions in the body.* ***A:*** *Simulated activation sequence in a human heart model; the scale is in milliseconds.* ***B:*** *Full-torso solution for ϕ_e computed by solving Equation 1.5, 40 ms after the start of the simulation, shown in a cross section of the torso and on the surface of the cardiac cavities.* ***C:*** *Standard ECG lead I, which is measured between electrodes placed on both arms, from the same simulation.* ***D:*** *ϕ_e at 6 positions in the cross-sectional plane of panel B. The first position was inside the left ventricular cavity and the second in the left-ventricular free wall. The other four are marked with green spheres. These potentials are referenced against Wilson's central terminal (the average potential of the three limb electrodes).*

high-performance computing

My work concentrates on modeling of the whole human heart and accurate simulation of the ECG. The main numerical challenges for this work result from the complexity of the function F and the high spatial resolution that is required to model these systems, which leads to model sizes in the order of 10 million to 100 million nodes or elements. This makes solutions of Equation 1.5 hard to obtain, and integration of the reaction-diffusion system numerically expensive. Most of my work is therefore done on tier-1 high-performance computing systems.

1.3 The role of numerical modeling in cardiac electrophysiology research

Ever since the Englightenment it has been common to believe that all of nature is governed by a few simple rules. Physicists such as me like to believe that the same rules that flung a trillion searing galaxies spinning into the void also allow the heart to beat and we tend to ignore how useless this proposition seems to a physician who faces the complexity and the unpredictable suffering of patients every day. Yet, despite the complexity, much of what happens in the heart can indeed be described very well by the "laws of physics," and it is this very complexity that necessitates numerical models. Mathematical models are needed when we apply the laws to a particular situation, and when this situation becomes a little complex, the models become "numerical," meaning that we cannot find exact solutions but only approximate ones, and often at great computational cost. It is with the doubtful physician in

mind that I describe here a few ways in which numerical models can help cardiology research.

1.4 Models to learn about models

Many cardiac modeling studies concern models, just like clinical studies concern clinical events. Such studies have little "collateral damage," as one of my dearest colleagues proposed to call it (others call it clinical impact), but are practically important. These studies demonstrate, for example, how models can be simplified without losing accuracy, or what emergent phenomena they are capable of [45, 223]. In the context of the MICROCARD project, our colleagues at the University of Strasbourg are investigating how detailed numerical models of cardiac membrane dynamics can be transformed automatically to better utilize the resources of specific CPUs, making simulations faster and less energy-consuming [207, 209].

When I had built the first code able to run bidomain (Equation 1.1, 1.2, and 1.3) simulations of a whole human heart, our first occupation was to show that for most purposes a monodomain model (Equation 1.4) is good enough (Chapter 2). Several other studies have investigated refinements of the monodomain model to make it work even more closely like a bidomain model, without increasing the computational cost [27, 28, 52].

1.5 Models to illustrate theory

Models are necessary to show what a theory predicts in a particular situation. Such predictions can then be compared to experimental results, to refute or corroborate the theory, but can also be valuable in their own right of one wishes to believe that the theory is good enough for the purpose and the assumptions in the model are justified.

Such is the case, for example, in my work on a simple model for the "unipolar" electrogram (UEG), a signal measured with the positive electrode touching the heart muscle and the negative electrode far away from it (Chapter 3). The simple model states that the UEG is essentially an upside-down transmembrane potential (as measured between the inside and the outside of the cell membrane) added to a lower-frequency "remote component" that represents the activity of the whole heart. This model was validated by comparing it to a bidomain model, using a realistic human cardiac geometry.

This simple model has likely helped to settle the debate about repolarization measurements in UEGS. While all researchers in cardiac electrophysiology would agree that local depolarization (upstroke of the transmembrane potential) is seen as a downstroke in the UEG, it was not universally acknowledged that local repolarization would correspond to a rising slope. Some researchers claimed that when the repolarization wave in the UEG is positive, the timing of its final, downward slope should be measured. The simple model shows that there is no reason to think so – an inference that would be hard to make from the complexity of a bidomain model.

At the same time the study showed that there was indeed in some situations a correlation between a downward slope in the signal and the local repolarization, as some

experimentalists had found. This less intuitive observation could be explained as resulting from an interaction between the local and global components in the UEG. The simulations also clearly showed that there was a correlation, but not a coincidence: repolarization times measured in this way could be off by over a hundred milliseconds, and would be strongly influenced by remote events.

Others have later noted that the remote component can be explained more accurately using lead-field theory, and that its dependence on electrode location does introduce important measurement bias [228]. The remote component can be calculated in the same way as an ECG lead, so one could see the UEG as an ECG with a local component. A variant of the simple model has even been tested in human open-chest experiments [143].

1.6 Models to falsify

The epistemiologically purest way in which a model can be used is to falsify a theory. Noble and Rudy explained how models of cardiac membrane dynamics have repeatedly shown that they could not reproduce all measured phenomena, each time leading to a search for the missing components, and their discovery [141].

My work presented in Chapter 4 falsified the theory that a reduction in the abundance or functionality of sodium channels (the main drivers of cardiac depolarization) can explain the ECG phenotype of Brugada syndrome. Simulations showed that such reductions only led to wider QRS complexes, and that the Brugada phenotype could only be reproduced when tissue damage (cardiomyopathy) was present as well. These predictions were supported by experimental [97] and clinical evidence [64].

1.7 Models that generate hypotheses

Even the toughest skeptics of models would probably not deny that models can be used to arrive at hypotheses. Every way to arrive at a hypothesis is legitimate, although not all are legal under every jurisdiction, and one could hardly object to some mathematics and computers. A well-known example in cardiology is the dog-bone shape of "virtual cathodes," predicted by theory before it was observed in experiments [229].

An example from my own work motivated the study reproduced in Chapter 5. We had been trying to reproduce ECG P waves, the waves generated by atrial depolarization, using a human heart-torso model, and observed that the waves always had complex shapes. We initially believed that this was not in agreement with reality, because P waves are always represented as very simple shapes, or printed so small that their shape cannot be discerned, so that with the simple textbook figures in mind one would always observe a simple shape. We tried several modifications in the anatomy and physiology of the model to obtain simpler waves, but even with spherical atria we did not succeed, as we had to allow for some undeniable openings in the spheres. Finally we began to doubt the observations instead of the model, and decided to study P waves in healthy volunteers with very high accuracy, using

high-quality recordings and carefully designed signal-averaging methods. The results showed that P waves are indeed complex and, interestingly, no less complex in young subjects than in older ones.

This in turn led me to the hypothesis that when P-wave complexity cannot be observed in a carefully measured and averaged ECG, it is because the signals differ from beat to beat – making a smooth P wave a signal of disease rather than health. Unfortunately I have not been able to investigate this hypothesis myself but there is suggestive evidence [94, 101].

1.8 Models to replace experiments

Models can replace experiments when they are sufficiently trusted or when experiments are not feasible. This idea is now common to engineers developing nuclear weapons, building large bridges, or sending spacecraft to other planets, but perhaps less so to medical scientists. Yet, when the alternative is an experiment on a species with different physiology, numerical models may well be superior [145]. Moreover, researchers sometimes perform animal experiments to test physical rather than physiological theories, for example to investigate the effects of local action potential shortening or lengthening on the ECG. Such experiments could nowadays be performed more reliably with a numerical model.

With this idea in mind, we used simulations to test new methods to help guiding an ablation catheter to the site of origin of an arrhythmia, performing the entire procedure in silico rather than in the clinic [8, 9]. The outcome of these studies was that it would not accelerate the procedure enough to be worth clinical trials. While this is a disappointing result for the researchers, it saves enormous effort and possible risk for patients. We have also used simulations to replace patient data in order to train a machine-learning approach for arrhythmia localization [7, 10, 105]. In this case, using real data would almost certainly not have improved the results.

Chapter 2

A comparison of monodomain and bidomain reaction-diffusion models for action potential propagation in the human heart

Preface

A slightly different version of this chapter was previously published as Mark Potse, Bruno Dubé, Jacques Richer, Alain Vinet and Ramesh M. Gulrajani: A comparison of monodomain and bidomain reaction-diffusion models for action potential propagation in the human heart. *IEEE Trans. Biomed. Eng.*, 53:2425–2435, 2006. doi:10.1109/TBME.2006.880875.

The paper presented the first ever bidomain reaction-diffusion simulations of the human ventricles, as well as methodological inventions to build the model anatomy and to enable the simulations, which barely fitted in the computing equipment at hand. Most importantly, however, it showed that for most simulation studies a monodomain model is good enough. This saves roughly a factor 20 in compute time.

Some of the numerical methods used in this paper are now obsolete. At the time, computer memory was the limiting factor, so we used a lightweight but weak preconditioner. Nowadays much more powerful methods such as multilevel preconditioners would be used, as well as much larger numbers of processors. Yet, the results of the study remain highly relevant.

An important modification is that the quantity that was mistakenly named "bulk conductivity" in the paper is here named "monodomain conductivity."

Summary

A bidomain reaction-diffusion model of the human heart was developed, and potentials resulting from ventricular depolarization and repolarization were compared with results from a compatible monodomain model. Comparisons were made for an empty isolated heart and for a heart with fluid-filled ventricles. Both normal and

ectopic activation were simulated. The bidomain model took 2 days on 32 processors to simulate a complete cardiac cycle. Differences between monodomain and bidomain results were extremely small, even for the extracellular potentials, which in case of the monodomain model were computed with a high-resolution forward model. Propagation of activation was 2 % faster in the bidomain model than in the monodomain model. Electrograms computed with monodomain and bidomain models were visually indistinguishable. We conclude that, in the absence of applied currents, propagating action potentials on the scale of a human heart can be simulated with a monodomain model.

2.1 Introduction

The bidomain model represents active myocardium on a macroscopic scale by relating membrane ionic current, membrane potential (V_m), and extracellular potential (ϕ_e) [84]. Conceived in 1969 [194] and first expressed formally in 1978 [131, 213], the bidomain model was initially used to derive *forward models*, which compute extracellular and body-surface potentials from given membrane potentials [78, 79, 131, 132]. Later the bidomain model was used to connect multiple membrane models to form a *bidomain reaction-diffusion (*R-D*) model* [14, 185].

Bidomain R-D models have to solve an implicit equation to obtain ϕ_e at each integration step. Therefore their use has long been limited to relatively small preparations. For human-heart simulations, either fixed velocities and waveforms or monodomain models have been used to keep the problem tractable [21, 22, 43, 99, 100, 114, 211]. The monodomain approximation has allowed the development of R-D-type models for the human heart as early as in 1991 [114], and produces realistic activation patterns and V_m. However, it cannot be applied in all situations because it does not allow currents in the extracellular domain to influence V_m and ionic currents. This influence must be taken into account when pacing or defibrillation currents are applied [11, 60, 153, 182], but even in their absence the current flow through the extracellular and extracardiac domains may influence cardiac sources in a way that only bidomain models can account for [31, 62, 85, 185].

Since bidomain R-D simulations would be prohibitively expensive for routine work on the scale of a human heart, we investigated the differences between monodomain and bidomain simulations on a model of the human ventricles. Our model differs from previous numerical models of animal hearts [86, 208] in its scale and specifically human electrophysiolopgy, and from previous models of the human heart [31, 62, 117] in its ability to simulate a complete cardiac cycle in a reasonable period of time. To test the monodomain model, we compared conduction velocities and ϕ_e waveforms between monodomain and bidomain models. To obtain ϕ_e for the monodomain model we used a forward model that computed ϕ_e in exactly the same way as the bidomain model. The comparisons were done for an isolated-heart model, and for one in which the ventricular cavities were filled with fluid.

2.2 Methods

We consider two *domains*: intracellular and extracellular. The intracellular domain exists only for active tissue. The extracellular domain exists in active tissue as well as

medium	material	σ_{eT}	σ_{eL}	σ_{iT}	σ_{iL}
active	ventricular muscle	0.12	0.30	0.03	0.30
conductive	connective tissue	0.20	0.20	0	0
	fluid	0.60	0.60	0	0
insulating	air	0	0	0	0

Table 2.1: *Media, materials, and conductivity values in* Sm^{-1}.

in other tissue and in surrounding fluid. Three *media* are distinguished based on the conductivity in the two domains: 1) "Active tissue" is conductive in both domains; V_m and ϕ_e are defined in this medium. 2) "Conductive medium" conducts only in the extracellular domain; consequently only ϕ_e is defined. 3) "Insulating medium" is nonconductive in both domains; neither potential is defined for it. There are several *materials*, each belonging to one medium, and each having different conductivity. Boundary conditions must be considered between media but not between materials, as discussed below. An overview of media and materials, together with their conductivities, is given in Table 2.1.

Anatomic Model

The model anatomy was based on computed tomography data of a human heart obtained at autopsy [119]. Muscle and connective tissue were previously identified in the images at 1-mm resolution. From these data we made a surface description, which was then used to determine the node types in a three-dimensional (3-D) finite-difference (FD) grid with 0.2-mm resolution ($567 \times 501 \times 711$ nodes). Nodes could represent ventricular muscle (13 %), atrial muscle or connective tissue (5 %); fluid (4–10 %); or air (73–78 %). We will use the term "node" for those grid points that represent tissue or fluid. The atria were not activated in this study, but were retained to allow the simulation of a grounding electrode on the right atrium, similar to that used in isolated Langendorff-perfused hearts. Therefore we replaced the atrial muscle by connective tissue (Table 2.1).

For each ventricular node, we determined a minimal distance to endocardium and epicardium (d_{endo}, d_{epi}) using a 3-D distance transform with $(1, \sqrt{2}, \sqrt{3})$ chamfer distances [179]. A thickness parameter e was defined as

$$e = d_{endo}/(d_{endo} + d_{epi}). \tag{2.1}$$

The local fiber orientations were made orthogonal to the vector $\nabla\bar{e}$, where each element of $\bar{e}$ is the average of the corresponding element of e and its 26 neighbors. In practice, $\nabla\bar{e}$ did not suffer from singularities as ∇e would. This method ensured alignment of the fibers with the cardiac surfaces together with smoothly varying angles (Figure 2.1). The fiber orientation was further determined by a helix angle

$$\alpha = R\,(1 - 2e)^3 \tag{2.2}$$

to account for transmurally rotating fiber orientation [200, 202]. We set R equal to $\pi/3$ for the left ventricle (LV) and $\pi/4$ for the right ventricle (RV). The expression for α was adapted from one by Beyar and Sideman [25], which was based on measurements by Streeter et al. [200]. The power 3 served to better match the nonlinear curve

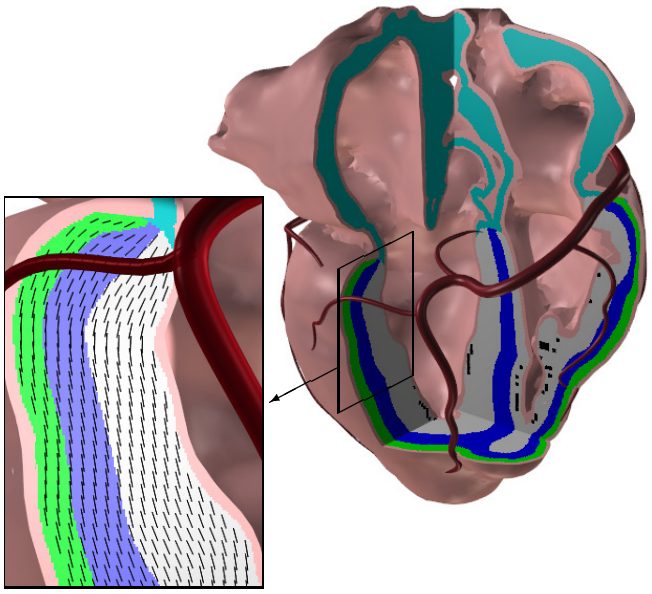

Figure 2.1: *Top right: heart model showing the tissue embedded in a thin layer of fluid (pink). Tissue types are identified with colors: gray for endocardial, blue for M cells, green for epicardial, and cyan for connective tissue. Black spots indicate early activation sites, which play the role of Purkinje-muscle junctions in our model. The heart is shown approximately in a posterior view with the left ventricular cavity on the left. Between the atria, the aortic annulus is visible. Coronary arteries are shown for orientation (veins were omitted); most prominent is the right circumflex artery which bends down in the crux cordis. Bottom left: detail of the left ventricular wall showing, at 1-mm resolution, the planes in which the fibers lie; the helix angle α is not shown.*

that Streeter et al. found for individual cases. The parameter e was also used to define three layers of different ventricular cell types: epicardial cells in the outer 20 % of the wall, M cells in the next 30 %, and endocardial cells in the inner 50 % [57, 116]. Ionic currents I_{ion} were computed using the model of the human ventricular cell membrane formulated by Bernus et al. [23], which accounts for these three cell types. We assumed that the interventricular septum is layered like the LV wall, except for the presence of endocardial cells on the RV side. We ignored differences between LV and RV cells [55, 224]. The different cell layers are illustrated in Figure 2.1. The model had no Purkinje network; for sinus rhythm simulation we stimulated the ventricles at the early activation sites and corresponding times published by Durrer et al. [59, 119]. Stimulation was performed by transmembrane current injection ($200\,\mu\text{A}/\text{cm}^2$ during 2 ms, interrupted when V_{m} exceeded 30 mV) to mimic a physiological stimulus. The same stimulation technique was used to initiate ectopic activation.

Bidomain Model

The bidomain model [131, 194, 213] describes the cardiac tissue as consisting of two co-located syncytia termed the intracellular and extracellular domain, which are characterized by conductivity tensors G_{i} and G_{e}, respectively. A current with surface density I_{m} flows between the two domains. The intracellular and extracellular

potentials ϕ_i and ϕ_e are subject to the *bidomain equations*:

$$\nabla \cdot (G_i \nabla \phi_i) = \beta I_m \tag{2.3}$$
$$\nabla \cdot (G_e \nabla \phi_e) = -\beta I_m \tag{2.4}$$

where β is the membrane surface-to-volume ratio, i.e. the amount of membrane in a unit volume of tissue. The transmembrane current density I_m consists of a capacitive part, an ionic part $I_{ion}(V_m, t)$ generated by the cell membrane, and an imposed stimulation current density I_s:

$$I_m = C_m \frac{\partial V_m}{\partial t} + I_{ion} + I_s \tag{2.5}$$

where C_m is the membrane capacitance per unit area. We used $\beta = 1000\,\mathrm{cm}^{-1}$ and $C_m = 1\,\mu\mathrm{F/cm}^2$. Using an operator splitting approach [221] we write the equations in terms of ϕ_e and V_m as an R-D equation

$$\frac{\partial V_m}{\partial t} = \frac{1}{\beta C_m}\Big\{\nabla \cdot \big(G_i \nabla (V_m + \phi_e)\big) - \beta (I_{ion} + I_s)\Big\}, \tag{2.6}$$

which we used to integrate V_m over time, and an implicit equation

$$\nabla \cdot ((G_i + G_e)\nabla \phi_e) = -\nabla \cdot (G_i \nabla V_m) \tag{2.7}$$

from which we solved ϕ_e.

Implementation

Computations were performed on 32 processors of an SGI Altix 3700 computer. This system has 64 nodes, each containing 2 processors and 8 GB of memory. The nodes intercommunicate over 3.2 GB/s (bidirectional) links. Although its memory is decentralized, the system provides a single memory image. The code was written in C and parallelized with OpenMP. Care was taken to place each data element on the node where it would be used most often, and to minimize sharing of data between nodes, since this minimizes memory access times. We also maximized cache line reuse by storing large arrays exactly in the order in which they were used by critical sections of the code.

Equation 2.6 and Equation 2.7 were discretized using a forward Euler approach to integrate over time, resulting in

$$V_m^{t+\delta t} = V_m^t + \frac{\delta t}{\beta C_m}\Big\{A \cdot (V_m^t + \phi_e^t) - \beta (I_{ion}^t + I_s^t)\Big\} \tag{2.8}$$

and

$$B \cdot \phi_e^{t+\delta t} = A \cdot V_m^{t+\delta t} \tag{2.9}$$

where A and B are $N \times N$ matrices whose coefficients are computed from $G_e + G_i$ and G_i, respectively; N is the number of nodes. Since the fiber direction was a function of position, G_e and G_i were inhomogeneous tensor fields, which were determined and stored for each FD node by transforming a diagonal conductivity tensor $\mathrm{diag}(\sigma_T, \sigma_T, \sigma_L)$ from local coordinates that are aligned with the local fiber direction to global coordinates. For the transverse and longitudinal conductivities, σ_T and

σ_L, we used the nominal values determined in a review of experimental studies by Roth [186]. An overview of all conductivity values in myocardium, fluid, and connective tissue is given in Table 2.1. We indicate the conductivities by σ_{eT}, σ_{eL}, σ_{iT} and σ_{iL} with subscript 'e' for extracellular, 'i' for intracellular, 'T' for transverse, and 'L' for longitudinal.

The A and B matrices have 19 nonzero elements per row. Since the positions of the nonzero matrix elements could be computed efficiently, we stored only their values, as single-precision floating point numbers. The diagonal elements, whose values must accurately equal the negative sum of the other elements on the row, were computed on the fly and in double precision when a matrix multiplication was performed. This is more efficient than obtaining them from memory. We computed A and B using an expression proposed by Saleheen and Ng, which accounts for the inhomogeneously anisotropic conductivity and allows discontinuities in the conductivity tensor fields [190]. In their approach, the boundary of a medium is just another discontinuity, where $G = \underline{0}$ outside the medium. Since the conductivity outside the medium is zero, there is no current flow across the boundary, so the conditions

$$\hat{n} \cdot G_i \nabla \phi_i = 0 \quad \text{on } \partial_{\text{tissue}} \tag{2.10}$$

$$\hat{n} \cdot G_e \nabla \phi_e = 0 \quad \text{on } \partial_{\text{air}} \tag{2.11}$$

were satisfied without being explicitly enforced. Neighbor nodes outside the simulated volume were treated as air, so that there was also no current flow through this boundary.

In Saleheen and Ng's method [190], the conductivity is constant on "elements" and changes only in a thin transition layer between the elements. An element is a rectangular volume cornered by 8 nodes. The custom-made software that produced the grid ensured that the node types were consistent with the elements (Figure 2.2). Because the conductivity is defined on elements rather than nodes, the boundary is infinitesimally close to the nodes (due to the transition layer the boundary does not run through the nodes [190]). Nodes on the tissue boundary therefore represented less tissue volume than interior nodes (Figure 2.2). This was accounted for by assigning them a proportional fraction of the standard value for β, as illustrated in Figure 2.2.

At each time step, I_{ion} was computed from V_m at the previous time step using the membrane model [23]. A "hybrid" method was used to integrate the state variables [188, 219]. The new V_m was then computed by evaluation of Equation 2.8, and used to compute ϕ_e using Equation 2.9.

Equation 2.9 is a system of N linear equations. In our case, where $N \sim 10^7$, classical elimination techniques and matrix decompositions could not be used because they have memory usage and operations count up to order N^2. Only iterative methods can solve systems of this size [221]. After initial experiments with the well-known conjugate gradient and biconjugate gradient algorithms [177] and the biconjugate gradient squared variant [196], we finally implemented a more sophisticated biconjugate gradient stabilized (BICGSTAB) solver [189, 214]. This algorithm proved to be the most efficient in terms of CPU time. Application of more recent variants such as QMRCGSTAB [35] gave no further improvement.

The solver routine used an initial guess for the solution. We found that using ϕ_e^t as an initial guess for $\phi_e^{t+\delta t}$ reduced the number of iterations by two orders of magnitude

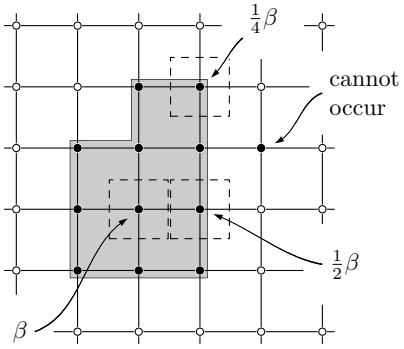

Figure 2.2: *Finite-difference grid illustrated in 2-D. The gray area represents one of the 3 media in one of the 2 domains, e.g. active tissue in the intracellular domain. Filled circles represent grid nodes that are internal to the medium, open circles nodes that are external. Grid squares correspond to "elements" in Saleheen and Ng's method; only elements that are completely inside the medium have nonzero conductivity. Dashed squares indicate the areas represented by three example nodes: one inside the medium, which has the standard β value; one on a boundary, with $\beta/2$; and one on a corner, with $\beta/4$. Internal nodes cannot occur as pseudopods, without a neighboring internal element.*

compared to zero initialization. A further reduction was obtained by using

$$\psi_1^{t+\delta t} = \phi_e^t + (V_m^{t+\delta t} - V_m^t)\, k, \tag{2.12}$$

where k is a constant. If the monodomain approximation $G_i = \xi G_e$ [211] for a scalar ξ applies, then $\phi_e \equiv -\xi/(1+\xi)V_m + \phi_0$, where ϕ_0 is a constant offset potential, so setting $k = -\xi/(1+\xi)$ would result in perfect prediction. In the general bidomain case, where there is no simple relation between ϕ_e and V_m, we found that a good prediction can still be obtained with $k = \sigma_{iT}/(\sigma_{iT} + \sigma_{eT})$. An alternative predictor is

$$\psi_2^{t+\delta t} = 2\phi_e^t - \phi_e^{t-\delta t} \tag{2.13}$$

which is obtained by hypothesizing that $\partial^2\phi_e/\partial t^2 \approx 0$ [148]. The reduction of the iteration count obtained with ψ_1 and ψ_2 depends on the anisotropy, the complexity of the activation front, and the interval of ϕ_e computation. As discussed below, we computed ϕ_e at intervals of 50 µs. For such large steps ψ_1 performed better, while ψ_2 was generally better at intervals below 10 µs.

Iteration of the solver for Equation 2.9 was terminated when the norm of the residual became smaller than either 1) 10^{-4} times the norm of the right-hand side $A \cdot V_m^t$, or 2) a fixed threshold of $0.1[(\delta x/0.2\,\mathrm{mm})^3 N]^{1/2}\,\mu\mathrm{A/cm^2}$, where N is the number of nodes and δx the spatial step ($\delta x = 0.2$ mm for the complete model and $\delta x = 0.1$ mm for a small tissue block as discussed below). For comparison, the peak membrane current density associated with a depolarization wavefront is in the order of $10^5\,\mu\mathrm{A/cm^2}$. The fixed-threshold criterion prevents unnecessary accuracy in the repolarization phase. As discussed below, both thresholds were taken 10 times smaller for output of signals, once per millisecond of simulated time.

We used an incomplete-LU (ILU) preconditioner [189, 196], which was parallelized using domain decomposition [189]. Its performance was compared to a diagonal or "Jacobi" preconditioner [177].

The ILU factorization and the A and B matrices together used about half the total memory of the program. The remaining memory was used primarily by the membrane status variables, V_m, ϕ_e, and arrays used by the solver routine. The memory usage was approximately 0.5 kB per node.

Equation 2.9 only determines ϕ_e up to an additive constant, so that the linear system is singular. Singularity is by itself not a problem for Krylov-subspace methods such as BICGSTAB. However, for large systems such as ours, accumulated rounding errors can build up a residual component in the direction of the eigenvector associated with the singularity, i.e. the common mode of the extracellular potentials. This component can spoil the solver's estimate of convergence. A similar problem occurs when the system is made nonsingular by setting the potential at one or more nodes to zero. Therefore we adapted the BICGSTAB routine to explicitly orthogonalize the residual with respect to the common mode, and did not fix any potentials. A reference potential taken from the roof of the right atrium was subtracted from the extracellular potentials after a solution was obtained.

The membrane potential V_m was computed with a time step of $\delta t = 10\,\mu s$. The stepsize was doubled when all cells finished depolarization, defined as the time when the activation variable m of the Na current [23] exceeded 0.98. The stepsize for V_m computation was limited both by the time constants of the Na current and by the stability criterion determined by the conductivities and spatial discretization [177, 211]. As proposed by Vigmond et al., the computation of ϕ_e was performed less frequently [208,221]. This is advantageous because the iterative solution of Equation 2.9 is much more time-consuming and more difficult to parallelize than the evaluation of Equation 2.8. We generally updated ϕ_e once in every $5\delta t$, i.e. at 50-µs intervals during depolarization and 100-µs intervals during repolarization.

Comparison with a monodomain model

The monodomain model can be derived from the bidomain model by assuming that the conductivity tensors satisfy $G_i = (1+\xi)\,G'$ and $G_e = (1+\xi)/\xi\,G'$ where ξ is a scalar and G' is the "monodomain conductivity tensor" [78, 114] whose elements are

$$G'_{\mu\nu} = \frac{G_{i\mu\nu} G_{e\mu\nu}}{G_{i\mu\nu} + G_{e\mu\nu}} \tag{2.14}$$

By substituting these definitions of G_i and G_e in Equation 2.7, a linear relation between ϕ_e and V_m is obtained:

$$\phi_e = -\frac{\xi}{1+\xi} V_m + \phi_{off} \tag{2.15}$$

where ϕ_{off} is a constant offset potential. If this expression for ϕ_e is substituted in Equation 2.6, an R-D equation is obtained in which ϕ_e does not occur:

$$\frac{\partial V_m}{\partial t} = \frac{1}{\beta C_m}\Big\{\nabla\cdot\left(G'\nabla V_m\right) - \beta(I_{ion} + I_s)\Big\} \tag{2.16}$$

Since ϕ_e plays no role in the monodomain model, there is no implicit equation to solve. This makes monodomain models much less demanding than bidomain models.

We performed monodomain simulations by computing propagation of V_m from Equation 2.16 instead of Equation 2.6. In both monodomain and bidomain simulations, ϕ_e was computed from Equation 2.7, i.e., based on the bidomain conductivity tensors G_i and G_e. For the monodomain model, this corresponds to solving a separate forward problem, and is only done once per millisecond of simulated time. In the monodomain model, the propagation velocity is expected to be proportional to the square root of the monodomain conductivity [40]. We computed G' using Equation 2.14 from the conductivities in Table 2.1. Thus, the monodomain conductivity was the same in our monodomain and bidomain simulations, so propagation patterns should match exactly if the monodomain approximation were valid.

Simulations

Simulations using varying numbers of processors for short intervals during depolarization were used to measure the scalability of the program, i.e. its ability to use a larger number of processors efficiently. In the same way, the performance of the two preconditioners was evaluated.

Propagation velocities were measured in a $40 \times 40 \times 40$ mm tissue block with straight fibers, which had a 1 cm-thick fluid bath on top and was insulated on the 5 remaining sides. The block was stimulated in the center of the tissue volume. Due to symmetry only a quarter of the block had to be computed. This simulation was also performed with a reduced spatial step (δx) of 0.1 mm, and with both bidomain and monodomain models. Another test of the model was performed by simulating epicardial maps of extracellular potentials obtained after epicardial and intramural pacing and comparing them with experimental results obtained in dogs by Taccardi et al. [202].

Finally, we compared activation times, action potential (AP) durations, AP waveforms, and extracellular potentials between monodomain and bidomain simulations using 1) a model with intracavitary blood, 2) a model with only a thin layer of blood on the ventricular walls, and 3) a model with no fluid at all. This comparison was performed for the epicardial pacing experiment described above, as well as for a sinus beat.

2.3 Results

Program behavior

The heart model at 0.2-mm resolution had 26 million nodes representing active tissue, for which V_m and ϕ_e were computed, and 10 million nodes representing connective tissue and atrial muscle, for which only ϕ_e was computed. Simulations with the resulting 36-million-node "dry heart" model produced $\phi_e > 40$ mV in late-activated areas. We considered this to be beyond the physiological range [176,184,202]. Therefore we performed all following simulations with a 1-mm layer of fluid appended to the endocardial and epicardial surfaces, a situation approximating a Langendorff setup. This measure added 9 million nodes for which ϕ_e was computed. Filling the cavities with blood resulted in another 10 million such nodes. Thus, we computed

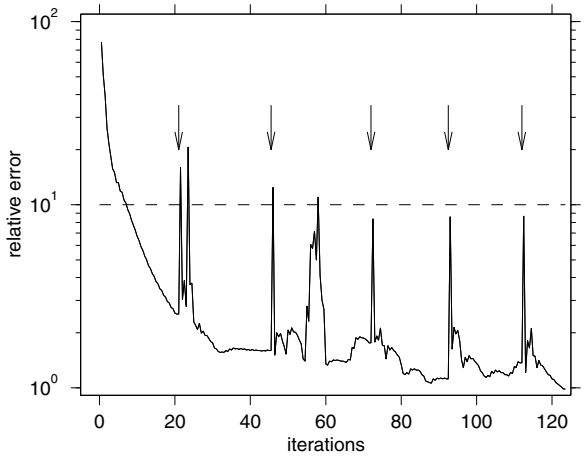

Figure 2.3: *Example of the convergence behavior of the solver for ϕ_e. The error is given relative to the tolerance level L_2 used for output of signals. The higher tolerance level L_1 used at intermediate time steps is indicated with a dashed line. This level falls in the relatively fast initial convergence regime. Gray vertical lines indicate restarts of the BiCGStab routine. The first restart is preceded by a short interval of stagnation. Each restart allows further convergence at the price of an initial divergence.*

26 million membrane potentials and either 45 million or 55 million extracellular potentials. These models used 22 GB and 26 GB of memory, respectively.

Figure 2.3 illustrates the typical convergence behavior of the solver for ϕ_e. Initially the convergence was relatively fast and regular. A subsequent slowdown coincided with a loss of accuracy in one of the minimization parameters in the solver [214]. A restart of the solver made further convergence possible but introduced an irregular convergence regime. Two tolerance levels, L_1 and L_2, were used; L_1 is indicated with a dashed line in the figure. Use of L_1 resulted in ϕ_e that were accurate enough for correct computation of V_m. Comparison with a simulation using a 100 times lower tolerance level showed differences in activation time of at most 0.01 ms and differences in ϕ_e of at most 1.5 mV. Differences in V_m were in the order of 0.02 mV, except during the steep AP upstroke, where they could be as large as 3 mV during one sample.

Electrograms computed with L_1, however, were not satisfactory. They typically featured depression of the S-T segment to about -1 mV, and had values around $+1$ mV at $t = 600$ ms, where they are expected to be zero. These offsets were proportional to the tolerance level. We decided to use a level $L_2 = 0.1L_1$ for computation of ϕ_e just before output (once per ms). Since the application of L_2 increased the number of iterations by a factor 2.5 on average, we used L_1 for all other updates of ϕ_e (once per $5\,\delta t$, i.e. 19 times per ms during depolarization).

Simulation of one heart beat (600 ms) in sinus rhythm took 39 hours with empty ventricles and 51 hours with the blood-filled version on 32 processors. Figure 2.4(a) shows the speedup obtained with various numbers of processors for a heart model of 45 million nodes. We had to use at least 8 processors, to obtain the memory required by the program. Speedup for 8 processors is defined as 8. For the case of 32 processors, the number that we usually employed, the speedup is then 30.6, cor-

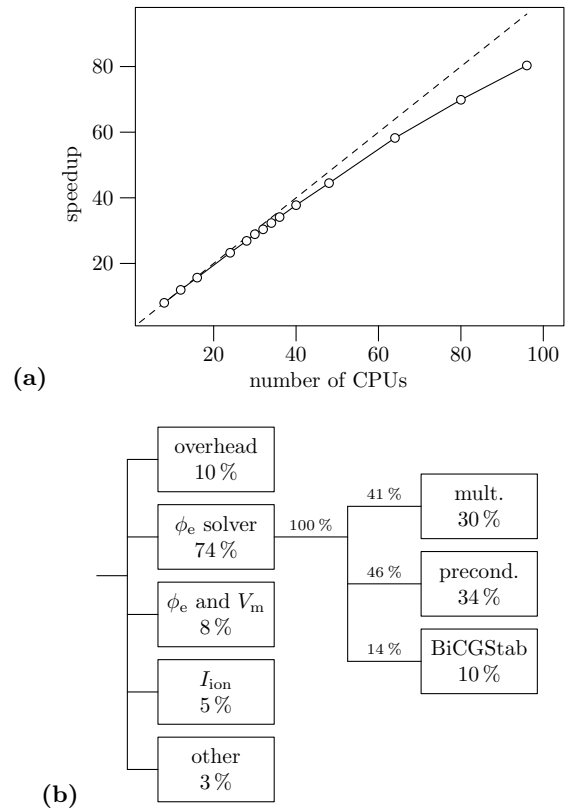

Figure 2.4: *(a) Speedup as a function of the number of processors. The speedup for N processors is defined as the runtime with one processor divided by the runtime with N processors. We used a minimum of 8 processors. The speedup is therefore computed as 8 times the runtime with 8 processors divided by the runtime with N processors. The dashed line indicates ideal speedup.*
(b) Relative time consumption of the major program components for a simulation with 55 million nodes on 32 processors. The code that solves the extracellular potential ϕ_e is by far the most time-consuming, using 74 %. It is subdivided into "multiplier," the code that multiplies the problem matrix by a given vector; (ILU) preconditioner; and "BiCGStab," the solver proper, which uses little time compared to the multiplier and the preconditioner. After the solver, parallelization overhead (including load imbalance) is the most time-consuming with 10 %. Other computations for V_m and ϕ_e use 8 %, the membrane model takes 5 %, and the remainder of the program 3 %.

responding to a performance loss of 4 %. The loss grows to 8 % for 64 processors and 16 % for 96 processors, the maximum that we could use for this test. Figure 2.4(b) shows how time consumption, measured in CPU cycles, was divided over the major program components.

The performance of the two preconditioners was compared for a simulation of a heart model of 55 million nodes with 32 processors. The diagonal preconditioner was 18 times faster (0.02 s per call) than the ILU preconditioner (0.36 s). For the solver as a whole the ratio was much closer to unity due to other time-consuming routines (Figure 2.4b), which took a total of 0.76–0.78 s per iteration. The preconditioner is called twice per iteration [214]. Thus, a single solver iteration took 0.88 s with the

	δx (mm)	longitudinal	transverse
bidomain	0.10	770	278
monodomain	0.10	756	277
bidomain	0.20	731	218
monodomain	0.20	713	217

Table 2.2: *Propagation velocities (mm/s).*

diagonal preconditioner and 1.50 s with the ILU preconditioner. However, the number of iterations necessary for the depolarization phase was 3.7 times larger with the diagonal preconditioner than with the ILU preconditioner. Consequently, the total runtime was 2.0 times larger with the diagonal preconditioner.

Simulation results

Propagation velocities were measured in a $40 \times 40 \times 20$ mm tissue block covered with 10 mm fluid. This simulation was also performed with a reduced spatial step (δx) of 0.1 mm, and with both bidomain and monodomain models. Results are shown in Table 2.2. With $\delta x = 0.2$ mm the longitudinal and transverse velocities were 95 % and 78 %, respectively, of those obtained with $\delta x = 0.1$ mm. With 0.1-mm resolution, the ratio of longitudinal to transverse velocity was 2.8; with 0.2-mm resolution it was 3.4. The longitudinal velocity was 2 % higher in the bidomain than in the monodomain simulations, at both resolutions.

A verification of the model was performed by simulating epicardial potential maps obtained after epicardial and intramural pacing in open-chest dogs [202]. Development of the potential pattern reflected the transmural rotation of fibers, showing an expansion and counterclockwise rotation of the positive areas for (sub)epicardial pacing, expansion and clockwise rotation for subendocardial pacing, and a more symmetric expansion for mid-wall pacing. The case of sub-epicardial pacing is illustrated in Figure 2.5.

The two maxima in the pattern had slightly different magnitudes, as was also observed experimentally [202]. To determine if this was purely a projection effect, with one maximum appearing smaller just because it lies deeper in the wall, we inspected isopotential surfaces, and found that the larger maximum was actually stronger and surrounded by a larger region of positive potentials. We quantified the strength of the maxima by integrating, for each of the two positive regions, the potential values over the volume where $\phi_e > 0.1$ mV. The resulting value was consistently about 20 % larger for one of the maxima, throughout the 40-ms interval that we simulated. Extracellular potentials calculated from monodomain V_m were nearly identical to bidomain results. All characteristics that were mentioned, including the difference in maxima, were reproduced by ϕ_e computed from monodomain V_m.

For a sinus beat, total depolarization of the ventricles took 103.5 ms in the monodomain model, 98.4 ms in the dry heart, 97.1 ms in the heart with fluid layer, and 97.0 ms in the heart with filled cavities. Activation time (AT) was measured with 0.01-ms accuracy. The difference in AT between the two models, as a function of AT in the bidomain model, grew almost linearly throughout the depolarization phase.

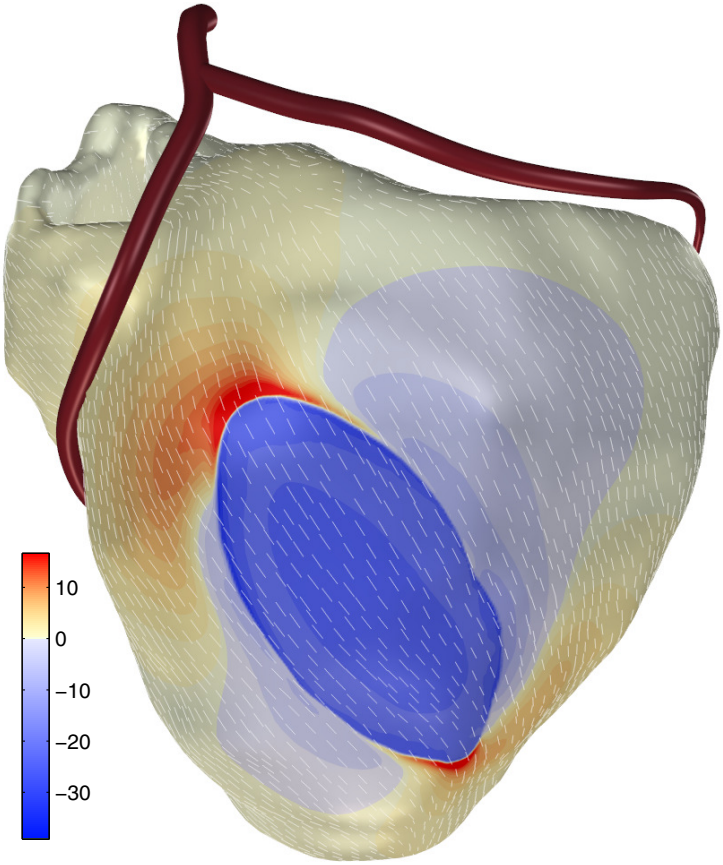

Figure 2.5: *Extracellular potentials on the left ventricular epicardial surface 28 ms after subepicardial pacing. Only the ventricular muscle is shown, with the left anterior descending and left circumflex arteries for orientation. Short white line segments indicate epicardial fiber orientation. A nearly elliptic dark-blue area indicates the negative extracellular potentials that are due to depolarized tissue; deviations from an elliptic shape are caused by the counterclockwise transmural fiber rotation. Low-level negative potentials also witness this rotation. Positive potentials (yellow to red) occur where depolarization travels along the fibers. The curved positive area, which can be well distinguished on the top left side, is again due to the fact that this longitudinal direction is rotated counterclockwise in deeper layers.*

Simulated electrograms are shown in Figure 2.6. The figure shows features that can also be observed on the human heart [26, 184], such as low-amplitude complexes in the RV basal area, small R waves (initial positive waves) and large S (negative) waves in the middle part of the RV free wall, and large R waves on the left ventricular wall. The figure also shows that differences between monodomain and bidomain models are small compared to differences between empty and filled ventricles.

Repolarization time (RT) was defined as the earliest instant where $V_\mathrm{m} = -70\,\mathrm{mV}$ and $dV_\mathrm{m}/dt < 0$. Action potential duration (APD) was defined as RT minus AT. In the model with filled cavities the APD was lengthened by 1 to 1.5 ms in the area that was activated in the first 10 ms. This effect cannot be reproduced by the monodomain model, in which there is no representation of intracavitary fluid. Since the APD differences were very small, the RT differences were governed by the AT differences

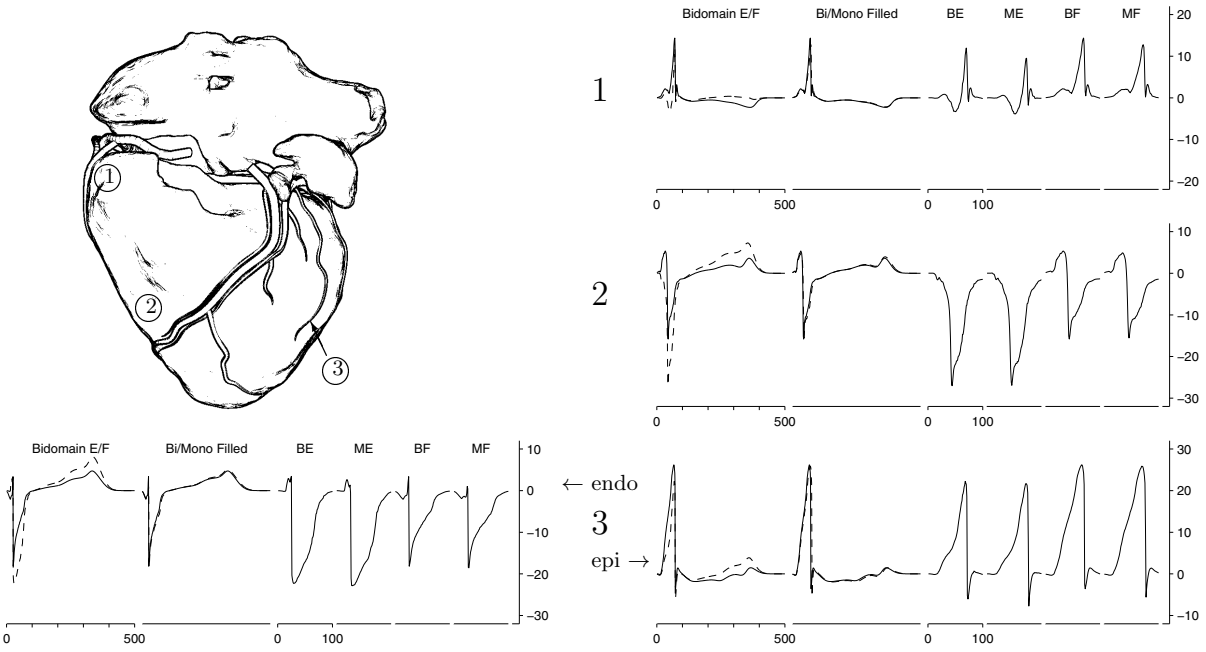

Figure 2.6: *Examples of extracellular potentials (electrograms) obtained with a monodomain and forward model and with a bidomain model, at 3 locations on the epicardial surface of the ventricles, and one on the endocardial surface. Electrograms were obtained either in ventricles with only a fluid layer ("Empty") or with filled cavities ("Filled"). For each site, 6 frames of axes are shown. The first compares empty (gray line) with filled ventricles (black line) in a bidomain simulation. The second frame compares monodomain (gray) with bidomain results (black) for the case of filled ventricles. The remaining four frames show the first 100 ms of the electrogram in empty bidomain (BE); empty monodomain (ME); filled bidomain (BF); and filled monodomain (MF) simulations.*

described above.

Minima and maxima of extracellular potentials throughout the heart were considered as a function of time. The range was beyond $(-60, +40)$ mV in the dry model, $(-53, +29)$ mV in the model with fluid layer, and $(-44, +36)$ mV in the fluid-filled model. Maximum potentials occurred in the R waves and were generally higher at later points in time, but the extrema did not grow monotonically. This demonstrates that both global electrotonic effects and local fiber orientation contribute to R-wave magnitude. For the monodomain model the ranges were $(< -60, > +40)$, $(-54, +30)$, and $(-44, +34)$, respectively.

Filling of the cavities reduced R-wave amplitude within 4 mm of the endocardial surface by a few millivolts, and increased R-wave amplitude in midmural and epicardial layers by up to 10 mV (Figure 2.6). These effects too were accurately reproduced by ϕ_e computed from monodomain V_m. Potentials in the intracavitary fluid were always negative during depolarization, even very close to the endocardium.

2.4 Discussion

Bidomain versus Monodomain

The bidomain model is widely used to simulate propagation in tissue preparations [30, 63, 75]. More recently, its application was extended to hearts of small mammals: Trayanova et al. described a finite-element model of the rabbit heart with 0.5-mm resolution [208]. Henriquez et al. reported a 75 µm-resolution finite-volume model of the mouse heart [86]. The small size of these hearts made it possible to use a high-resolution mesh while keeping the number of nodes well below a million. Simulations in tissue preparations have used several millions of nodes [210, 226], and simulation of the human heart requires a mesh size that is almost two orders of magnitude larger. Lines et al. [117] have discussed techniques for a bidomain torso-coupled human heart model, but have shown only example simulations with a very coarse mesh. With the hardware at our disposal we had to resort to a resolution of 0.2 mm for our FD model of a human heart, comprised of 26 million tissue nodes and up to 29 million nodes in the surrounding fluid.

We investigated the impact of the monodomain assumption on simulated propagation in an isolated human heart, by comparing results with a bidomain model. Differences between the two models were extremely small, even if extracellular potentials were influenced considerably by fluid-filled cavities. There was a small difference in propagation velocity between the monodomain and the bidomain model. All other properties of the membrane potentials and extracellular potentials simulated by the bidomain model were accurately reproduced by the monodomain model with a forward solver for the extracellular potential. We have repeated the experiments shown in this paper with simulated ischemia and with the Na conductivity [23] reduced to 1/10 of its normal value, and arrived at the same conclusions.

Since the monodomain approximation is not even approximately valid (Table 2.1) it may be expected that monodomain simulation results differ importantly from bidomain results. Monodomain R-D models were developed before the first bidomain R-D models, and few papers have compared monodomain with bidomain results. Those that did, have shown small differences [221], and monodomain simulations have provided realistic results [21, 22, 99, 100, 114, 211]. The epicardial potential results of Taccardi et al. were accurately reproduced by bidomain, monodomain, and eikonal models [43, 135, 158]. The success of the monodomain approximation may be considered a common wisdom, which we have formalized by demonstrating that even if differences between monodomain and bidomain results can be found, they are small enough to be ignored for most applications, with the obvious exception of simulations involving applied currents. Another exception must be made for the influence of adjacent fluid on V_m within a few hundred micrometer from the surface [85, 185]. These effects seem negligible on the scale of a human heart. However, they may be significant in hearts of small rodents, and are critically important for the understanding of superfused preparations [187]. We attribute the success of monodomain models not to the validity of the assumption of equal anisotropy (which results in unrealistic extracellular potentials), but rather to the observation that the difference between monodomain and bidomain ϕ_e is a smooth function of position. This difference therefore contributes little to the diffusion current.

The ability to simulate extracellular potentials is important because these can be observed much more easily than transmembrane potentials. Monodomain models do

not produce realistic extracellular potentials, but we have shown that the ϕ_e computed from the membrane currents produced by a monodomain model are very close to those of a bidomain model. Such a solution is able to account for the effect of the thorax and the intracavitary blood on ϕ_e [79].

The method to solve the forward problem for our monodomain model is the same as in the bidomain model. While this provides a fair comparison, it is not a typical example of a forward model. Such models usually employ a few dozen current dipoles [79, 131], or epicardial potentials sampled at a few hundred points [15, 106]. Our "source model," in contrast, incorporated membrane potentials throughout the heart sampled at 0.2-mm resolution. We did not investigate the impact of lower-resolution source representations in this study.

The conductivity of the thorax influences epicardial ϕ_e [31, 77, 106, 123]. However, its influence on V_m was never assessed. Modeling studies establishing the influence of torso coupling have used epicardial ϕ_e as the source model [31, 106]. Experimental studies have shown that epicardial ϕ_e changes [77, 123], but effects on V_m were not reported. A source model consisting of membrane currents may be more stable since the membrane can be thought of as a current source. With respect to the isolated heart, we have shown that intracavitary conductivity changes ϕ_e, but not V_m. We have verified that this change in ϕ_e can be computed from monodomain V_m just by employing an appropriate forward model. The conductivity of the thorax may be expected to have a larger influence on cardiac potentials than the intracavitary blood. Therefore it would be useful to verify the applicability of the monodomain assumption for the in-situ heart. This requires coupling of the heart to a torso model. Torso coupling was described by several groups [31, 62, 117], but never applied to a complete high-resolution 3-D human heart and torso. To implement a thoracic coupling for our heart model we would have to use a discretization method that allows a coarser grid at some distance from the heart. While this is feasible, it is challenging to reconcile this with the streamlined solver routines that we used to make bidomain modeling on the scale of a human heart at all possible.

While the differences between monodomain and bidomain results are small enough to permit the use of a monodomain model for propagation studies, there is no doubt that a bidomain model is necessary to simulate pacing or defibrillation. These topics were not addressed in this study. Our model can be used to some extent to simulate pacing with extracellularly applied currents. However, defibrillation currents would cause erroneous activations in an FD model with irregular boundaries. Our methods can be used for defibrillation only in rectangular blocks aligned with the coordinate axes.

The time gain of using a monodomain model and a separate forward model to compute ϕ_e results from solving ϕ_e less often (e.g. 1/ms) than in a bidomain R-D model, and perhaps on a coarser grid [221]. This gain is limited because a lower tolerance level is needed for computation of electrograms than for propagation of potentials per se. Solving ϕ_e on the same grid as used in the bidomain model, at 1-ms intervals, our monodomain and forward model were only about twice as fast as our bidomain model.

Epicardial mapping

The epicardial mapping data reported by Taccardi et al. constitute an interesting challenge to computer heart models [202]. Several researchers have attempted to simulate these results [43, 135, 158], and have explained many of the reported features. An exception is the observed difference in strength of the two maxima in the potential patterns, which Taccardi and colleagues attributed to the imbrication angle of the fibers [202]. Despite the presence of imbrication in their model of an idealized ventricle, Colli Franzone et al. did not obtain an important difference [43]; but Muzikant et al. [137] did, using a realistic imbrication angle of 5°. We studied simulated epicardial potentials following subepicardial stimulation and observed asymmetry in the positive potentials even when imbrication was zero. We hypothesize that this difference is due to varying wall thickness or slight convergence/ divergence of the fiber orientations, but we presently did not investigate these hypotheses.

The model

Due to its relatively low spatial resolution of 0.2 mm, our model underestimates the transverse propagation velocity by about 22 % for the parameters chosen in this study. This may be compensated by assuming a larger conductivity, but more elegant solutions may also be conceived. First, more accuracy can be obtained with a higher resolution, which we currently cannot implement because it would require too much computer memory and CPU time. Second, a higher-order estimate for the diffusion operator $\nabla \cdot (G_i \nabla)$ in Equation 2.6 or an integral equation for the diffusion current [14] could be employed. These would increase memory usage and runtime less. Third, a finite-element or finite-volume method may be more accurate at the same or even a coarser discretization [208, 210]. Finally, we could use a modification of the membrane model that slows down the depolarizing sodium current to make the depolarization wavefront thicker and less steep [24]. The side effects of such modifications are hard to predict, so this method should be used with caution when membrane behavior is studied.

The value of $\beta = 1000\,\mathrm{cm}^{-1}$ used in this study is low compared to measured values [120]. Together with the conductivity and the membrane capacitance C_m, β determines propagation velocity. Values used in modeling studies vary from 200 to 3000 [14, 23, 31, 86, 100, 118, 120, 136, 153, 185, 208, 211]. Generally, authors of propagation studies who reported realistic propagation velocities have found it necessary to use low values of β. A possible explanation for this discrepancy is that due to the tight packing of fibers into bundles, effective β or C_m is smaller in tissue than in isolated myocytes, in which they are usually measured.

We used a mathematical definition of fiber orientation that is conceptually simple, but is able to represent the known macroscopic features such as alignment with the surfaces and transmurally rotating fiber orientation. Regional variations in the range of transmural rotation can be made, although presently we only assigned different ranges to the left and right ventricles. This mathematical definition is an improvement of the methods used previously by Lorange et al. [119, 211] and is based on qualitative and quantitative knowledge of cardiac anatomy [25, 200]. Several groups

have reported the use of fiber orientations measured by histological means or by diffusion tensor imaging [20, 65, 113]. We have not used such data because we feared that measurement errors might occasionally cause discontinuities and large imbrication angles, which would be difficult to repair. In addition, our mathematical definition facilitates study of recognizable features, such as imbrication, in isolation.

The linear system solver and preconditioner used are among the most powerful algorithms of their kind. However, recent comparisons suggest that multilevel methods could be competitive [12, 134]. Our model readily solved the small-scale features of ϕ_e, which are important for the propagation algorithm. It had difficulty to reach the lower tolerance level L_2 because it could not easily resolve smaller gradients, which build up appreciable errors over long distances – especially in large models. Multilevel methods should be able to deal better with the long-distance features, and would thus be especially advantageous if correct ϕ_e traces are required, rather than accurate $\nabla \cdot (G_i \nabla \phi_e)$ for use in Equation 2.6.

In this study we used a membrane model that is a compromise between accuracy of representation and computational efficiency [23]. However, the model is designed to work with any membrane model, can assign different membrane models to different nodes, and can employ spatially varying parameters for the membrane model. Since the membrane routine takes a relatively small fraction of the computation time, we have not considered additional optimizations for the membrane model such as adaptive time steps [115, 219].

The memory usage of the program, 0.5 kB per node, compares favorably to the estimate of *at least* 2 kB per node given by Lines et al. [117]. This is due to several savings. We used a regular mesh, for which no geometrical data and very few topological data need to be stored. In addition, we found that the matrices A and B as well as the ILU coefficients can be stored in single precision. For single-beat simulations, the membrane state variables too can be stored in single precision. Finally, we used a relatively simple membrane model with only 6 state variables.

The speedup (runtime reduction when more processors are employed) of our model is satisfactory. Although we optimized our program for use with 16 to 32 processors, speedup from 32 to 64 processors is a factor 1.92. This implies a performance loss of only 4 %. Thus, it will be relatively easy to improve the spatial resolution of our model when larger machines become available for our work.

2.5 Conclusion

We have developed a bidomain R-D model of the human heart that can compute a full cardiac cycle in a reasonable period of time. The model can also operate as a monodomain, optionally with a forward solver for ϕ_e. We have shown that a bidomain model is not necessary for propagation studies. Thus, even with the (more economical) monodomain model we can simulate epicardial, endocardial, intracavitary, and intramyocardial signals that can be compared with measured signals. Both models can be used to study the changes that occur in these signals as a result of abnormalities in ionic currents and in tissue properties.

2.6 Acknowledgment

The work described in this paper was initiated under the direction of Dr. Ramesh M. Gulrajani, who passed away unexpectedly while the manuscript was still an early draft. We gratefully dedicate this paper to our deceased colleague.

We would like to thank the editors and the anonymous reviewers for their thoughtful comments and suggestions, Éric Bélanger for the initial implementation of the BICGSTAB solver, and several colleagues for proofreading our manuscript. Computations were performed at the Réseau québécois de calcul de haute performance (RQCHP).

Chapter 3

Validation of a simple model for the morphology of the T wave in unipolar electrograms

Preface

This chapter was previously published, in a slightly different form, as Mark Potse, Tobias Opthof, and Ruben Coronel: Validation of a simple model for the morphology of the T wave in unipolar electrograms. *Am. J. Physiol. Heart Circ. Physiol.*, 297:H792–801, 2009. doi:10.1152/ajpheart.00064.2009.

The paper was intended to settle a debate on the determination of local repolarization times from unipolar electrograms, by not only demonstrating the relation between local repolarization and signal features, but also explaining it using a simple model. The simple model could even explain why previous studies had found correlations (but not identities) with other signal features. To prove the correctness of the simple model we compared its results to a realistic model for which the simulation code and model anatomy presented in Chapter 2 were used.

Summary

Local unipolar electrograms (UEG) permit assessment of local activation and repolarization times at multiple sites simultaneously. However, UEG-based indices of local repolarization are still debated, in particular for positive T waves. Previous experimental and computer modeling studies have not been able to terminate the debate. In this study we validate a simple theoretical model of the UEG and use it to explain how repolarization statistics in the UEG relate to those in the action potential. The model reconstructs the UEG by taking the difference between an inverted local action potential and a position-independent "remote" signal. In normal tissue, this extremely simple model predicts T-wave morphology with surprising accuracy, while explaining in a readily understandable way why (1) the instant of repolarization is always related to the steepest upstroke of the UEG, both in positive and negative T waves, and (2) positive T waves are related to early-repolarizing sites while negative T waves are related to late-repolarizing sites.

3.1 Introduction

Measurement of repolarization time from the unipolar electrogram (UEG) is important for clinical studies of repolarization abnormalities, as well as for experimental studies. It is therefore important to understand how the T wave in the electrogram relates to local repolarization time. The ongoing debate on repolarization measurement in positive T waves [48, 49, 138, 233, 234] demonstrates that this understanding is incomplete.

Wyatt et al. [231] proposed to use the instant of steepest upstroke (T_{up}) of the T wave in the UEG as an index of local repolarization. Several studies have confirmed the validity of this method theoretically [41, 42, 83, 199] and experimentally [39, 48, 83, 130]. However, others have proposed that for positive T waves the instant of steepest downstroke (T_{down}) should be used [37, 66, 235]. The T-wave apex has also been used as an estimate for repolarization time [193].

The current mechanistic insight in the relation between T_{up} and repolarization is based on theoretical studies in a one-dimensional cable model [41, 42, 83, 199]. This explanation cannot be extended easily to arbitrary repolarization patterns in the 3-D heart. Numerical evaluations with realistic 3-D heart models have confirmed that theoretically T_{up} is the best index of repolarization even in the complex situation of a complete 3-D heart [41, 42, 166, 167], but the overwhelming complexity of the computational techniques inhibits a clear explanation.

We propose a simple UEG model that gives clear insight in repolarization phenomena. This model approximates the UEG by subtracting the local action potential (AP) from a position-independent signal which we name the "remote component." The purpose of this paper is to demonstrate that this model is accurate enough to predict the most important repolarization statistics, and that it can be used to understand how these statistics relate to the underlying AP. To show the validity and limitations of the simple model, simulated UEGs were compared with UEGs simulated by a realistic numerical model of the intact human heart.

3.2 Materials and Methods

Action potentials were simulated with a large-scale computer heart model that has been described and validated previously [168, 211]. This model has anisotropic myocardium with transmurally rotating fiber orientation. Sinus rhythm was mimicked by stimulating the ventricles at the early activation sites published by Durrer et al. [59, 119]. Propagating AP were computed at 15 million points in the ventricular myocardium with a monodomain reaction-diffusion equation, based on ionic currents computed with the TNNP model for the human ventricular myocyte [205], which distinguishes endocardial, mid-myocardial, and epicardial cells. Differences between the left ventricle (LV) and right ventricle (RV) [55, 224] were implemented as detailed in Table 3.1.

The anatomy of the model is illustrated in Figure 3.1. The atria were not activated, but were included in the simulation of electrograms to allow the reference potential to be set to zero at the roof of the right atrium [168]. Ventricular and atrial cavities were filled with blood.

Two different models were used for the computation of electrograms: a "realistic model" and a "simple model."

	LV epi	LV M	LV+RV endo	**RV M**	**RV epi**
G_{to} (nS/pF)	0.294	0.294	0.073	**0.504**	**0.882**
G_{Ks} (nS/pF)	0.245	0.062	0.245	**0.112**	**0.490**
APD (ms)	272	324	275	303	244

Table 3.1: *Selected parameters of the ionic model and APD of isolated cells. Parameter values that are different from the original TNNP model [205] are printed in bold type. The affected parameters are the maximal conductances of the transient outward current (G_{to}) and the slow delayed rectifier current (G_{Ks}) [205]. APD = action potential duration at steepest downstroke of the AP. APD was measured at 1000 ms cycle length. Units are nS = nanoSiemens, pF = picoFarad, ms = millisecond.*

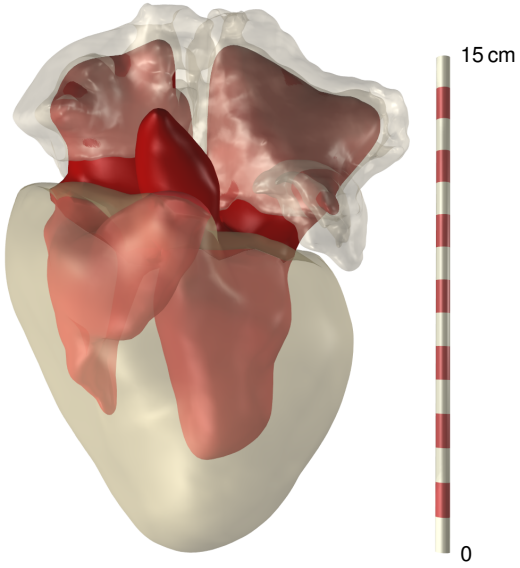

Figure 3.1: *Anatomy of the heart model used in this study. Ventricular and atrial cavities as well as the aorta were filled with blood. Atrial myocardium was included as a passive conductor.*

realistic model

Let $V_m(\mathbf{x}, t)$ be the membrane potential at time t and position $\mathbf{x}$ (boldface symbols are used to indicate vector quantities). The local UEG according to the realistic model, $\phi_e(\mathbf{x}, t)$, was computed from V_m throughout the heart by solving the bidomain equation [168,220] in the form of Equation 3.9 given in the Appendix, with the additional condition that $\phi_e(\mathbf{y}, t) = 0$ at the reference electrode site, $\mathbf{y}$, in the right atrium. By solving this equation, $\phi_e(\mathbf{x}, t)$ was obtained at 35 million model points in the ventricular myocardium, atria, connective tissue, and intracavitary blood. To allow analysis of temporal derivatives, error tolerance levels were chosen 100 times lower than previously reported [168]. To limit the consequent increase in computation time, we chose a lower spatial resolution of 0.25 mm for computation of both AP and electrograms. The resulting errors in propagation velocity were compensated by choosing 15 % higher values for the conductivity in the intracellular domain. Nominal conductivity values were taken from literature [186]. The adapted conductivities were $g_{eT} = 0.12$, $g_{eL} = 0.30$, $g_{iT} = 0.035$ and $g_{iL} = 0.33$ Siemens/m, with subscript 'e'

for the extracellular domain, 'i' for the intracellular domain, 'T' for transverse, and 'L' for longitudinal. The intracavitary blood had conductivity 0.6, connective tissue and atrial myocardium 0.2 Siemens/m.

simple model

We define $S(\mathbf{x},t)$, the simple model for the UEG at a point $\mathbf{x}$ as a function of time t, as the difference between a position-dependent "local component," $L(\mathbf{x},t)$, and a position-independent "remote component," $R(t)$:

$$S(\mathbf{x},t) = L(\mathbf{x},t) - R(t). \tag{3.1}$$

The names of these components reflect that $L(\mathbf{x},t)$ is completely determined by local activity, while $R(t)$ is dominated by remote activity. The local component, $L(\mathbf{x},t)$, is defined as a scaled and inverted local membrane potential:

$$L(\mathbf{x},t) = -\frac{g_\mathrm{i}}{g_\mathrm{i}+g_\mathrm{e}}\, V_\mathrm{m}(\mathbf{x},t) \tag{3.2}$$

where g_e and g_i represent the conductivities of the extracellular and intracellular domains, respectively. For the simple model, these conductivities are assumed to be isotropic. The rationale for Equation 3.2 is given in the Appendix. The remote component is obtained by comparison to $\phi_\mathrm{e}(\mathbf{x},t)$ computed by the realistic model, as follows. First we compute a residual signal, $r(\mathbf{x},t)$, for each location

$$r(\mathbf{x},t) = L(\mathbf{x},t) - \phi_\mathrm{e}(\mathbf{x},t). \tag{3.3}$$

This signal contains the effects of anisotropy, inhomogeneities, and tissue boundaries, but it is dominated by the differential effect of activity throughout the myocardium on the positive (exploring) and negative (reference) electrodes. To single out the global effect, we take the average, $R(t)$, of $r(\mathbf{x},t)$ obtained from a large number of different locations $\mathbf{x}$. We will show that $r(\mathbf{x},t)$ from different sites are similar, so that approximating them by the average $R(t)$ has little effect on $S(\mathbf{x},t)$. $R(t)$ can be computed directly from membrane potentials throughout the heart. A derivation based on lead field theory [67,68,125] is presented in the Appendix.

To facilitate the discussion, we introduce a signal V_rm that can be compared to membrane potentials:

$$V_\mathrm{rm}(t) = -\frac{g_\mathrm{i}+g_\mathrm{e}}{g_\mathrm{i}}\, R(t). \tag{3.4}$$

In the Appendix we demonstrate that $V_\mathrm{rm}(t)$ can be considered as a (weighted) average of $V_\mathrm{m}(\mathbf{x},t)$ over the surface that bounds the myocardium.

We now reformulate our definition of the simple model as follows:

$$S(\mathbf{x},t) = -\frac{g_\mathrm{i}}{g_\mathrm{i}+g_\mathrm{e}}\left[V_\mathrm{m}(\mathbf{x},t) - V_\mathrm{rm}(t)\right]. \tag{3.5}$$

For the fraction $g_\mathrm{i}/(g_\mathrm{i}+g_\mathrm{e})$ the value 0.25 was chosen. This value is close to the ratio $g_\mathrm{iT}/(g_\mathrm{iT}+g_\mathrm{eT})$ in the realistic model. This model is based on ideas that were independently published by Colli Franzone et al. [42] and by us [166], and is similar to a UEG model derived by Geselowitz [68] (see Appendix).

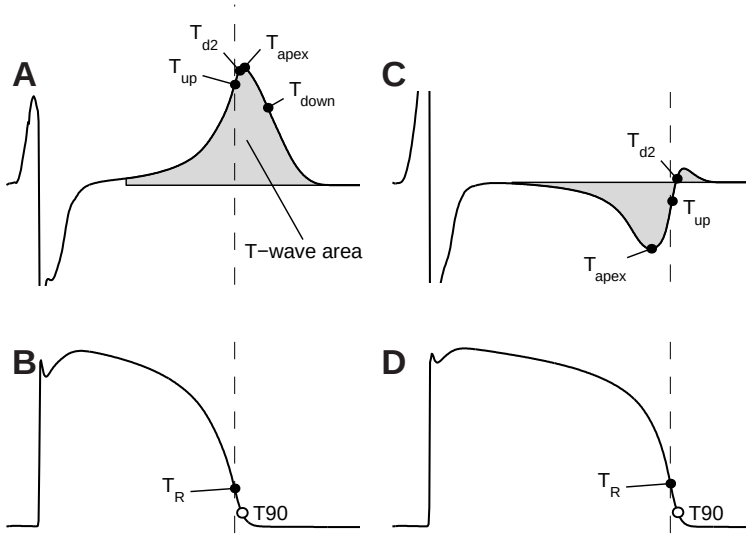

Figure 3.2: ***A,C:*** *Simulated UEG with illustration of the repolarization indices used; see text for their definitions.* ***B,D:*** *Simulated AP at the same locations as A and C, respectively, illustrating the reference markers. The dashed line in each panel marks the local* T_R.

statistics

The AP and UEG were analyzed at 10^4 randomly selected sites throughout the ventricular myocardium. From each simulated AP, repolarization time (T_R) and the instant of 90 % repolarization (T90) were determined and used as reference timings. T_R was defined as the instant of minimum first derivative (steepest downstroke) of the AP. In addition, the activation time T_A was defined as the instant of maximum first derivative (steepest upstroke) of the AP. Action potential duration (APD) was computed as $T_R - T_A$.

From the UEG at the same location we determined T_{up}, T_{down}, the instant of the T-wave apex (T_{apex}) [193], and the instant of minimum second derivative (T_{d2}), which has recently been reported to be related to T90 [41]. First, T-wave signs were determined. There is a continuous spectrum of positive, biphasic, and negative T waves in the UEG. To classify T waves as positive or negative, we evaluated the area under the electrogram, from 50 ms after the end of depolarization (the latest T_A) to the end of the simulation. A T wave was considered positive when the positive area exceeded the negative area. T_{up} and T_{down} were evaluated as the instants of maximum and minimum first derivative of the UEG, respectively, in the interval from 50 ms after the end of depolarization to the end of the simulation. For positive T waves, T_{down} was evaluated in the interval from T_{up} to the end of the simulation. The repolarization markers are illustrated in Figure 3.2. Analysis of the UEG was the same for the Simple and Realistic models. All statistics were determined automatically by a computer program. No manual corrections were made.

Computation and analysis of ϕ_e and S was done at a 1-ms sampling rate. Therefore, timing results are expressed with 1-ms accuracy.

The difference between the realistic and simple UEGs at a site $\mathbf{x}$ was quantified using

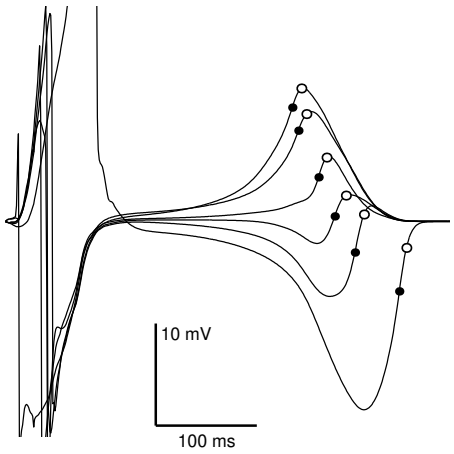

Figure 3.3: *Simulated UEGs (realistic model) from various sites in the ventricular myocardium. Local T_R are indicated with solid dots; local T90 with circles.*

the relative difference (RD) [216] defined as

$$\mathrm{RD}(\mathbf{x}) = \sqrt{\frac{\sum_t (S(\mathbf{x},t) - \phi_e(\mathbf{x},t))^2}{\sum_t \phi_e(\mathbf{x},t)^2}} \tag{3.6}$$

where the time index $t = 1, \ldots, 500$ ranges over all samples (depolarization and repolarization). The RD is a dimensionless measure of the difference between two signals (S and ϕ_e in our case); it is zero if the signals are identical.

3.3 Results

Predictions of the realistic model

To show the rationale for developing the simple model, we briefly review results obtained with the realistic model. These results summarize and expand previously reported findings [166,167] and confirm results from studies with smaller-scale models [41,42,83,199].

Figure 3.3 shows a representative sample of UEGs from the ventricular myocardium. Local repolarization times (T_R) are indicated with solid dots in the electrograms. These are invariably located on the upslope of the T wave.

In sinus rhythm, positive T waves were found in 44 % of the analyzed positions (Table 3.2). Their average T_R was 40 ms earlier than that of negative T waves. In Figure 3.4, panel A, T_R distribution is shown separately for positive and negative T waves. Clearly, positive T waves are generally associated with earlier repolarization than negative T waves. There is overlap between the distributions, reflecting the fact that repolarization time is associated with a continuous spectrum of T-wave configurations from entirely positive, through biphasic, to entirely negative. This is illustated in panel B of Figure 3.4, using (signed) T-wave area as a single parameter to describe the configuration.

The performance of T_{up} in sinus rhythm is illustrated in Figure 3.4, panel C. On 1000 points shown in the figure, 8 outliers are seen; the other points lie within a few milliseconds from the identity line.

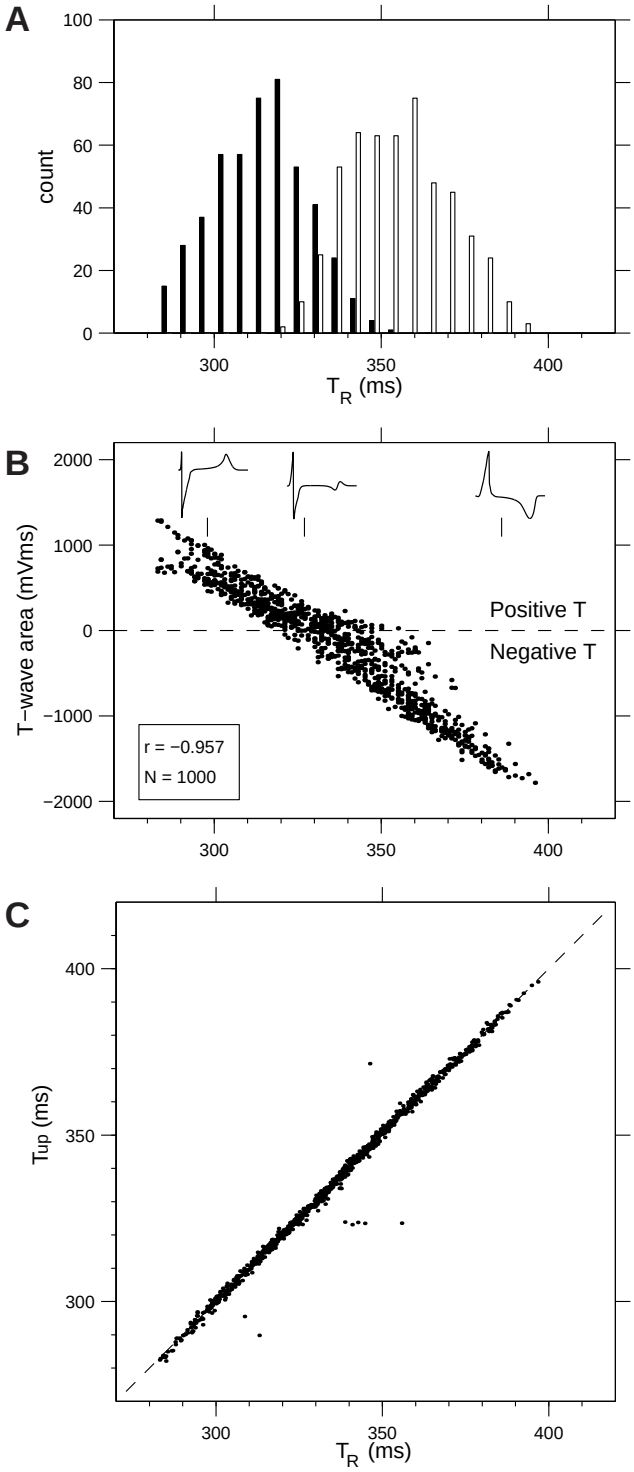

Figure 3.4: ***A:*** *Distribution of T_R for positive T waves (black bars) and for negative T waves (white bars); $N = 10^4$.* ***B:*** *scatter plot demonstrating the correlation between T_R and T-wave area; $N = 1000$. Three insets show typical UEGs whose T_R are indicated with vertical lines. The horizontal axis is the same as in panels A and C.* ***C:*** *scatter plot demonstrating the relation between T_R and T_{up}; $N = 1000$.*

	positive T	negative T
N	4376 (44 %)	5624 (56 %)
$T_{\mathrm{up}} - T_{\mathrm{R}}$	-0.1 ± 2.3 ms	0.7 ± 1.8 ms
$T_{\mathrm{down}} - T_{\mathrm{R}}$	28.7 ± 8.1 ms	n.a.
$T_{\mathrm{d2}} - \mathrm{T90}$	-2.6 ± 1.4 ms	-2.5 ± 2.3 ms
$T_{\mathrm{apex}} - \mathrm{T90}$	2.8 ± 1.9 ms	-29.0 ± 10.7 ms

Table 3.2: *Comparison of repolarization indices. Values are mean ± standard deviation. N is the number of measurement locations.*

The performance of T_{up}, T_{down}, T_{d2}, and T_{apex} on a sample of 10^4 randomly chosen sites throughout the ventricular myocardium, in sinus rhythm, is summarized in Table 3.2. The table shows that T_{up} is a very accurate substitute for T_{R}. An alternative for T_{up} in positive T waves, T_{d2} predicts T90 reasonably well. In positive T waves, the performance of T_{apex} is similar to that of T_{d2} but with an opposite bias, whereas T_{down} performs very poorly.

Pacing in the left ventricular apex caused repolarization to move predominantly from apex to base. This led to 85 % positive T waves and increased the difference in average T_{R} between positive and negative T waves to 70 ms. The accuracy of T_{up}, T_{down}, and T_{apex} as predictors for repolarization time was not affected (changes less than 1 ms). In a model with uniform intrinsic APD (all cells set to type endocardial; see Table 3.1) 49 % of the T waves was positive and the difference in average T_{R} between positive and negative T waves was reduced to 31 ms (from 40 ms in sinus rhythm), but the accuracy of the repolarization indices was again not affected.

Remote component for the simple model

Residuals $r(\mathbf{x}, t)$ computed according to Equation 3.3 for 100 randomly chosen myocardial sites are plotted in Figure 3.5, panel A, together with their average. Although individual signals differ, the average gives a reasonable estimate of their individual shapes, especially during repolarization. To obtain a smooth signal, we used the average R from 10^4 randomly chosen sites to compute UEGs with the simple model.

Validation of the simple model

Examples of UEGs computed according to the simple model (Equation 3.5) are shown in Figure 3.5, panels B–E. These examples were chosen to illustrate a representative set of relative differences (RD) between the simple and realistic models. Figure 3.5, panel F, shows that the vast majority of the 1000 sampled sites had acceptable RD values. As expected with this highly simplified model, there were several bad matches as well. These typically occurred in thin trabeculae, where realistic UEGs have small amplitudes and are more influenced by remote activity. The simple model cannot account for this. The simple and realistic models agreed on the polarity of the T wave in 90 % of the 10^4 analyzed positions.

The performance of the simple model was similar for different activation and repolarization sequences. The median RD was 0.29 in sinus rhythm, 0.23 for apical pacing,

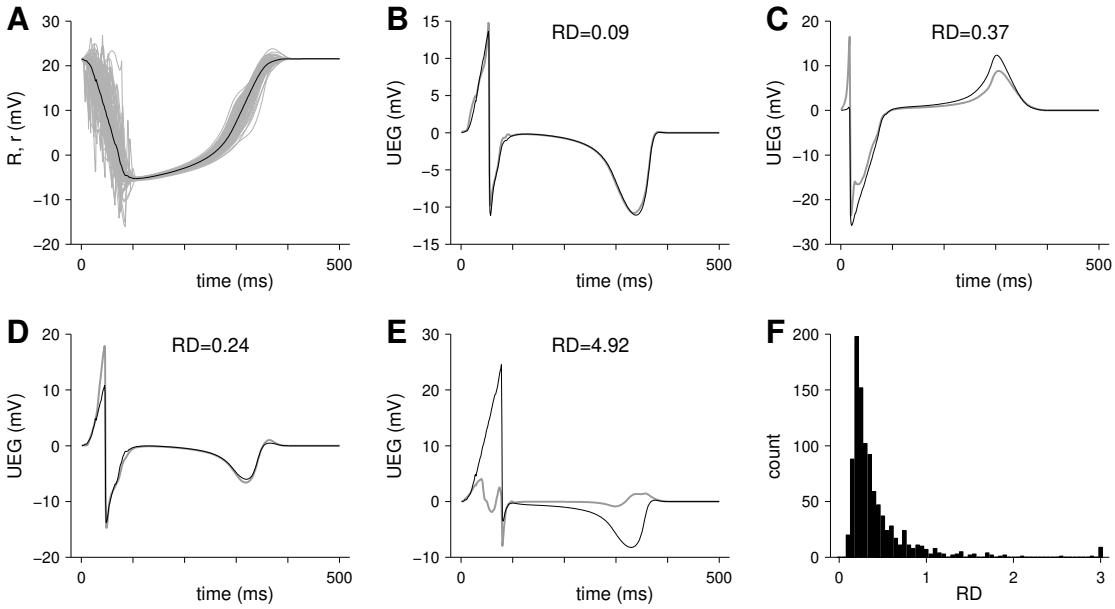

Figure 3.5: ***Panel A:*** *Determination of the remote component R. Gray lines: $r(\mathbf{x}, t)$ computed for 100 individual sites. Black line: average of these 100 signals.* ***Panels B–E:*** *UEG computed with the simple model (black) compared to the realistic model (gray). Positions were selected to show:* ***(B)*** *the best match;* ***(C)*** *a median match with positive T wave;* ***(D)*** *a median match with negative T wave; and* ***(E)*** *the worst match. The vertical axis gives potential (mV). Each panel gives the corresponding relative difference (RD).* ***Panel F:*** *frequency distribution of RD values over a sample of 1000 comparisons. The last bin represents RD $\geq$ 3.*

and 0.31 for left ventricular epicardial pacing ($N = 1000$). In a model with uniform intrinsic APD, the median RD was 0.32 for sinus rhythm.

Insights from the simple model

The upper two rows of Figure 3.6 show how the UEG is constructed according to the simple model. The UEG is computed as the inverted and downscaled difference between V_m and V_rm (Equation 3.5); it is positive when V_m is more negative than V_rm (blue area) and negative when V_m is more positive than V_rm (red area). Thus, positive T waves must occur at early-repolarizing sites.

The third row of signals in Figure 3.6 shows how the simple model compares to the realistic model.

The fourth row in Figure 3.6 shows how the simple model can help us to understand the proposed repolarization indices T_up and T_down. It shows the temporal derivatives of the V_m and V_rm signals. We will use the notation $\dot{V}$ to indicate the temporal derivative dV/dt. A dashed trace shows $\dot{V}_\mathrm{rm}$ and a solid trace shows $\dot{V}_\mathrm{m}$. The minimum of $\dot{V}_\mathrm{m}$ defines T_R, which is indicated by a red vertical line. Coincident with this line is a dashed black vertical line, which indicates T_up, the instant of maximum $\dot{S}$. The (near) equality of T_R and T_up can be understood by observing that the maximum of $\dot{S}$, which is proportional to $\dot{V}_\mathrm{rm} - \dot{V}_\mathrm{m}$, always occurs near minimum $\dot{V}_\mathrm{m}$,

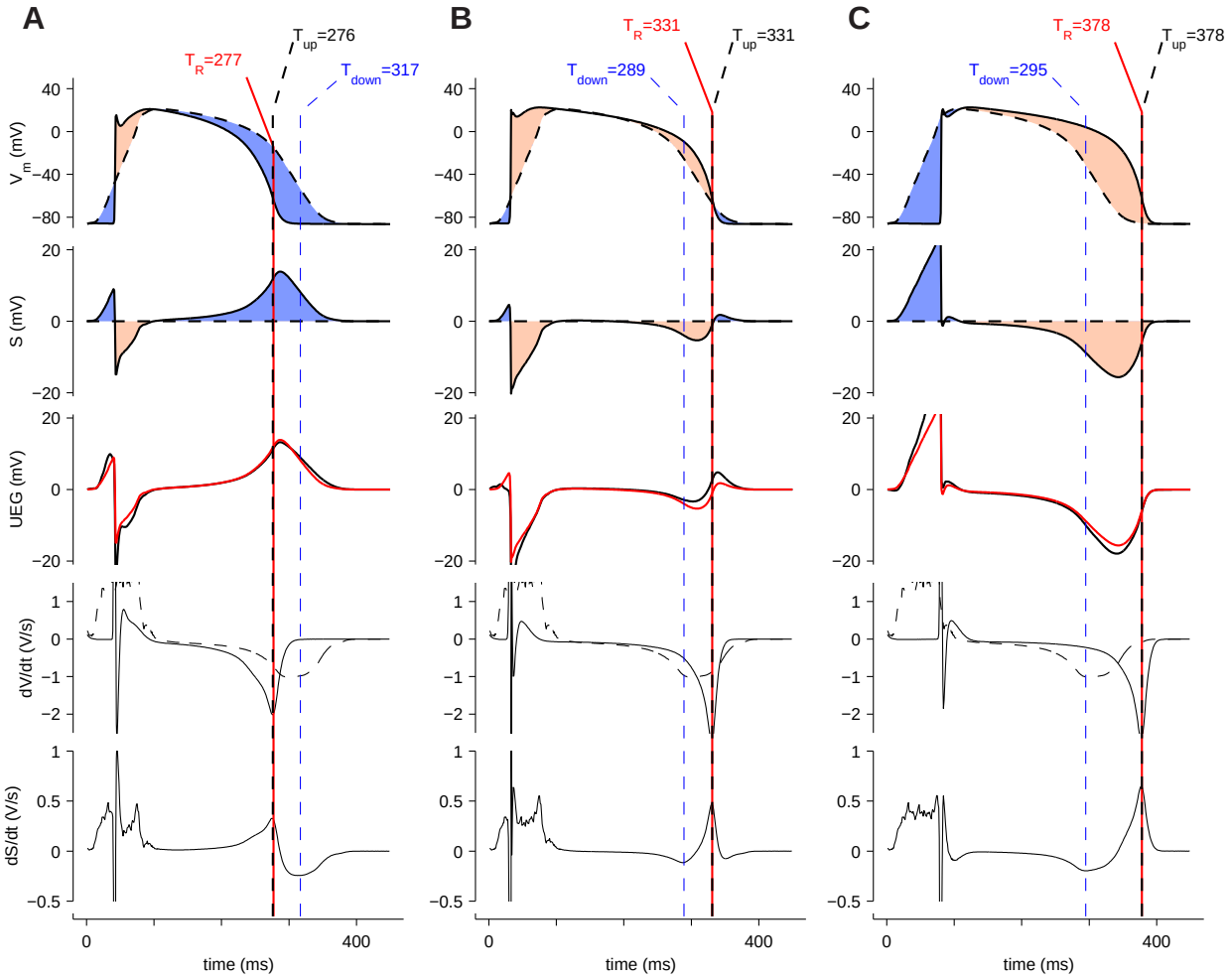

Figure 3.6: *Construction of UEGs with the simple model. The top frame in each panel shows simulated V_m from three different locations in the model (solid line) and the location-independent V_rm (dashed). The second frame shows their downscaled and inverted difference, i.e. the UEG according to the simple model. In the third frame, this UEG (red) is compared to the UEG computed with the realistic model (black). The fourth frame shows the temporal derivatives $\dot{V}_\mathrm{m}$ (solid line) and $\dot{V}_\mathrm{rm}$ (dashed). The fifth frame shows the temporal derivative of the UEG itself (computed with the simple model). Each red vertical line indicates T_R, i.e. the instant of minimum $\dot{V}_\mathrm{m}$. Each of these lines is half obscured by a dashed black line which indicates T_up, leading to a black-red dashed line. Each dashed blue vertical line indicates T_down. **Panel A:** positive T wave. **Panel B:** biphasic T wave. **Panel C:** negative T wave.*

due to the soft slopes of V_rm. Thus, in normal tissue, the remote component does not perturb T_up much.

The fifth row in Figure 3.6 shows $\dot{S}$ itself. Its extrema, which define T_up and T_down, occur near the minima of V_m and V_rm, respectively, but generally do not coincide exactly with these.

T_down occurs where the difference $\dot{V}_\mathrm{rm} - \dot{V}_\mathrm{m}$ is most negative. At very early repolarizing sites (panel A in Figure 3.6) T_down occurs well after the end of the local AP and corresponds with the minimum in $\dot{V}_\mathrm{rm}$. At less early sites, it still occurs after

the end of the AP, because $\dot{V}_{\mathrm{rm}}$ can only dominate the difference when V_{m} is nearly back at resting potential. At sites with intermediate repolarization times, $\dot{V}_{\mathrm{rm}}$ and $\dot{V}_{\mathrm{m}}$ together determine T_{down}. Both experimental [235] and numerical [166] studies have previously shown a (weak) correlation between T_{down} and repolarization time but a theoretical explanation has been lacking. The simple model readily explains this relation, also showing why it has a variable, non-unitary slope.

The T_{d2} index can be easily understood as well. T_{d2} is defined as the instant of minimum $d^2\phi_{\mathrm{e}}/dt^2$, i.e. most downward curvature in ϕ_{e}. According to the simple model, this corresponds to the most upward curvature in V_{m}, if distortion from V_{rm} is negligible. This upward curvature occurs at the end of the AP, near T90 in healthy myocardium. Because V_{rm} is a very smooth signal, its curvature is indeed negligible. This explains the small difference between T_{d2} and T90 (Table 3.2). In positive T waves, the sharp turn in ϕ_{e} leads in most cases to the apex of the wave. Thus, in positive T waves, T_{apex} is close to T_{d2}.

We reported above that during apical pacing in the realistic model, 85 % of the myocardium showed positive T waves, while this was 44 % in sinus rhythm. The simple model explains this finding too. When the heart was paced at the apex, the basal region repolarized last. Because the reference electrode was near the base, this region was more strongly represented in V_{rm}, and its late repolarization prolonged V_{rm}. Since the majority of sites now repolarized earlier than V_{rm}, a majority of T waves became positive. During sinus rhythm positive T waves were a minority. An explanation for this is given in the Appendix: under the assumption that the myocardium is isotropic, only sites at the surface of the myocardium contribute to V_{rm}. In the anisotropic heart this is not strictly true, but the surface still dominates. In sinus rhythm, the mid-myocardium was the last to repolarize. Due to the small influence of this late-repolarizing tissue, repolarization of V_{rm} during sinus rhythm occurred somewhat earlier than the average of the myocardium, making a larger volume of myocardium appear late-repolarizing and having negative T waves.

Although T_{up} and T_{R} are closely related, they do not coincide exactly. This can be understood in terms of the simple model as follows. In Figure 3.7, the signals $\dot{V}_{\mathrm{m}}$ and $\dot{V}_{\mathrm{rm}}$ are plotted in a short interval around T_{R}. These signals correspond to the first column in Figure 3.6. In this case, T_{R} (the instant of minimum $\dot{V}_{\mathrm{m}}$) was 277 ms and T_{up} (the instant of maximum $\dot{S}$) was 276 ms. The reason for this difference is that $\dot{S}$ is determined by both $\dot{V}_{\mathrm{m}}$ and $\dot{V}_{\mathrm{rm}}$: From Equation 3.5 it follows that $\dot{S}(\mathbf{x}, t)$ is proportional to $\dot{V}_{\mathrm{rm}}(t) - \dot{V}_{\mathrm{m}}(\mathbf{x}, t)$. In the case of Figure 3.7, the second derivative of V_{m} was smaller than the second derivative of V_{rm} during a full sample interval before T_{R}, as shown by the tangent lines. Therefore, the difference $\dot{V}_{\mathrm{rm}} - \dot{V}_{\mathrm{m}}$ was slightly larger at $t = 276$ ms than at $t = T_{\mathrm{R}}$.

3.4 Discussion

We have shown that in healthy tissue the local contribution to the UEG is essentially a downscaled inverted AP. The electrogram is positive when local V_{m} is more negative than V_{rm}. This explains why T waves are positive for early-repolarizing cells. Cells with intermediate repolarization times have a V_{m} that initially stays above V_{rm}, but descends below it in the final stage of repolarization. This explains their biphasic T waves. As observed experimentally [48, 83], such biphasic waves always have a

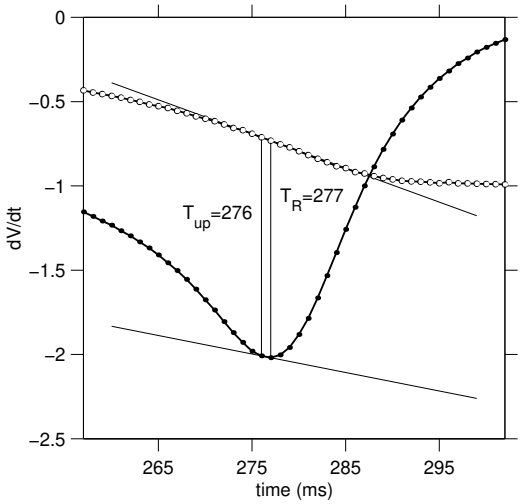

Figure 3.7: *Illustration of difference between T_{up} and T_{R}. The first derivative of the membrane potential, $\dot{V}_{\mathrm{m}}$, at the same location as the leftmost column in Figure 3.6, is shown with solid dots, connected with line segments (1-ms sampling interval). The signal $\dot{V}_{\mathrm{rm}}$ is shown similarly with open circles. Computed tangent lines to both signals at $t = T_{\mathrm{R}} - 0.5\,ms$ demonstrate that the second derivative of V_{rm} at this time is larger than the second derivative of V_{m}, leading to a difference of 1 ms between T_{up} and T_{R}.*

negative part followed by a positive part. In late-repolarizing regions the T wave is entirely negative because the local membrane is still depolarized while it is repolarized elsewhere.

Due to the relatively soft slopes of V_{rm}, first- and second-order derivatives of the UEG are dominated by the derivatives of V_{m}. Thus, where V_{m} makes its steepest descent, the UEG makes its steepest ascent. This explains the near-equality of T_{up} and T_{R}. Also, where V_{m} turns most sharply upward, the UEG turns most sharply downward. This explains the small difference between T_{d2}, T90, and, in positive T waves, T_{apex}. Only when V_{m} is very flat the slope of V_{rm} can dominate the slope of the UEG. This leads to a coincidence of T_{down} and the instant of minimum dV_{rm}/dt for very late- and very early-repolarizing sites. At sites with intermediate repolarization times, this relation is modulated by the slope of the local V_{m}, leading to a (weak) correlation between T_{R} and T_{down}.

The ARI and alternatives

Wyatt et al. proposed the activation-recovery interval (ARI) as a substitute for the APD, which cannot easily be measured in vivo [231]. The ARI was measured from the time of steepest downstroke of the UEG to the time of steepest upstroke of its T wave. Comparison with transmembrane APD and with effective refractory period demonstrated the validity of this method [39, 48, 83, 130]. A simulation study with a cable model also confirmed the method, and demonstrated some of the circumstances in which it is less accurate [199].

Other authors proposed that, for positive T waves, T_{down} should be used instead of T_{up} [37, 66, 235]. The original rationale for this "alternative method" was that

in some studies its results correlated better with the duration of the monophasic action potential [37,235]. The intuition that the end of the local T wave (i.e. T_{down} for positive T waves) should correspond to local T_{R} may also play a role.

Our simple model shows that in normal tissue, T_{up} is temporally linked to T_{R}. This (simple) model is not suitable for all conditions. For example, it cannot faithfully simulate UEGs in case of fibrosis or intracavitary measurements. It is possible that the relation fails there, e.g. because the active tissue is so sparse or so far from the exploring electrode that the slope of V_{rm} can dominate the slope of the UEG, or because the tissue is too anisotropic. However, it is difficult to imagine that under these conditions the relation between T_{R} and T_{up} would be replaced by a relation between T_{R} and T_{down}.

Another possible alternative for T_{up} is the T-wave area, which correlates strongly with T_{R} [166,222]. This relation may be useful as a last resort when T_{up} cannot be measured. However, caution is necessary because other factors may influence T-wave area. It may be a useful index if such problems can be ruled out, or in order to assess local changes in APD. When there is no opportunity for a quantitative analysis, the polarity of the T wave can give a coarse estimate of local repolarization time with respect to the average of the ventricular myocardium.

In model studies, T_{d2} too has shown potential as an estimate for T_{R} or T90, but its sensitivity to noise may limit its applicability in experimental or clinical studies [41]. For positive T waves, T_{apex} is equally accurate.

Sources of inaccuracy in the ARI

Generally, T_{up} and T_{R} will not be exactly the same, because the UEG has a remote component. At T_{R} itself, where $\dot{V}_{\mathrm{m}}$ is minimal, the second derivative of V_{m}, $\ddot{V}_{\mathrm{m}}$, is zero, so any signal component with a nonzero second derivative at T_{R} can modulate T_{up}. This displacement is limited to the interval in which the magnitude of $\ddot{V}_{\mathrm{m}}$ is smaller than that of the other components of the UEG. According to the simple model, the only other component is V_{rm}. Its second derivative, $\ddot{V}_{\mathrm{rm}}$, is generally small but not zero at T_{R}. If $\ddot{V}_{\mathrm{rm}} < 0$ at T_{R}, T_{up} will be earlier than T_{R}, and if $\ddot{V}_{\mathrm{rm}} > 0$ at T_{R}, T_{up} will be later than T_{R}.

In this study, the interval in which the absolute value of $\ddot{V}_{\mathrm{m}}$ is small enough to allow a difference between T_{up} and T_{R} was generally less than 2 ms long. However, in failing [178] or ischemic myocytes, the AP can have a long, linear downslope, i.e. a long interval in which the absolute value of $\ddot{V}_{\mathrm{m}}$ is small. This can lead to considerable differences between T_{up} and T_{R} [83,199]. The same problem occurs with atrial myocytes that lack a plateau in their AP [222].

Other ways to explain the UEG

Previous explanations of the validity of the ARI were based on propagation in a uniform cable, which is equivalent to plane-wave propagation in a uniform isotropic 3-D medium [83,199]. Under the assumption that the repolarization wavefront travels with a constant velocity and the final phase of the AP is temporally symmetric about T_{R}, a strict equivalence of T_{up} and the instant of minimum third temporal

derivative of V_m can be demonstrated [199]. A disadvantage of this approach is that the generalization to arbitrary repolarization sequences is not obvious.

Another UEG model that has been successful in providing insight is the oblique dipole layer [44]. Whereas this model is very useful in explaining anisotropic effects on the QRS complex, we think that it is not convenient for an explanation of the ARI and T-wave polarity.

The cable model can also be used to explain T-wave polarity. For depolarization wavefronts, this has been treated e.g. by Spach et al. [198]. With the signs inversed, this treatment is perfectly applicable to repolarization wavefronts. Just like the amplitude ratio of the R and S waves in the UEG contains information about depolarization time [54], the positive/negative amplitude ratio of the T wave gives information about repolarization time.

The remote component

The signal V_{rm} was obtained in an ad-hoc way. In the Appendix, we argue that it can be interpreted as an average membrane potential. This average is not calculated over the entire myocardium, but only over its surface. In addition, different cells contribute to it with different weights, and these weights depend on the position of the reference electrode. This is to be expected, since the location of the reference is known to influence the UEG shape substantially. However, the amplitude of V_{rm} is always similar to the AP amplitude, and its shape always represents a weighted average of remote AP.

Modeling techniques used

In our "realistic model," dispersion of AP shape was based on inhomogeneous expression of ion channels and subunits. Presently, these inhomogeneities are insufficiently characterized to explain the dispersion of AP shape in the human heart and to obtain normal T waves in the ECG [46,203,205]. However, the similarity of results obtained with the realistic model for different repolarization sequences demonstrates that a faithful representation of the true dispersion of AP shapes is not important for our study.

Conclusion

In normal myocardium, the UEG can be understood (approximately) as the difference between an inverted action potential and a remote component. With this simple model, the mechanism and limitations of all proposed repolarization markers can be readily explained. The relation between T_{up} and T_R, which has previously been established both theoretically and experimentally, can now be understood intuitively.

We confirm the conclusion that T_{up} is the best estimate of T_R, regardless of T-wave sign. T_{d2} and T_{apex} may sometimes be useful. T_{down} should never be used.

3.5 Acknowledgements

Computational resources for this work were provided by the Réseau québécois de calcul de haute performance (RQCHP).

This study was partially supported by the Netherlands Heart Foundation, grant nr. 2005B092.

M. Potse was partially supported by the Fonds de la recherche en santé du Québec (FRSQ), through the Research Center of Sacré-Coeur Hospital, Montreal, Quebec, Canada.

Appendix: Rationale for the Simple model

The bidomain model is the theoretical basis for almost all current modeling work in cardiac electrophysiology [67, 131, 154, 220]. It approximates the myocardium with two continuous domains. The "intracellular domain" represents the interior of myocytes and gap junctions, while the "extracellular domain" represents the interstitium. Intracavitary blood and connective tissue can be thought of as an extension of the extracellular domain [168]. The electric conductivity of each domain is represented by conductivity tensor fields $\mathbf{G}_\mathrm{i}$ and $\mathbf{G}_\mathrm{e}$, respectively. The bidomain model states that all current that leaves one domain at a given location must enter the other domain at the same location:

$$\nabla \cdot \mathbf{G}_\mathrm{i}(\mathbf{x})\, \nabla \phi_\mathrm{i}(\mathbf{x}, t) = -\nabla \cdot \mathbf{G}_\mathrm{e}(\mathbf{x})\, \nabla \phi_\mathrm{e}(\mathbf{x}, t) \tag{3.7}$$

where ϕ_i and ϕ_e are the intracellular and extracellular potential fields. Using the transmembrane potential

$$V_\mathrm{m}(\mathbf{x}, t) = \phi_\mathrm{i}(\mathbf{x}, t) - \phi_\mathrm{e}(\mathbf{x}, t) \tag{3.8}$$

the bidomain equation can be rewritten as

$$\nabla \cdot [\mathbf{G}_\mathrm{i}(\mathbf{x}) + \mathbf{G}_\mathrm{e}(\mathbf{x})]\, \nabla \phi_\mathrm{e}(\mathbf{x}, t) = -\nabla \cdot \mathbf{G}_\mathrm{i}(\mathbf{x})\, \nabla V_\mathrm{m}(\mathbf{x}, t). \tag{3.9}$$

This equation allows the computation of $\phi_\mathrm{e}(\mathbf{x}, t)$ from a known distribution of V_m. It only determines ϕ_e up to an arbitrary offset potential, which is fixed by defining $\phi_\mathrm{e}(\mathbf{y}, t)$ to be zero at the location, $\mathbf{y}$, of the reference electrode. Since Equation 3.9 is an implicit equation which must be satisfied for all $\mathbf{x}$, it can only be solved in general by computing ϕ_e throughout the heart at once by solving a large system of linear equations [168]. The realistic model employed in this study uses this method. This solution process can not be intuitively understood. To arrive at an equation that can be easily understood, we assume $\mathbf{G}_\mathrm{i}$ and $\mathbf{G}_\mathrm{e}$ to be homogeneous and isotropic, so that we can represent them by scalars g_i and g_e and write

$$(g_\mathrm{i} + g_\mathrm{e})\nabla^2 \phi_\mathrm{e}(\mathbf{x}, t) = -g_\mathrm{i} \nabla^2 V_\mathrm{m}(\mathbf{x}, t). \tag{3.10}$$

In the absence of boundaries, the general solution of this equation is

$$\phi_\mathrm{e}(\mathbf{x}, t) = -\frac{g_\mathrm{i}}{g_\mathrm{i} + g_\mathrm{e}} V_\mathrm{m}(\mathbf{x}, t) + \phi_\mathrm{off}(t) \tag{3.11}$$

where $\phi_{\text{off}}(t)$ is an undefined offset potential [157]. Due to the assumption of isotropy, this equation for 3-D tissue is the same as the expression for ϕ_e in the one-dimensional cable [78, 92, 157]. The first term in Equation 3.11 is our expression for the local component, $L(\mathbf{x}, t)$.

If we define the extracellular potential at a reference location, $\mathbf{y}$, to be zero: $\phi_e(\mathbf{y}, t) \equiv 0$, we find the following expression for the offset potential:

$$\phi_{\text{off}}(t) = \frac{g_i}{g_i + g_e} V_m(\mathbf{y}, t) \tag{3.12}$$

Thus, bipolar electrograms can be computed with Equation 3.11. For the UEG, a reference location in a passive medium (inactive tissue, blood, or perfusion fluid) must be used. This situation cannot be modeled realistically with an infinite-medium approach as used above. Therefore we seek to replace $\phi_{\text{off}}(t)$ in Equation 3.11 by a more general remote component $R(t)$ that can account for the inhomogeneities and boundaries of the body.

There are essentially two methods to compute UEGs in a bounded and inhomogeneous body. The first is to use a differential equation like Equation 3.9. This is the approach taken by the realistic model used in this study. As stated above, it has the disadvantage of providing little insight in the mechanisms underlying the UEG. The second method is based on integral rather than differential expressions. A suitable integral-based method was proposed by Geselowitz in a brief conference paper [68]; details of his derivations are given in earlier work [67]. The method is based on what is now called an "equivalent double layer" [217]. Assume that a current I_{app} is injected through an exploring electrode at a point $\mathbf{x}$ inside the myocardium, and leaves through a reference electrode located at a point $\mathbf{y}$ outside the myocardium. The resulting current field inside the body, including the myocardium, is denoted as $\mathbf{J}_{\mathbf{xy}}$. The field $\mathbf{J}_{\mathbf{xy}}/I_{\text{app}}$ is traditionally called the "lead field" [125] or "lead vector field" [156] for the given pair of electrodes. Assuming isotropic extracellular and intracellular media, the UEG, i.e., the potential difference between the two electrodes, $V_{\mathbf{xy}}$, can then be expressed as

$$V_{\mathbf{xy}} = -\frac{g_i}{g_i + g_e} \left[V_m(\mathbf{x}, t) + \frac{1}{I_{\text{app}}} \int_S V_m \mathbf{J}_{\mathbf{xy}} \cdot d\mathbf{S} \right] \tag{3.13}$$

where S is the surface of the active myocardium, over which the product of V_m and $\mathbf{J}_{\mathbf{xy}}$ is integrated [68]. Comparison with equations Equation 3.5 and Equation 3.11 confirms the expression for the local component, $L(\mathbf{x}, t)$, and identifies the term involving the surface integral as what we named the remote component $R(\mathbf{x}, t)$ of the UEG. It is not obvious from this expression that R depends little on the position of the exploring electrode. Therefore we calculated lead fields $\mathbf{J}_{\mathbf{xy}}$ (using the same software as for the realistic model [168]) and evaluated the expression

$$R_{\mathbf{x}_n\mathbf{y}} = -\frac{g_i}{g_i + g_e} \frac{1}{I_{\text{app}}} \int_S V_m \mathbf{J}_{\mathbf{xy}} \cdot d\mathbf{S} \tag{3.14}$$

for five different positions $\{\mathbf{x}_n,\ n = 1 \ldots 5\}$ of the exploring electrode and a reference electrode at location $\mathbf{y}$ in the left atrium. The results are shown in Figure 3.8, and demonstrate that $R_{\mathbf{y}}$ defined as the average of several $R_{\mathbf{x}_n,\mathbf{y}}$ would be a good approximation for each individual $R_{\mathbf{x}_n\mathbf{y}}$. For practical reasons, R used elsewhere in this

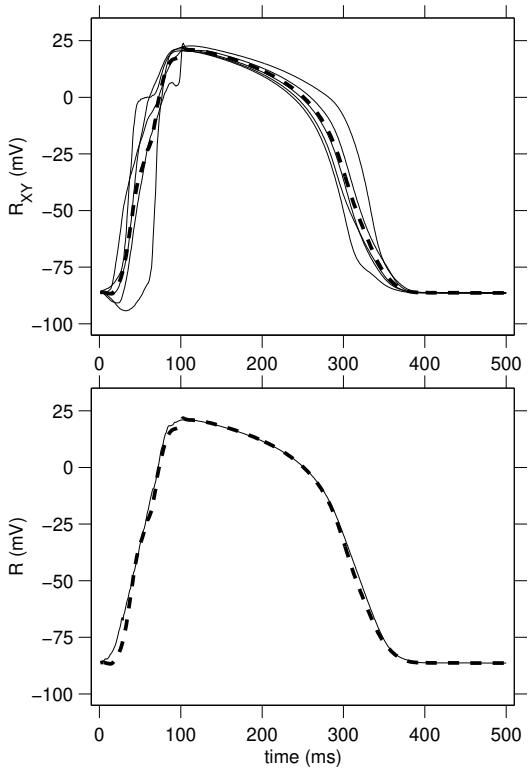

Figure 3.8: ***Panel A:*** *Thin solid lines show the remote component $R_{\mathbf{xy}}$ evaluated for a reference electrode in the left atrium and exploring electrodes (1) in the right ventricular subendocardium, (2) in the left-ventricular (LV) apical midmyocardium, (3) LV subendocardially in the tip of the septum, (4) LV basal subendocardial, and (5) LV posterior subepicardially at the level of the papillary muscles. The thick dashed line shows the average of these 5 signals.* ***Panel B:*** *The dashed line is the same as in panel A. The solid line is $R(t)$ according to the simple model (computed from residuals $r(\mathbf{x}, t)$ at many sites).*

paper was obtained by subtracting the local component, $L(\mathbf{x}, t)$ from $\phi_e(\mathbf{x}, t)$ computed with a realistic model, and averaging the difference over many locations $\mathbf{x}$. Panel B of Figure 3.8 shows that $R_{\mathbf{y}}$ and R are nearly identical. Since the purpose of our simple model is only to give insight, and not to replace the realistic model for numerical simulations, the actual method to arrive at R is not important.

From charge conservation, we must have

$$\int_S \mathbf{J_{xy}} \cdot d\mathbf{S} = I_{\text{app}} \ . \tag{3.15}$$

Thus, Equation 3.13 demonstrates that we can think of V_{rm} for any pair of electrodes at $\mathbf{x}$ and $\mathbf{y}$, which can be expressed as

$$V_{\text{rm}} = \frac{1}{I_{\text{app}}} \int_S V_{\text{m}} \mathbf{J_{xy}} \cdot d\mathbf{S} \tag{3.16}$$

as an average membrane potential, albeit with a weighting that depends on the reference location. Under the assumption of isotropy, only V_{m} at the surface of the myocardium contributes. Therefore V_{rm} does not reflect late repolarization of the

mid-myocardium [227]. In the anisotropic heart, the deeper myocardium does contribute to V_{rm}, but the surface still dominates.

In previous work, we have computed V_{rm} as a non-weighted average of V_{m} over the whole myocardium [166, 167]. The more general method employed here is more accurate, especially for abnormal repolarization sequences.

The simple model is not intended as an alternative for complete bidomain solutions, or competition for less crude approximations such as the oblique dipole model [44]. It is only a "rule of thumb" that allows us to explain how the UEG relates to action potentials. As such, it is similar to models that explain the electrocardiogram as a difference between two action potentials. Such models are used by many teachers of electrocardiography [16, 201].

Chapter 4

The Brugada sign cannot be explained without structural damage

Preface

This chapter is based on the article "Mechanism of right precordial ST-segment elevation in structural heart disease: Excitation failure by current-to-load mismatch" by Mark Hoogendijk et al. *Heart Rhythm*, 7:238-248, 2010. doi:10.1016/j.hrthm.2009.10.007 [97]. Parts of the article text were copied with only minor adaptations. Figures 4.1, 4.3 and 4.4 were composed by Dr. Mark Hoogendijk.

The original paper relied on numerous techniques and many authors to investigate the possible mechanisms of the Brugada sign in the ECG. This chapter describes the role of computer modeling in the article.

Summary

The Brugada sign has been associated with mutations in the SCN5A gene and with right ventricular structural abnormalities. Their respective roles in the Brugada sign and in the associated ventricular arrhythmias are unknown.

We aimed to delineate the role of structural abnormalities and sodium-channel dysfunction in the Brugada sign. We determined the activation and repolarization characteristics of the explanted heart of a patient with a loss-of-function mutation in SCN5A and dilated cardiomyopathy after induction of right-sided ST-segment elevation by ajmaline. Additionally, we simulated right ventricular structural discontinuities and sodium channel dysfunction in a computer model encompassing the heart and thorax.

In the explanted heart, disappearance of local activation in unipolar electrograms at the basal right ventricular epicardium was followed by monophasic ST-segment elevation. The local origin of this phenomenon was confirmed by coaxial electrograms. Neither early repolarization nor late activation correlated with the ST-segment elevation. At sites of local ST-segment elevation, the subepicardium was interspersed with adipose tissue and contained more fibrous tissue than either the left ventricle

or control hearts. In computer simulations entailing right ventricular structural discontinuities, reduction of sodium-channel conductance or size of the gaps between introduced barriers resulted in subepicardial excitation failure or delayed activation by source-sink mismatch and in the Brugada sign on the ECG.

We conclude that right ventricular excitation failure and activation delay by source-sink mismatch in the subepicardium can cause the Brugada sign and may underlie the ventricular arrhythmias in patients with the Brugada sign.

4.1 Introduction

The Brugada sign of right precordial ST-segment elevation followed by a negative T wave is associated with ventricular tachyarrhythmia and sudden cardiac death [6]. In the Brugada syndrome, it occurs in the absence of gross structural abnormalities [6]. However, the Brugada sign is not limited to structurally normal hearts. Right ventricular structural abnormalities have been demonstrated in a significant fraction of patients with the Brugada sign [47, 51, 64, 237]. Additionally, sodium channel blockers can provoke the Brugada sign in arrhythmogenic right ventricular cardiomyopathy [150] and Chagas' disease [38], conditions characterized by severe structural derangements. The role of the structural changes in the mechanism of the Brugada sign and the associated arrhythmias is unknown.

Thus far, two mechanisms have been proposed to explain Brugada-type ST elevation: 1) early repolarization [232] and 2) late activation [47, 212] in the right ventricular wall. Sodium channel function is important in both mechanisms because sodium channel blockers can provoke the Brugada sign [133] and loss-of-function mutations in the gene encoding the cardiac sodium channel (SCN5A) can be identified in about 20 % of patients with Brugada syndrome [6]. Neither hypothesis has been confirmed in patients [129].

Structural abnormalities can result in sites where a thin fiber connects to a much larger muscle mass. Such sites are susceptible to conduction block by source-sink mismatch, especially when the available sodium current (I_{Na}) is reduced [61, 127, 183, 192]. If excitation fails at these sites, the potential difference between excited and unexcited myocardium will still produce a current, too small to excite the distal tissue but maybe large enough to result in a measurable ST-segment elevation. Therefore, we hypothesized that right ventricular excitation failure by source-sink mismatch can cause the Brugada sign in patients with structural abnormalities, especially when I_{Na} is reduced by loss-of-function mutations in SCN5A or sodium channel blockade. To test this hypothesis, we determined the activation and repolarization characteristics of the explanted heart of a patient with a loss-of-function mutation in SCN5A and structural discontinuities in the setting of dilated cardiomyopathy, before and after the induction of ST-segment elevation by sodium channel blockade. To distinguish the roles of I_{Na} and structural discontinuities we simulated the effects of both in a numerical model of a human heart and torso.

4.2 Methods

Numerical simulations were crucial in the argument of this study. The following methods were used.

Propagating action potentials were simulated with a monodomain reaction-diffusion model (Equation 1.4) on a human ventricular geometry. The membrane dynamics were simulated using the human ventricular myocyte model proposed by Ten Tusscher et al. [205]. This model represents the differential characteristics of subendocardial, mid-myocardial, and subepicardial myocytes. The tissue was anisotropic, with transmural fiber rotation based on Streeter's rule [200]. The ECG was computed using a bidomain model of the human heart and torso, including lungs and intracavitary blood volumes. Structural discontinuities were simulated by the introduction of barriers (thickness 0.4 mm) in the outer 50 % of the right ventricular wall. In these barriers, no intercellular coupling was present, but the interstitium was unaffected. The barriers contained gaps of 0.2 mm width in which intercellular coupling was maintained, but reduced in steps from 100 % to 8 % of normal to simulate smaller gaps. Sodium channel conductivity (G_{Na}) was reduced in steps from 100 % to 20 % of normal in the entire heart. Single cardiac cycles were simulated in 12 hours on 128 processors of an SGI Altix 4700 supercomputer.

4.3 Results

The experimental results on the isolated heart showed neither signs of early repolarization nor late depolarization. Instead, monophasic ST-segment elevations were observed in the non-activated areas, and these coincided with the appearance of ST-segment elevation in the ECG.

The simulated ECG in the absence of structural abnormalities had a QRS duration of 80 ms and isoelectric ST segments (Figure 4.1A, black ECG). Reduction of G_{Na} in the normal heart to 30 % of normal delayed activation globally and increased the QRS duration to 130 ms, but did not lead to ST-segment elevation (Figure 4.1A, red ECG). The introduction of structural discontinuities with 30 % of the normal coupling in the gaps at normal G_{Na} resulted in a QRS prolongation to 100 ms and in negative T waves in the right precordial leads but not in ST-segment elevation (Figure 4.1B, black ECG). The negative T wave was caused by activation delay of the RV subepicardium (Figure 4.1C).

Reduction of G_{Na} after introduction of these structural discontinuities caused excitation failure at the anterior right ventricular subepicardium (Figure 4.1D, black sites). The current received from and given to surrounding elements and corresponding action potentials at five neighbouring sites in and immediately distal of the gaps are depicted in Figure 4.2. Subepicardial excitation failure occurred when the depolarizing current received distal of the structural discontinuities was insufficient to reach threshold potential. The potential gradient between the excited and unexcited myocardium caused ST-segment elevation in the right precordial leads. Activation at other right ventricular subepicardial sites was delayed, leading to a negative T wave in the right precordial leads (Figure 4.1B, red ECG).

In the presence of structural discontinuities with 30 % of the normal coupling in the gaps, the percentage of elements that were not excited throughout the cardiac cycle depended on G_{Na} and correlated well with the cumulative ST-segment elevation in V1 and V2 of the 3rd and 4th intercostal space. Both increased markedly when G_{Na} was reduced below 50 % of normal (Figure 4.3). Likewise, a decrease of the size of the gaps in the barriers at normal sodium conductance resulted in a reduction in

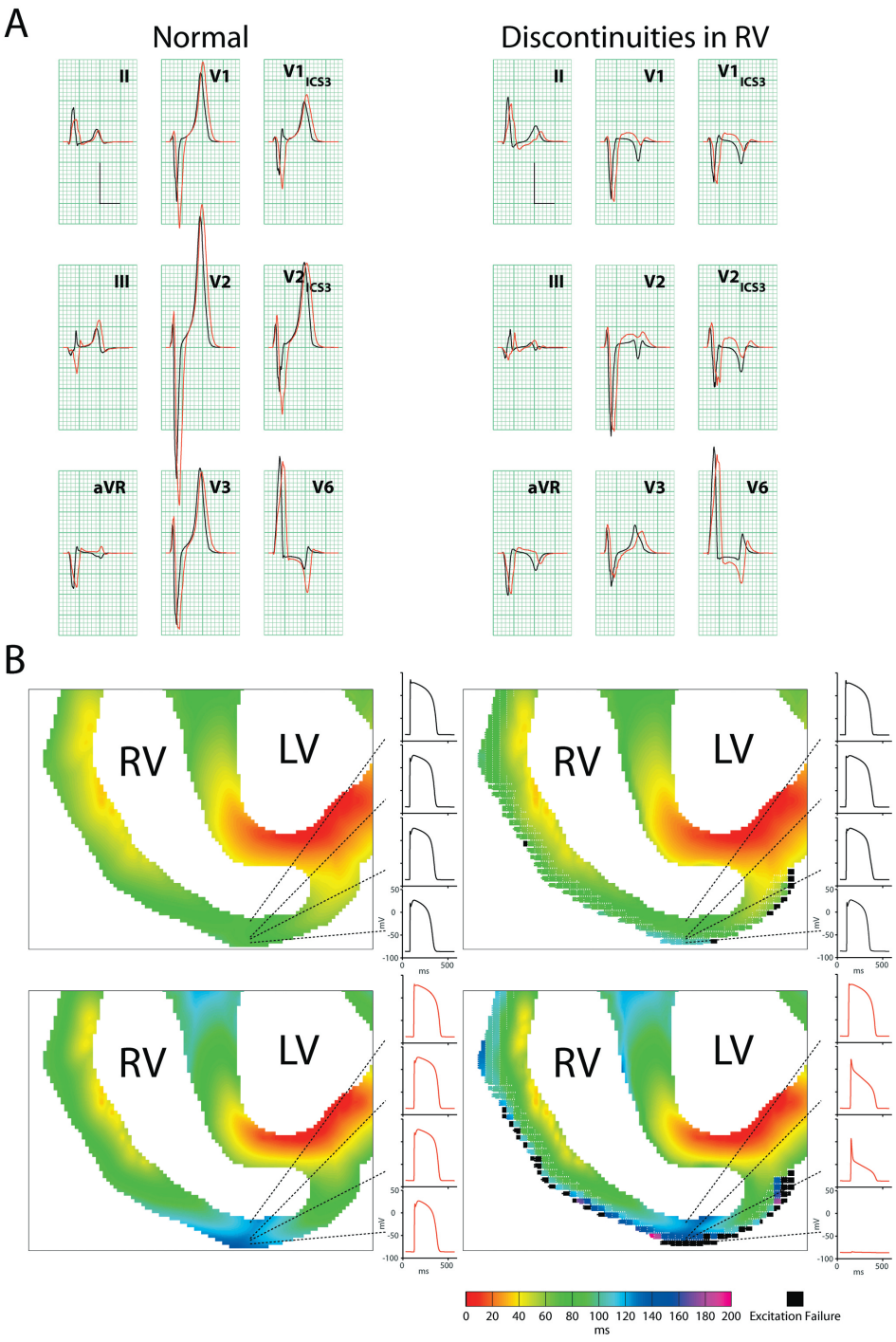

Figure 4.1: *Simulated subepicardial discontinuities and sodium channel dysfunction. **A**: ECGs of the heart without and with structural discontinuities in the right ventricular subepicardium at baseline (black) and after (red) reduction of G_{Na} to 30 % of normal. Grid squares 40 ms × 0.1 mV. **B**: Basal short-axis view of the heart with structural discontinuities at the right ventricular subepicardium before (left) and after (right) reduction of GNa to 30 % of normal. Colors indicate activation time; sites that failed to excite are shown in black. LV = left ventricle; RV = right ventricle. Action potentials at four sites proximal and distal to a barrier are also shown.*

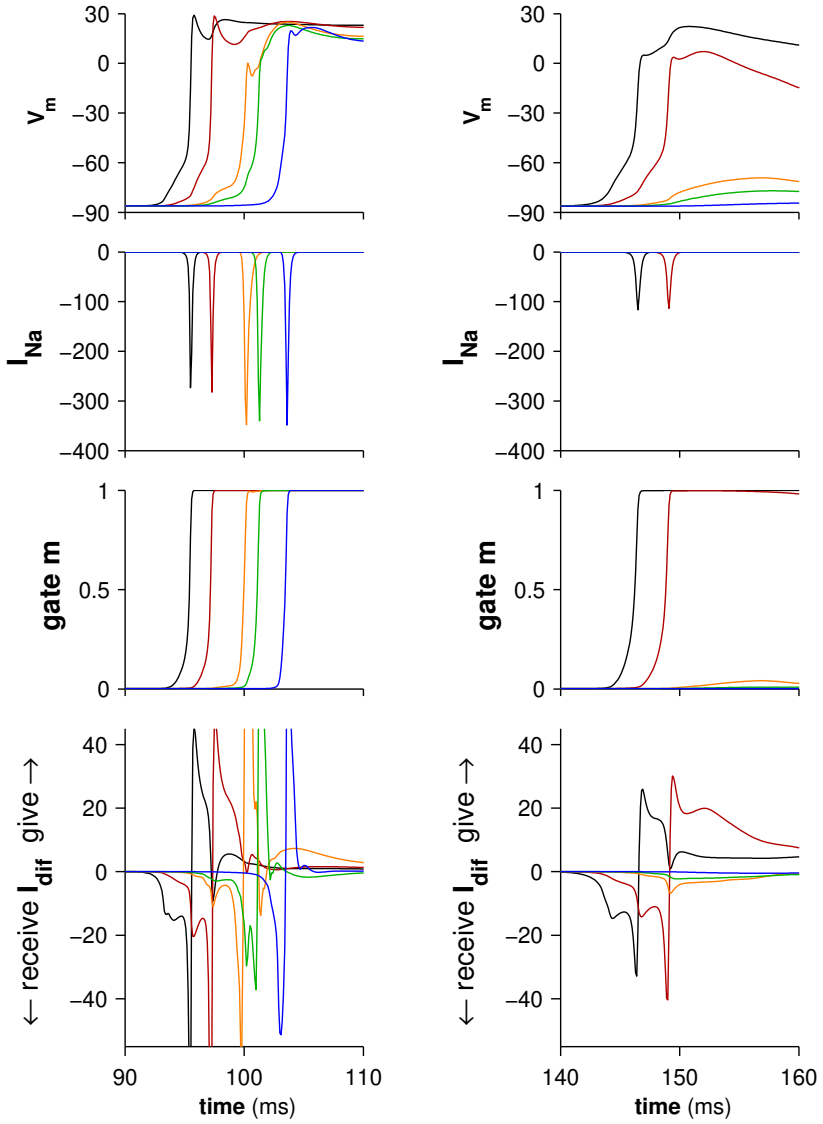

Figure 4.2: *Cellular electrophysical behaviour in and behind a gap in the barriers. Left with normal G_{Na}, right with reduced G_{Na}. The traces are colored from proximal to distal in black, red, orange, green and blue. From top to bottom the panels show the transmembrane potential, I_{Na}, activation gate of I_{Na}, and the current received or produced by a single model node. With reduced G_{Na}, many elements behind the structural discontinuities received too little current to reach the activation threshold. This resulted in excitation failure and activation delay of the right ventricular subepicardium and in ST-segment elevation followed by a negative T wave in the right precordial leads.*

excited elements. The amplitude of ST-segment elevation by excitation failure after reduction of the size of the gaps was limited by the increased resistance between the excited and unexcited myocardium (Figure 4.4).

4.4 Discussion

This study showed that in the heart of a patient diagnosed with Brugada syndrome and carrying a loss-of-function mutation in the SCN5A gene, activation block rather than premature repolarization or late depolarization was responsible for the Brugada sign in the ECG. Numerical simulations provided two key arguments that could not be obtained from experimental results. First, they showed that the phenomena could not be obtained without structural alterations. Second, they showed that in a model heart with tissue damage and with reduced G_{Na}, parts of the right ventricle did not depolarize, and kept drawing current for the whole duration of the ST elevation in the ECG. This persistent current resulted from a mismatch between the current source (a narrow strand of depolarized muscle) and the sink (a well-connected muscle volume of about 1 cubic millimeter), causing the activation to stop despite a current flowing between the depolarized and non-depolarized tissue.

A weakness of this simulation study was the coarse grain of the tissue damage, necessitated by the 200-µm size of the model elements. At the time, in 2010, more fine-grained simulations were not feasible. This is one of the motivations for the MICROCARD project (Section 6.5): we believe that the source-sink mismatches underlying the Brugada sign occur on a much smaller scale, where the individual links between muscle cells cannot be ignored.

Another limitation is the amplitude of the ST elevation produced by the model, which is considerably smaller than the well-known examples of the Brugada ECG. Perhaps this may be explained by the coarseness of the model as well, and in particular by the use of a homogenized model, in which conduction block occurs less readily than in discrete models. Investigating this hypothesis in a model representing individual myocytes would be very interesting. Further explanations may include exaggerations in the examples. Authors rarely report the filter settings they used to record an ECG, and even a nonstandard signal amplification is not always reported. Many clinicians prefer to use a higher than recommended cut-off for the high-pass filter that is used to suppress drift in the ECG. But even with a slightly higher setting, for example 0.1 Hz, the dominantly negative QRS complex often preceding a Brugada-type ST elevation can produce a positive "ringing" artefact, which exaggerates the ST elevation.

Notwithstanding its limitations, this study illustrates how a model can fill in a missing link in an argument built on experimental findings, and enhance our understanding of pathological mechanisms.

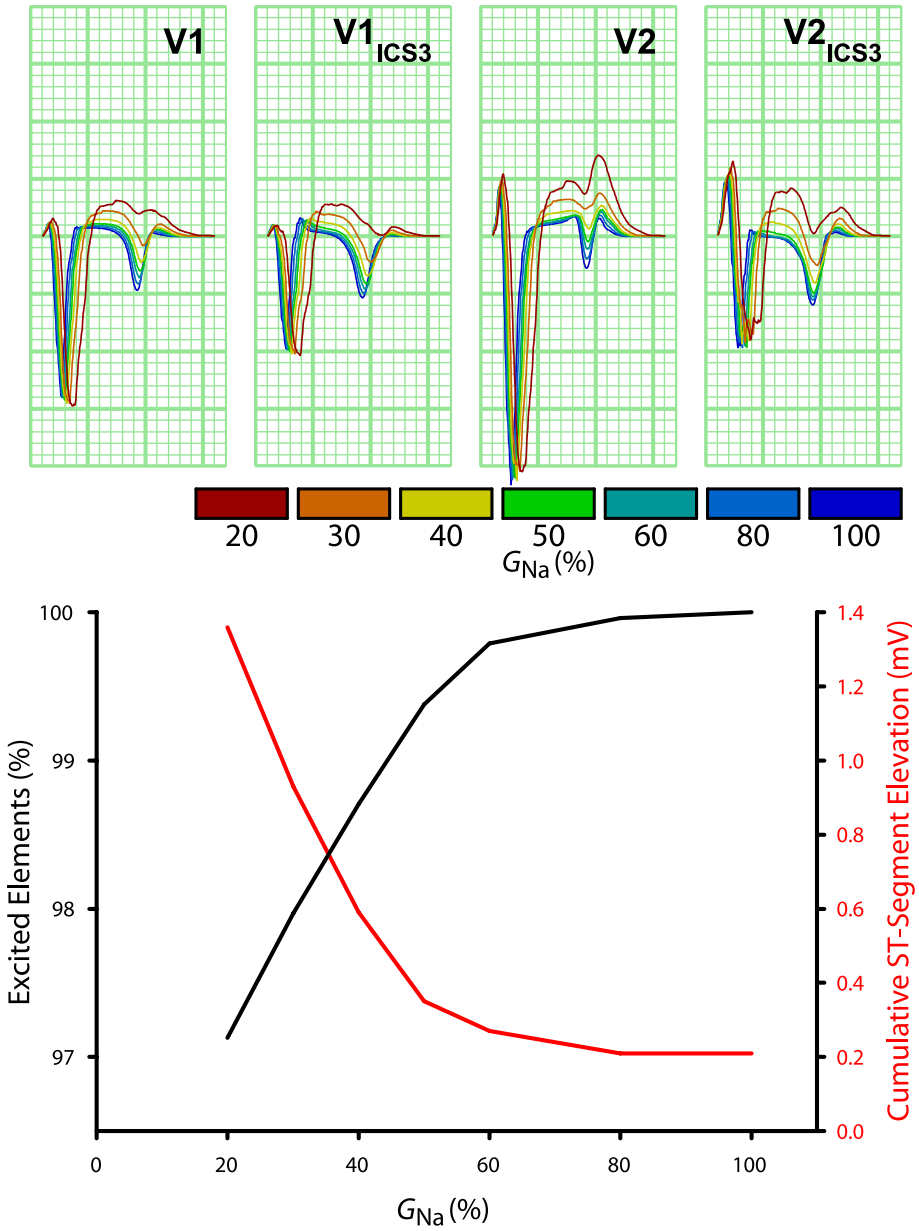

Figure 4.3: *Changes in simulated ECGs in structurally abnormal heart caused by reduction of G_{Na} and corresponding graph relating excited elements with ST-segment elevation in the right precordial leads. Reduction of G_{Na} below 50 % of normal resulted in a rapid reduction in excited elements and ST-segment elevation on the ECG.*

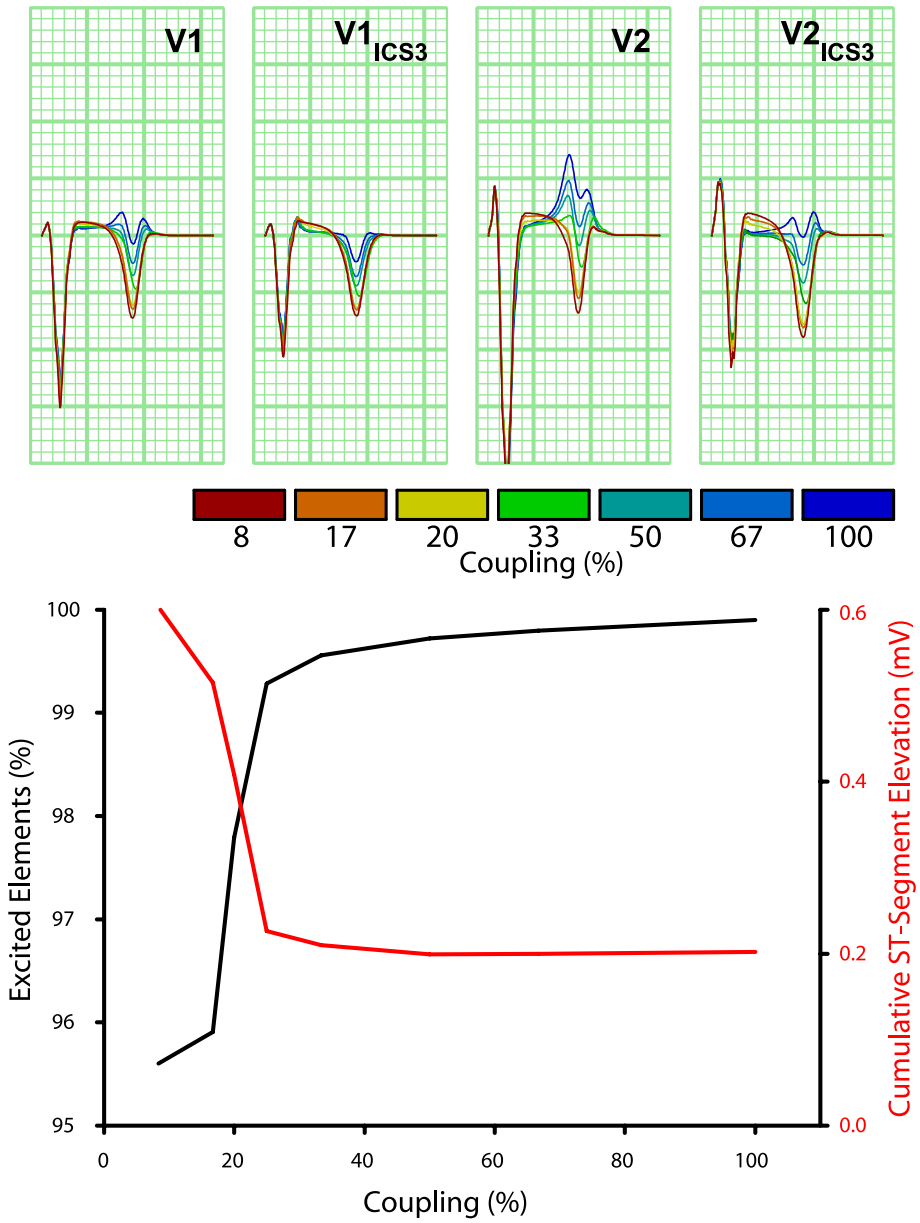

Figure 4.4: *Changes in simulated ECGs in structurally abnormal heart due to reduction in the simulated size of the gaps in the barriers by reduction of coupling in the gaps and corresponding graph relating excited elements with ST-segment elevation in the right precordial leads. Reduced coupling increased ST elevation but not as much as* G_{Na} *reduction did (Figure 4.3), because the resistance between the excited and unexcited elements limited the generated current.*

Chapter 5

The true shape of the P wave

Preface

The article that is reproduced here, in a slightly different form, concentrates on signal analysis. In the paper itself the numerical model has only a modest role, but the study would not have been performed if models had not persistently *failed* to produce the expected result. The problem was that, based on cardiology literature, we expected P waves (the ECG waves that represent the activation of the atria) to have a simple shape. The models, however, produced unruly multiphasic "P complexes." After having questioned the correctness of the model and numerous fruitless attempts to obtain the expected results, we began to question the correctness of our expectations, and decided to investigate the true shape of the P wave. It turned out that the model was right.

The original publication is Mark Potse, Theo A. R. Lankveld, Stef Zeemering, Pieter C. Dagnelie, Coen D. A. Stehouwer, Ronald M. Henry, André C. Linnenbank, Nico H. L. Kuijpers and Ulrich Schotten: P-wave complexity in normal subjects and computer models. *J. Electrocardiol.*, 49:545-553, 2016. doi:10.1016/j.jelectrocard.2016.05.005.

Summary

P waves reported in electrocardiology literature uniformly appear smooth, but computer simulation and signal analysis studies have shown much more complex shapes. To find the cause of this discrepancy, we investigated P-wave complexity in normal volunteers using high-fidelity electrocardiographic techniques without filtering. We recorded 5-minute multichannel ECGs in 16 healthy volunteers. Noise and interference were reduced by averaging over 300 beats per recording. In addition, normal P waves were simulated with a realistic model of the human atria.

Measured P waves had an average of 4.1 peaks (range 1–10) that were reproducible between recordings. Simulated P waves demonstrated similar complexity, which was related to structural discontinuities in the computer model of the atria. We conclude that the true shape of the P wave is very irregular and is best seen in ECGs averaged over many beats.

5.1 Introduction

On the routine electrocardiogram (ECG), P waves usually have a smooth appearance [225]. A notched or more complex P-wave shape is thought to be an abnormal finding. A previous study even found notched P waves to be a predictor of cardiovascular events [103]. Furthermore, changes in P-wave morphology are associated with interatrial block [17], a known predictor for supraventricular tachyarrhythmias [4, 95] and electromechanical dysfunction of the left atrium [76].

However, recent computer modeling studies have predicted highly complex P-wave shapes in normal atria [110, 142]. Details of these P waves were linked to normal structural features of the atria. More complex shapes have also been observed in advanced signal-analysis studies [102, 111, 149].

Prompted by these conflicting reports we tested if complex P-wave shapes are present in healthy subjects. We studied normal young and aged volunteers using 5-minute multichannel high-resolution surface ECGs. We avoided low-pass filters, because these may remove high-frequency signal content along with the noise, while being unable to remove interference with lower frequencies. Instead, noise suppression was achieved by a careful P-wave alignment and averaging procedure resulting in an ECG with microvolt-level fidelity. We compared the measured P waves with those predicted by a computer simulation study involving a structurally realistic anatomical model of the human atria.

5.2 Methods

Measurements

Multichannel ECGs from 184 thoracic electrodes [112] and 3 limb electrodes were recorded in two groups:

- A "young" group consisting of seven healthy volunteers (Y1–Y7), all male, aged 26–43 years (average 30); and
- a "senior" group consisting of seven male and two female subjects (S1–S9) aged 61–72 years (average 67) with normal cardiac anatomy and function who entered the Maastricht Study, a population-based cohort study on the development of chronic diseases [195]. The Maastricht Study has been approved by the ethical committee of Maastricht University Medical Center. All participants gave written informed consent. Subject S9 was diabetic.

Recordings were made using a 256-channel Biosemi ActiveTwo amplifier (Biosemi, Amsterdam, The Netherlands) with 0.8 µV root-mean-square noise level. Signals were low-pass filtered (3 dB point 419 Hz) and digitized at a frequency of 2048 Hz with 0.03 µV resolution.

Signals from electrodes with poor contact and intervals of recording with excessive artifacts were manually removed. QRS peaks were detected using an energy signal, similar to that used by Pan and Tompkins [144], based on the temporal derivatives of the 184 thoracic leads. A time instant for baseline correction was chosen manually shortly before the P-wave onset, and a piecewise linear baseline correction was

applied to the entire recording. The detected QRS peaks were used for an initial alignment of the beats. A P-wave template was chosen manually, and the remaining beats were shifted to maximize correlation of the P wave with the template. This procedure was performed on the sum squared voltages of the thoracic leads to reduce the effect of noise on the alignment. An average P wave was then computed and used as a template in a second alignment step. P waves that correlated less than a preset threshold of 0.9 with the template were excluded from this averaging. The final averaged PQRST complex was used for analysis. To avoid influence of mains interference on the alignment process, a notch filter at 50 Hz and multiples thereof was applied to the raw data. Only the signals used for beat detection and alignment were filtered; the final averaging took place on unfiltered data.

To quantify the complexity of the signals, we automatically counted the peaks (positive and negative) in each P wave. The algorithm first determined all local extrema, defined as samples that had either a higher value than the preceding and following sample, or a lower value than both. Then it identified all pairs of successive extrema with voltage values that were closer than a given threshold, and repeatedly removed the pair with the smallest absolute difference until no subthreshold differences remained.

We report the number of peaks determined with each of two methods to set the threshold for the definition of a peak: it was either fixed at 10 µV or determined by an estimate of the variability in the signal. This estimate was obtained by performing the alignment and averaging procedure described above on five randomly determined subsets of beats. The maximum difference between the five resulting averages and the global average signal was then used as the variability measure. Since the variability in the global average should be smaller than the variability in the group averages, this yields an overestimation of the variability, and therefore an underestimation of the number of peaks. This conservative estimate provides a lower bound on the number of peaks that are invariable, i.e. should be reproducible between repeated measurements in the same subject.

To find inter-subject similarities in the pattern of notching we considered the timing of the local extrema, in all 12 leads combined. Initially, peak and nadir times for all subjects combined were counted in 10-millisecond bins. Adjacent bins with similar counts were then combined and bin edges were adapted to identify intervals of high and low density. The number of extrema in each of the new bins was then determined for each subject individually, and a mean value and standard deviation for each bin were computed.

P-wave duration was difficult to measure because there was no instant in the P-Q interval where all signals were zero. Therefore we measured it manually using digital calipers in a signal prepared from the sum of the absolute values of all leads, after averaging. P-wave onset was defined as the start of the first clear upstroke of the signal, and P-wave end as a local minimum after which rapid signal changes ceased.

From the 184 thoracic electrodes we selected those that were closest to the standard precordial positions [112]. Together with he limb leads these were used to create a standard 12-lead ECG.

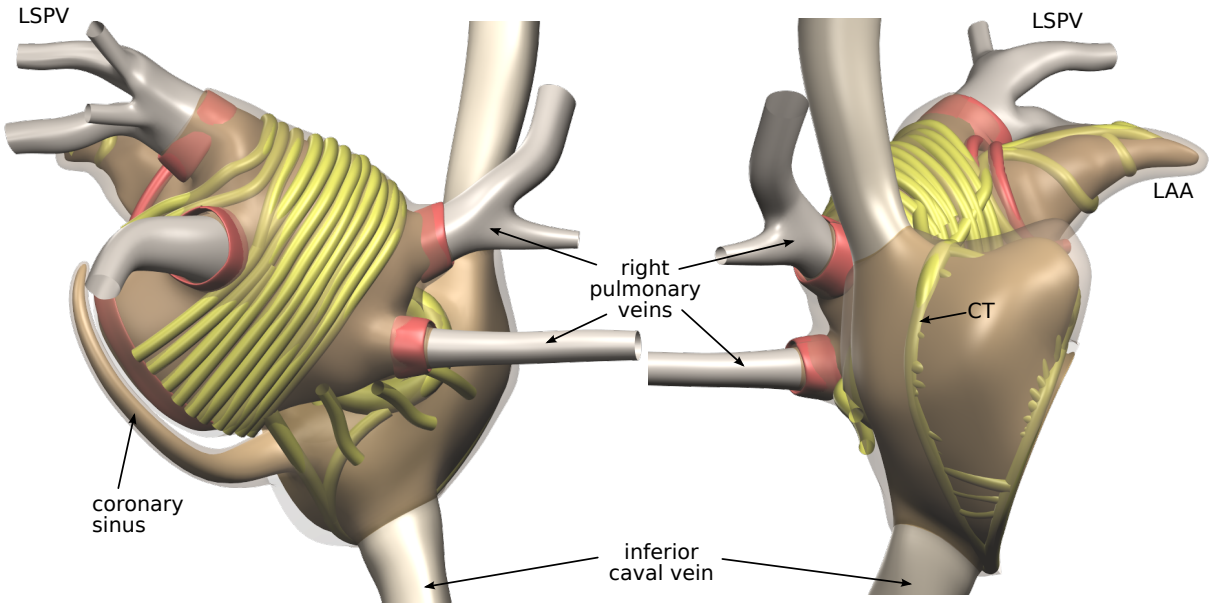

Figure 5.1: *Anatomic model of the atria used for the simulations. Left panel, posterior view; right panel, right sagittal view. The endocardial surface is rendered in brown; fiber bundles in yellow, "orientation bundles" in red, and the "myocardial envelope" semi-transparently. LSPV, left superior pulmonary vein; LAA, left atrial appendage; CT, crista terminalis.*

Simulations

An anatomical model of the human atria was built using Blender (The Blender Foundation, Amsterdam, The Netherlands) as a 3-D editing tool. The global shape was guided by MRI data from a subject with normal atrial anatomy. Details were filled in based on literature [5, 88, 89]. As illustrated in Figure 5.1, this model consisted of surfaces representing the endocardial surface of the atria, pulmonary and caval veins, and coronary sinus; an "envelope" for the atrial myocardium; and several bundles representing thicker parts of the atrial myocardium such as the crista terminalis, the pectinate muscles, and the superior and posterior wall of the left atrium. Also included were a smaller number of "orientation bundles" which defined local myofiber orientation.

The various surfaces were then filled with a hexahedral mesh at 0.2-mm resolution. Within the myocardial envelope, a 1-mm layer of myocardium was placed at the endocardial side. This myocardium was given isotropic electrical conductivity, except where it coincided with an orientation bundle (red in Figure 5.1); in these places it was made anisotropic with a fiber orientation aligning with the bundle's axis. Bundles (yellow in Figure 5.1) were filled with anisotropic myocardium with a fiber orientation aligning with the bundle direction.

Simulations of atrial electrical activation were performed using the Propag software (version 4) [168]. Atrial activation was simulated using a monodomain reaction-diffusion equation on a semi-structured mesh with a spatial step size of 0.2 mm. Membrane electrophysiology was represented by the Courtemanche model for the human atrial myocyte [53]. To compute the ECG from the simulated atrial activity we embedded the atrial model in an inhomogeneous torso model including lungs

and intracavitary blood masses and solved the bidomain equation at 1-mm resolution [169].

For comparison of measured and simulated P waves, the simulated ECGs were subjected to a low-pass filter with a cut-off frequency of 419 Hz, the same value as the analog filter applied to the measured data. In addition, the simulated P waves were subjected to the same alignment and averaging procedure as the measured data. For this purpose we created a record consisting of only noise and physiological variability by taking the original recording of one subject, subtracting from each of its 366 beats the P wave-aligned average PQRST complex, and superposing the simulated P wave and the subject's averaged QRST complex.

Frequency content

Amplitude spectral densities of measured and simulated 12-lead ECGs were estimated using a discrete Fourier transform. A Hann window was used to minimize frequency aliasing. To estimate the noise spectrum of the measured data the average signal was subtracted from each beat, and the average spectrum of the remaining data in the P-wave interval was computed. To estimate the noise after averaging, the beats were averaged in 5 randomly selected groups. The difference between each group average and the total average was computed and the average spectrum of these difference signals was determined. This spectrum may be expected to overestimate the final noise densities by a factor $\sqrt{5}$ [93, 197]. In addition the spectra of the average P wave, QRS complex, and T wave were computed. All spectral densities were averaged over the 12 standard leads.

Statistics

The statistical significance of differences in group mean values of the number of peaks was estimated using Student's t-test; $p < 0.05$ was considered significant.

5.3 Results

Measurements

The total noise level in the recordings was about 20 µV peak-to-peak. Signal averaging reduced the noise level to less than 2 µV. In Figure 5.2, panel A shows the raw data for one lead in one subject. Panel B shows the same signal after low-pass filtering with 150 and 40 Hz cut-off frequencies. With a 150-Hz cut-off, the recommended value [107], there is still noise remaining. With a 40-Hz cut-off, a value often used clinically [108], the signal is smooth, but it cannot be characterized as a simple dome or sine wave. Panel C of Figure 5.2 shows the signal after application of our averaging methods, using either alignment on the QRS complex or on the P wave. With P wave-based alignment more small-scale features could be resolved, while either type of alignment resolved the larger features of the P wave. The PQ segment became a single smooth curve, and the 40-ms interval before the P wave became flat, demonstrating that the remaining noise level was less than the thickness of the trace. The remaining features that are visible in the P-wave aligned signal can therefore be

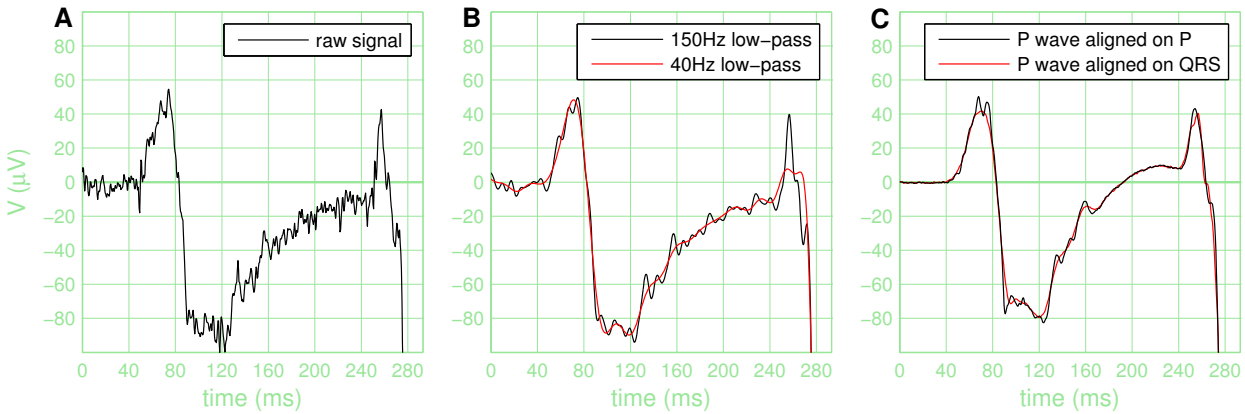

Figure 5.2: ***A****: Raw signal for lead V1, after baseline correction.* ***B****: The same signal, low-pass filtered at 150 Hz.* ***C****: Signal after averaging 300 beats. Red trace, alignment based on the QRS complex; black trace, alignment based on the P wave. In both panels, only the P wave, PQ interval, and the onset of the QRS complex (clipped) are shown. Horizontal grid lines are 20 µV apart (i.e. 5× normal amplification); vertical grid lines are 40 ms apart (standard). The display starts at the baseline point.*

assumed to be physiological. Comparison between panels B and C shows that 150-Hz filtering was not enough to remove all interference, and 40-Hz filtering deleted physiological signal features. Both types of filtering did not allow the finest details of the P wave to be seen.

An averaged 12-lead ECG of one of the subjects is shown in Figure 5.3. Due to the extremely low resulting noise level the P-wave shape and PQ interval are clearly defined. The QRS complexes are slightly smoothed due to the alignment on the P wave and the variability (approximately ±5 ms) in PQ interval.

Average P-wave duration was 104 ms (range 90–129) in the young group and 108 ms (range 87–130) in the senior group.

Figure 5.4 (panels A–E) shows only the P wave and the PQ interval, at a much larger magnification, for five subjects. Table 5.1 and Table 5.2 report the number of peaks. To determine the minimum number of invariable peaks that could be demonstrated in each lead, the threshold for the definition of a peak was determined by the variability in that lead in each subject. The results are reported in Table 5.1. The number of peaks differed between leads and between subjects; the average over all leads and all subjects was 4.1.

To compare the number of peaks between leads and between subjects the analysis was repeated with a fixed threshold of 10 µV. The results are reported in Table 5.2, and demonstrate once more large differences between leads and between subjects. No statistically significant differences between the two groups were found.

The analysis of temporal positions of peaks suggested three intervals in which peaks occurred more often than in neighboring intervals. We delineated the intervals of high density as 40–45, 60–75, and 85–100 ms after P-wave onset. In contrast, the first 40 ms of the P-wave had relatively few peaks. The density of peaks was evaluated in 7 temporal bins of varying widths, for each subject individually. Mean and standard

	I	II	III	aVL	aVR	aVF	V1	V2	V3	V4	V5	V6	average
subject Y1	1	1	3	1	4	1	4	2	2	2	2	2	2.1
subject Y2	1	2	5	1	2	2	8	4	8	3	2	3	3.4
subject Y3	3	5	5	5	1	5	3	1	1	1	3	5	3.2
subject Y4	1	5	4	3	1	5	4	4	4	4	3	7	3.8
subject Y5	4	2	5	3	3	3	2	4	5	7	3	5	3.8
subject Y6	1	3	3	3	5	3	2	3	3	3	3	3	2.9
subject Y7	4	5	8	4	6	5	3	3	4	4	4	4	4.5
average Y	2.9	3.4	4.7	3.1	3.7	3.9	4.3	3.9	4.3	3.9	3.1	4.6	3.8
subject S1	6	6	5	6	8	8	7	6	6	6	6	6	6.3
subject S2	3	5	3	5	3	2	4	3	3	3	5	3	3.5
subject S3	2	4	5	2	2	5	4	5	7	5	5	5	4.2
subject S4	3	5	3	3	3	5	5	5	3	3	6	10	4.5
subject S5	1	2	3	3	1	2	5	8	8	10	8	1	4.3
subject S6	3	3	1	3	3	1	1	1	4	4	2	2	2.3
subject S7	4	4	4	4	3	5	6	5	5	2	6	6	4.5
subject S8	4	3	7	3	6	6	4	6	5	5	4	5	4.8
subject S9	9	6	8	6	10	8	7	9	7	7	6	7	7.5
average S	3.3	4.1	4.3	3.7	3.9	4.3	4.3	4.7	5.0	4.7	5.1	4.7	4.3
average	3.1	3.8	4.5	3.4	3.8	4.1	4.3	4.3	4.7	4.3	4.2	4.6	4.1

Table 5.1: *Lower bounds on the number of stable peaks in each lead for each subject. Averages per lead and per subject are also given.*

	I	II	III	aVL	aVR	aVF	V1	V2	V3	V4	V5	V6	average
subject Y1	1	1	3	1	3	1	2	2	2	2	2	2	1.8
subject Y2	1	2	7	1	4	4	4	10	8	3	2	3	4.1
subject Y3	1	1	2	1	1	2	1	1	1	1	1	1	1.2
subject Y4	1	3	4	3	1	5	4	4	4	4	3	1	3.1
subject Y5	4	1	2	1	3	1	2	4	1	1	1	1	1.8
subject Y6	1	3	3	3	7	3	2	3	3	3	1	1	2.8
subject Y7	4	6	5	4	5	5	5	5	2	1	2	5	4.1
average Y	1.9	2.4	3.7	2.0	3.4	3.0	2.9	4.1	3.0	2.1	1.7	2.0	2.7
subject S1	3	1	1	1	1	2	2	1	3	3	1	1	1.7
subject S2	4	2	3	2	4	2	3	4	4	4	2	2	3.0
subject S3	3	3	1	3	3	2	2	2	3	3	3	3	2.6
subject S4	2	2	3	2	2	1	4	3	3	5	5	5	3.1
subject S5	3	3	3	3	3	2	3	2	3	3	4	4	3.0
subject S6	1	2	1	3	1	2	3	4	4	2	2	14	3.2
subject S7	2	3	1	2	3	1	1	1	2	2	2	2	1.8
subject S8	4	4	4	4	3	3	4	5	5	3	2	2	3.6
subject S9	2	3	7	1	4	6	2	6	7	5	4	5	4.3
average S	2.7	2.6	2.7	2.3	2.7	2.3	2.7	3.1	3.8	3.3	2.8	4.2	2.9
average	2.3	2.5	3.1	2.2	3.0	2.6	2.8	3.6	3.4	2.8	2.3	3.2	2.8
p	0.23	0.87	0.29	0.58	0.41	0.43	0.77	0.42	0.47	0.06	0.06	0.14	0.65

Table 5.2: *Number of peaks in each lead for each subject, determined using a fixed threshold of 10 μV. Averages per lead and per subject are also given.*

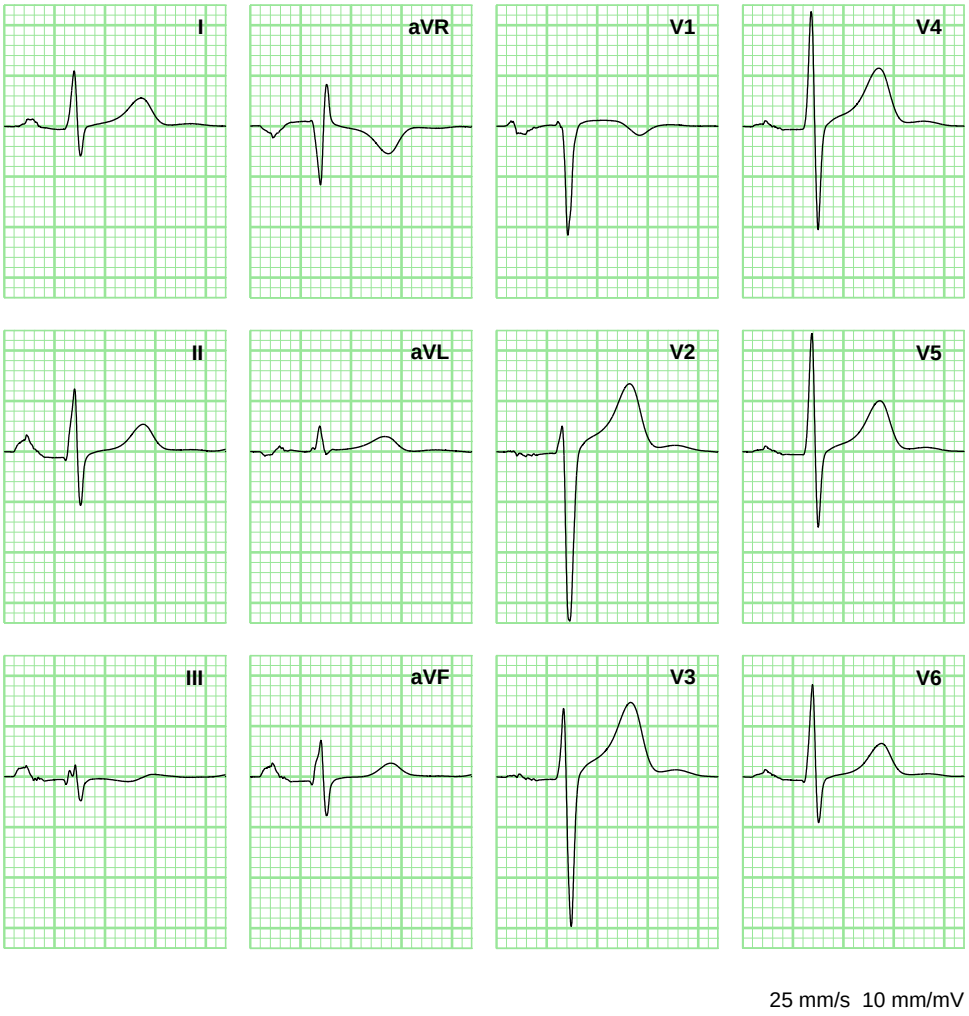

Figure 5.3: *12-lead* ECG *of subject Y2, averaged over 300 beats using alignment on the P wave. Horizontal grid lines are 0.1 mV apart, vertical grid lines 40 ms (both standard).*

deviation for the whole group are reported in Figure 5.5. Five differences between adjacent bins were found to be statistically significant, establishing the intervals 60–75 ms and 85–100 ms after P-wave onset as having a relatively high density of peaks.

Simulations

Simulated P waves are shown in panel F of Figure 5.4. The signals show slightly more complexity than the measured signals, but similar amplitude and variability in shape.

The effect of different filter setting is illustrated in Figure 5.6 using low-pass filter frequencies of 419 Hz, 150 Hz, and 40 Hz. A low-pass frequency of 150 Hz can be seen to affect the smaller features of the P wave, for example the appearance of the first extremum in lead III. Such a filter does not affect the global shape of the P wave, including the number of peaks. At a low-pass frequency of 40 Hz, however, many

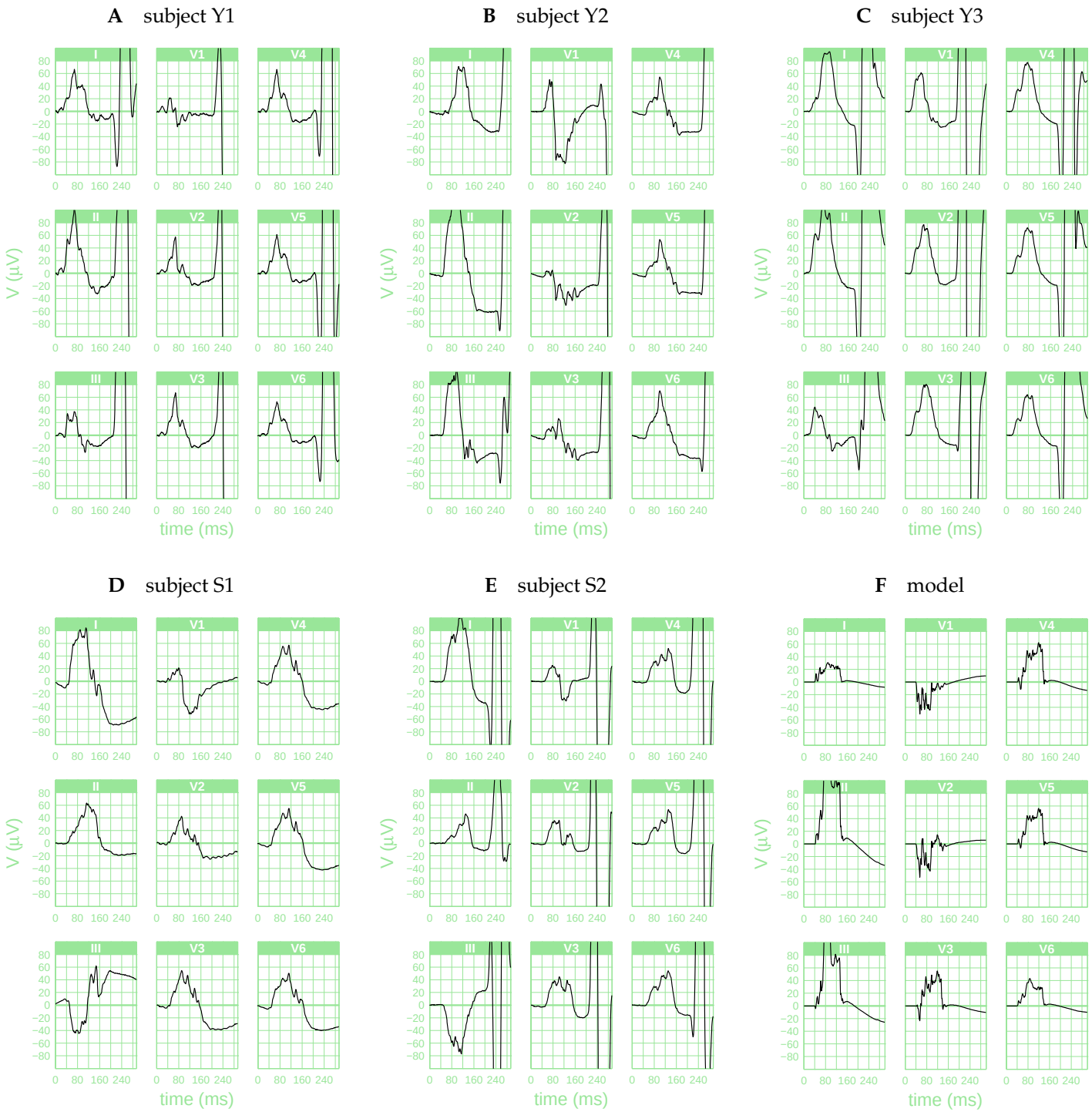

Figure 5.4: *Selected* ECG *leads of 5 subjects and the computer model, showing only the P wave, PQ interval, and the onset of the QRS complex (clipped). Signals were averaged over 300 beats using alignment on the P wave. Horizontal grid lines are 20 μV apart (i.e. 5× normal amplification); vertical grid lines are 40 ms apart (standard). The display starts at the baseline point and the zero level is shown with a thicker grid line.*

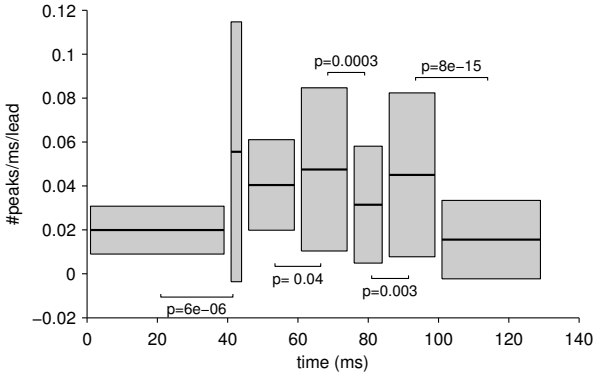

Figure 5.5: *Mean and standard deviation of the number of peaks per millisecond time and per lead. For each bin, a thick horizontal line indicates the mean, and the gray box ±1 standard deviation. Bin edges were located at 0, 40, 45, 60, 75, 85, 100, and 130 ms after P-wave onset. The p values for the difference between the means of adjacent bins are indicated if they classify as statistically significant ($p < 0.05$).*

details were lost. The notch in lead III disappeared, and in several places two closely separated peaks merged into one.

When the simulated P wave was superposed on the noise record of subject Y2 and subjected to the same alignment and averaging procedure as the measured data, the recovered 12-lead P wave differed from the original by less than 4 µV (0.46 µV root-mean-square). The traces were visually indistinguishable from those in Figure 5.4, panel F.

Frequency content

The spectral densities of subject Y2 are shown in Figure 5.7. At a frequency of approximately 60 Hz the P-wave amplitude density drops below the original noise level. Around 200 Hz it reaches the final noise level, but at that frequency it is already 2 orders of magnitude smaller than at 10 Hz, so that it has little influence on the total signal. The P-wave signal content below 40 Hz was 83 %. An additional 14 % was contained in the band 40–150 Hz, and 3 % in still higher frequencies.

5.4 Discussion

We have shown that both measured and simulated P waves in subjects with normal atria have a complex shape. P waves had 4.1 distinct peaks on average, while up to 10 peaks could be identified in some cases. Peaks were relatively rare in the first 40 ms of the P wave, and relatively common in the intervals 60–75 and 85–100 ms after P-wave onset.

Contemporary textbooks show the P wave as a half circle or, in the biphasic case, as a sine wave [122, 225]. Incidental reports on nonfiltered averaged P waves have demonstrated complexity similar to our results [102, 111, 149], but this knowledge is not reflected in the recent medical literature. Not only textbooks, but also original reports show very smooth P waves [82, 155]. Using more recent technology and an

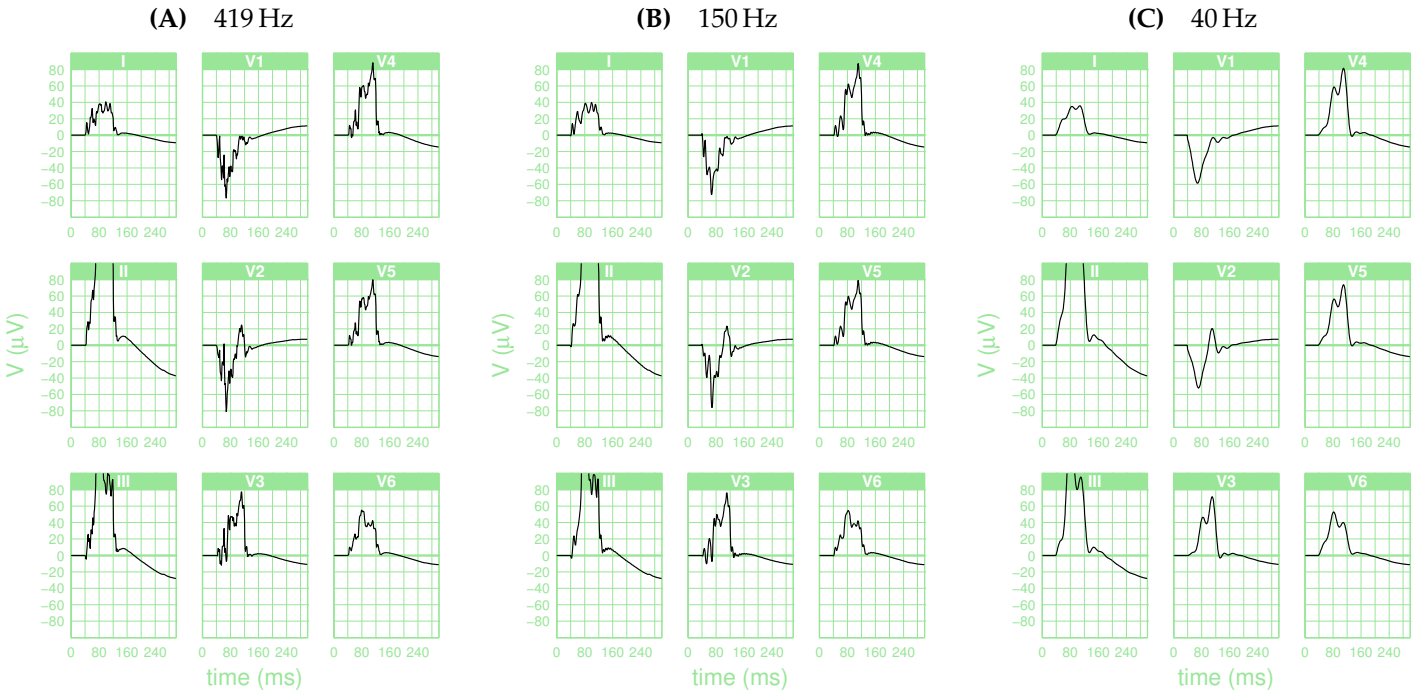

Figure 5.6: *Simulated P waves low-pass filtered at (**A**) 419 Hz (same as measured signals); (**B**) 150 Hz (guidelines); and (**C**) 40 Hz.*

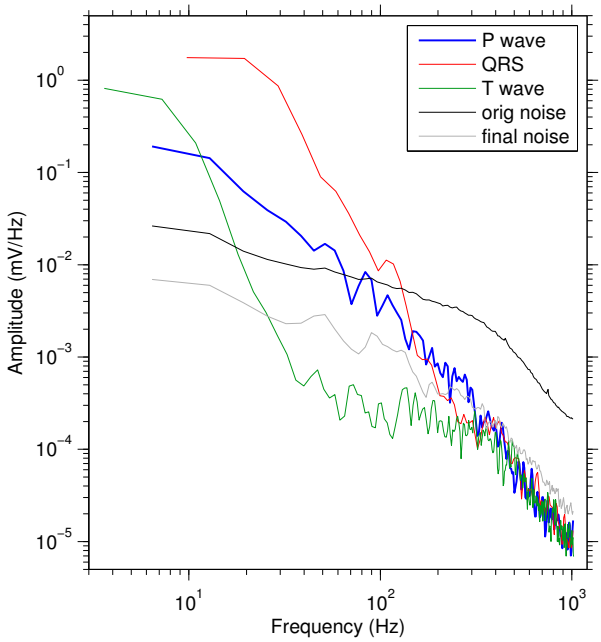

Figure 5.7: *Amplitude spectral density of the original and averaged record of subject Y2. The lowest measured frequency depended on the length of the associated interval. In blue, red, and green, the spectra of the averaged P wave, QRS complex, and T wave are shown. The spectrum of the original recording noise (black) was averaged over all beats and is therefore smoother than the other spectra. The final noise spectrum (gray) was computed from 5 group averages and therefore overestimates the noise after averaging all beats.*

approach targeted at precise alignment of P waves, we have confirmed the complex shapes shown in the older reports. In addition, our study is the first to systematically investigate the detailed shape of the P wave in the 12-lead ECG.

The smooth P-wave shapes shown in recent literature may be explained by low-pass filtering and perhaps inaccurate alignment of the P waves in averaging procedures. In patients with variable P-wave shapes, it may be very challenging to obtain good alignment, since the waves should at the same time be divided into clusters representing different physiological signals [101]. Even in our normal subjects, comparison of raw and averaged signals occasionally suggested that details had been smoothed out by averaging. In clinical practice, the small size at which P waves are typically printed, the thickness of the trace, and the aspect ratio which is more suitable for QRST complexes further contribute to an underestimation of P-wave complexity. However, the current generation of ECG systems stores the data digitally and essentially unfiltered, allowing the viewer to select the filter characteristics. Some systems also allow the user to zoom in or change the amplification. These advances will allow clinicians to see more details of the P wave.

Noise and interference generated at the electrode-skin interface, in the wiring, and in the amplifier is inevitable in ECG recordings. Low-pass filtering is a common method to reduce this noise at least for high frequencies, but it also removes the high-frequency part of the signal. Selection of the cut-off frequency is therefore important. Guidelines recommend a frequency of at least 100 Hz [152] and preferably 150 Hz [107]. However, according to one report 53 % of routine ECGs were observed with a low-pass filter frequency of 40 Hz, and another 17 % at filter frequencies ranging from 30 to 35 Hz [108]. As shown in Figure 5.2 and Figure 5.6, the true shape of the P wave cannot be observed using such filter settings. Our spectral analysis showed that 17 % of the P-wave signal is contained in frequencies above 40 Hz, and 3 % above 150 Hz. Yet, filtering at 150 Hz would not suffice to recover 97 % of the true P-wave shape, because there is significant noise content below that frequency (Figure 5.2 and Figure 5.7). In contrast to filtering, averaging can remove noise in the same frequency band as the signal without removing the signal itself.

The methods that we used to obtain detailed P-wave shapes included several non-standard components: 1) recording techniques with very low interference; 2) a large number of channels allowing us to suppress noise in the alignment signal by spatial averaging; 3) long recordings (5 or 10 minutes) to allow averaging; and 4) alignment by maximizing correlation between P waves. Averaging with P-wave alignment was previously used by Havmoller at al. [82] and by subsequent studies from the same group [94, 101]. Nevertheless, the P waves they have shown were much smoother than ours. This may be due to their use of a 50 Hz mains filter, higher initial noise levels, or P-wave variability in their patient group.

Although the number of peaks was the same in simulated as in measured P waves, the simulated waves had a more complex shape related to deeper troughs between the peaks. This may be due to the crude representation of anatomical features in our model. In the real atria, transitions from thick bundles to thinner myocardium are probably much smoother than in the model. An alternative explanation is that our averaging methods still result in some smoothing of signals, for example due to slight variations in P-wave shape, and that in fact the physiological P wave is even more complex than we could measure. Using a simulated P wave superposed on

a realistic noise record of 366 beats we verified that our alignment and averaging method did not perceptibly distort the shape of a simulated P wave.

Another striking difference between the model and the measured results are the large PQ offsets in the measured leads, which were also highly variable between subjects. We assume that these offsets are part of the atrial repolarization waves, the remainder of which is masked by the QRS complex. In the model, these waves occurred later and had smaller amplitude. Nonzero potentials in the PQ interval can also be caused by propagation in the AV node and bundle of His. However, we think that this cannot fully explain the observed PQ offsets. His-bundle potentials have an ascending slope over a duration of about 40 ms and an amplitude of approximately 10 µV [149]. In contrast, we observed PQ segments with amplitudes that were several times larger and nearly flat. Moreover, the observed offsets were negative in lead II, where a positive His-bundle potential would be expected.

Limitations

The method described here required a large number of electrodes and some manual intervention. Clinical applicability could be improved by further automation and tests with a smaller number of electrodes. Our method to determine P-wave duration was somewhat subjective.

Acknowledgements

This study was supported by the 7th Framework Program of the European Union through a Marie Curie International Reintegration grant (number 256493) to M.P. and through the Collaborative project EUTRAF (number 261057).

A.C.L. was supported by the Dutch Technology Foundation STW under grant number 10959.

Simulations were performed on an SGI Altix 4700 supercomputer at Université de Montréal, operated by Calcul Québec and Compute Canada, and financed by the Canada Foundation for Innovation, NanoQuébec, RMGA, and the Fonds de recherche du Québec - Nature et technologies.

Chapter 6

Personal contributions

6.1 Contributions to cardiac signal analysis

My PhD project at the department of Medical Physics of the University of Amsterdam concerned the interpretation of electrocardiographic body surface maps: electrocardiograms (ECGs) measured with many electrodes (sixty-four in our case) spread over the chest and back. Using an idea that I developed as a Master student, we were to develop a tool that could estimate the exit sites of cardiac arrhythmia and pacing sites, while the patient was being treated in the catheterization laboratory. This tool was meant to help the cardiologist to rapidly bring a catheter to the site of origin, which could then be ablated with radiofrequency energy. It would have to interpret the ECGs automatically and present the predicted location on the X-ray screens that were used to monitor catheter positions at the time.

Due to personal circumstances of our clinical partners we could not develop or test clinical prototypes, but we did publish evaluations of our methods based on existing data [159, 174]. I further developed new analysis software for ECG and intracardiac data to support the work of the neighbouring Experimental Cardiology department [173]. This software has been used for dozens of studies since then. I also published a study on the problematic interpretation of endocardial electrograms measured with a 64-electrode "basket" catheter in the left ventricle [176] and contributed analysis and visualization methods to several clinical and experimental studies [90, 146, 147, 215, 218].

My original project on arrhythmia localization remains relevant today. Due to my involvement in the IHU Liryc and the numerous patients treated there with catheter ablation, it has been possible to revive this work with the much better data and computer hardware available today. We have initially used synthetic data produced by my own computer models to test new and existing methods [8–10, 104]. A roll-out in the clinic has again been difficult, this time due to the covid-19 pandemic and the impossibility of real-time data access.

Another signal-analysis study, published in 2016 [172], was discussed in Chapter 5. Finally, I have recently worked with the University of Zaragoza to infer blood electrolyte concentrations from the ECG in kidney patients, using both signal analysis and simulation [32–34].

6.2 Contributions to cardiac modeling

My interest in numerical modeling of the heart was evoked by a project in which we searched for possible ECG differences between two patient groups, hidden in large normal inter-subject variability. I became convinced of the necessity to first evaluate the expected ECG changes using a numerical model, and test for their presence, rather than taking a "data mining" approach, which would have required a much larger sample than possible with the rare syndrome we studied. I applied for a post-doctoral position with Dr. Ramesh Gulrajani, an ECG modeling pioneer and author of an acclaimed textbook on bioelectromagnetism [78]. This work resulted in the first bidomain reaction-diffusion model of the complete human ventricles [168]. This paper included several methodological innovations and has been cited over 500 times.

I have developed a variety of software to meet the demands of my own applied research. This includes construction of geometrical models, data compression methods, data analysis, and visualization. Much of this software is now maintained on Inria's Gitlab platform. This software is particularly suited for the simulation of cardiac activation and ECGs using realistic models of the human heart and torso (Figure 1.3).

I have published three studies specifically on the simulation of ECGs [151, 161, 169]. The first of these, published in 2009, has now been cited over 100 times.

The modeling software that I developed in Montreal has been gradually improved since then. In 2010 and 2011 it has been thoroughly revised to replace the original OpenMP parallelization by a hybrid MPI-OpenMP parallellization so that the software could run on the largest cluster machines that are currently available [109].

In recent papers I have shown that the current software is able to solve bidomain problems (Equation 1.5) on models with over 3 billion nodes [161] and monodomain problems on models with 11 billion nodes [175].

In the context of the MICROCARD project (2021–2024) I have devoted myself to the creation of software that produces virtual cardiac tissue: volumetric meshes representing individual cardiomyocytes with (somewhat) realistic shapes that can be used for the large-scale simulations at which the project aims [36, 162]. A small example is shown in Figure 6.1. To make the creation of such meshes possible, the MICROCARD project made considerable improvements in the Mmg remeshing software.

6.3 Contributions to understanding of cardiac disease

Although I did significant work on the methods for cardiac modeling, my aim has always been to use the software that I developed in order to better understand the (patho)physiology of the heart and its representation in measurable signals such as the ECG.

Nudged by the funding priorities in Canada and the expertise of the researchers around me, I have done several studies related to myocardial ischemia, the electrochemical effects of blocked coronary arteries [160, 163–165].

Following a move to Maastricht University in the Netherlands I have worked on atrial fibrillation [69–74] and heart failure combined with left-ventricular conduction disturbances. The study of heart failure has been my main topic of research

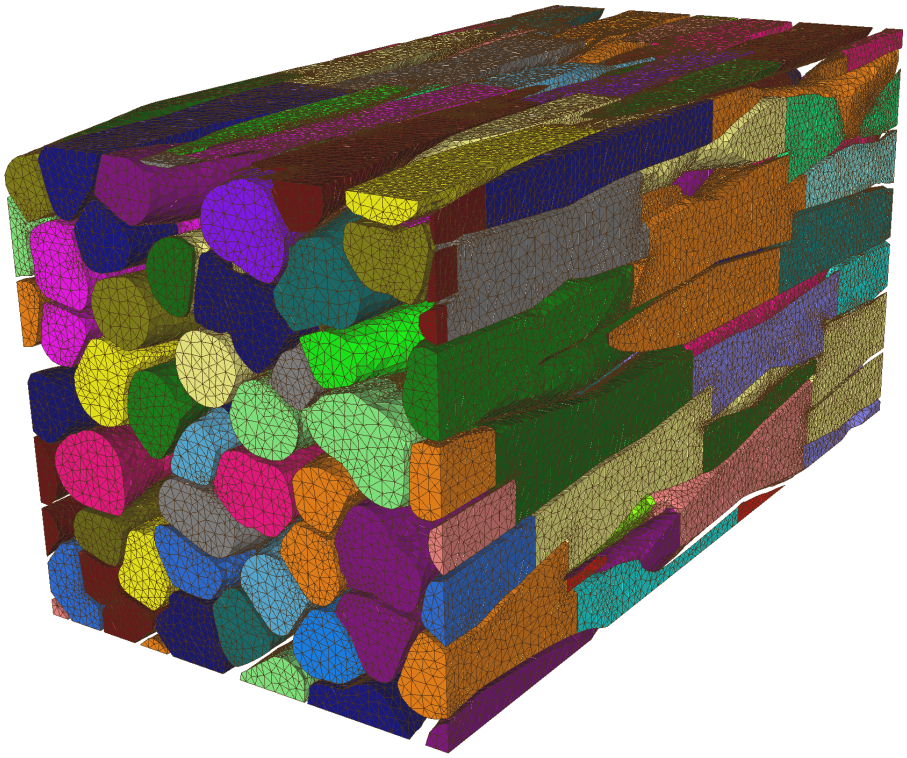

Figure 6.1: *Synthetic cardiac tissue model. Only surfaces are shown but the underlying mesh is volumetric. The dimensions of this tissue block are 400 × 200 × 200 µm. Colors distinguish individual cells, although some colors are used more than once.*

during 5 years spent half-time at the Università della Svizzera italiana in Lugano, Switzerland [13, 139, 170, 171, 191].

However, the subject that interests me most has has always been sudden-cardiac-death syndromes. Patients who have died or nearly died from such events have been divided into various syndromes, based on ECG abnormalities that they had in common. Several of these syndromes have been hypothesized to be caused by genetic abnormalities of specific ion channels in the heart. In collaboration with experimental and clinical researchers I have used modeling studies to challenge this hypothesis [96–98, 126] (Chapter 4). The view that I have helped to defend is that in most of these arrhythmia subtle abnormalities in the tissue structure are crucial, and that abnormalities in the ionic currents (genetically or pharmacologically induced) play a modulating role.

6.4 An interdisciplinary approach

In my work, cardiac modeling and signal analysis have interacted in several ways. My decision to become involved in cardiac modeling has been inspired by my work on signal analysis. Conversely, my modeling work on electrocardiographic P waves has led to a hypothesis that we have subsequently tested using a signal-analysis study (Chapter 5). During my stay in Bordeaux, we have also used the highly realistic signals produced by my models in order to test electrocardiographic inverse

methods [18, 29, 56, 58, 104, 105, 128, 180, 181, 204, 236], using a more reliable "ground truth" than measured data could provide. Similarly, I have used simulated signals in an influential study explaining cardiologists how to recognize repolarization phenomena in electrical signals measured in the heart (Chapter 3).

The insights in the physics behind cardiac electric phenomena that I have obtained due to my simulation work have also allowed me to contribute to studies where neither modeling nor signal analysis was involved [1, 2, 50, 80, 81, 121]

Most of my work results from a collaboration with scientists from other disciplines: cardiologists, radiologists, physiologists, biologists, biomedical engineers, numerical scientists, mathematicians, and recently also computer scientists. I think that this interdisciplinary approach, combined with an eclectic use of modeling, image analysis, and signal-analysis methods, allows an original line of research with a high societal and scientific impact, and many opportunities for junior scientists to become involved in interdisciplinary research.

6.5 Current work

As of 2024, my main occupations are the coordination of the EuroHPC MICROCARD projects.

The first MICROCARD project was the result of a succesful proposal submitted in January 2022 to EuroHPC, a joint undertaking of the European Union, several national funding agencies, and the European high-perfomance computing (HPC) industry. With a score of 14/15, the MICROCARD proposal likely won this competition as a rare medical application of computing machinery that is traditionally the exclusive domain of the physical and engineering sciences. The project, which started in April 2021, aims to build software that can simulate cardiac tissue on models with micrometer resolution, using future exascale supercomputers (machines that can perform 10^{18} mathematical operations per second). With this resolution, it will be possible to represent the cardiac muscle cells individually, together with their interconnections. I believe that such models are crucial to understand arrhythmia formation in cardiomyopathies, and to learn how arrhythmic risk relates to ECG features.

The MICROCARD project is also groundbreaking in terms of interdisciplinarity. Cardiac electrophysiology is traditionally the realm of biomedical engineers and applied mathematicians. Involvement of experts in numerical methods is rare, and experts in low-level code optimization are completely absent. Recent work in the project has shown that these informaticians are able to achieve over ten-fold speedups in parts of the code, using advanced compiler techniques. This "professionalization" of our simulation code could affect the whole field of electrophysiological simulation, not only in the heart but also in the nervous system and in other electrically active organs.

In addition to the overall coordination, I am leading the development of artificial tissue models in the MICROCARD project [162]. These models will be needed, at least temporarily, because models based on imaging data are currently limited to only a handfull of cells.

In May 2024 we learned that a followup proposal, MICROCARD-2, will be funded. The 30-month project allows to benefit from what we learned in the MICROCARD

project and deploy our software on the exascale supercomputers for which it was meant, and which are just beginning to arrive in Europe.

6.6 Future perspectives

The MICROCARD projects are, due to the funding source, concentrated on the development of computational methods and tools. However, the soon to be realized possibility of running simulations on micrometer-resolution models of cardiac tissue has also exposed the fact that such models currently do not exist. Three-dimensional imaging can reveal the shape of the cells with enormous precision, and can accurately localize proteins associated with ion channels and gap junctions, but is limited to a few dozen cells, most of which will be incompletely captured. Larger samples may become available within years from now, but their size will remain very much smaller than a whole heart. Therefore I believe that a large effort is needed to "grow" artificial tissue models, by hypothesizing rules that govern the structure, building models according to these rules, and confronting these models with imaging data. This will involve a massive involvement of experts in cardiac imaging, in the development of tissue models, and in the construction and improvement of computational meshes. The structural rules may even be inspired by the way in which cardiac tissue develops, implying a collaboration with embryologists. Such work would not only result in geometrical models of the tissue suitable for simulation, but also to insight in the rules that govern the structure, and in how these may change in diseased tissue.

My other plans are to propose new projects concerning patient-tailored simulation of ECG features in patients with characteristics of Brugada syndrome or the early repolarization variant, and new work on the analysis of P-wave details.

Finally, I am convinced that current understanding of the T wave and U wave in the ECG is incomplete at best. It is presently not possible to reconcile findings in isolated cells with those in the normal ECG. Much more work is needed to understand how the behaviour of the cells may change when they are isolated, or when the heart is decoupled from the autonomic nervous system.

References

[1] Saer Abu-Alrub, Marc Strik, Peter Huntjens, F. Daniel Ramirez, Mark Potse, Hubert Cochet, Hugo Marchand, Samuel Buliard, Romain Eschalier, Michel Haïssaguerre, Pierre Bordachar, and Sylvain Ploux. Left axis deviation in patients with nonischemic heart failure and left bundle branch block is a purely electrical phenomenon. *Heart Rhythm*, 18:1352–1360, 2021.

[2] Jorge Corral Acero, Francesca Margara, Maciej Marciniak, Cristobal Rodero, Filip Loncaric, Jingjing Feng, Andrew Gilbert, Joao F. Fernandes, Hassaan A. Bukhari, Ali Wajdan, Manuel Villegas Martinez, Mariana Sousa Santos, Mehrdad Shamohammdi, Hongxing Luo, Philip Westphal, Paul Leeson, Paolo DiAchille, Viatcheslav Gurev, Manuel Mayr, Liesbet Geris, Pras Pathmanathan, Tina Morrison, Richard Cornelussen, Frits Prinzen, Tammo Delhaas, Ada Doltra, Marta Sitges, Edward J. Vigmond, Ernesto Zacur, Vicente Grau, Blanca Rodriguez, Espen W. Remme, Steven Niederer, Peter Mortier, Kristin McLeod, Mark Potse, Esther Pueyo, Alfonso Bueno-Orovio, and Pablo Lamata. The "digital twin" to enable the vision of precision cardiology. *Eur. Heart J.*, 41:4556–4564, 2020.

[3] A. Selcuk Adabag, Russell V. Luepker, Véronique L. Roger, and Bernard J. Gersh. Sudden cardiac death: epidemiology and risk factors. *Nat. Rev. Cardiol.*, 7:216–225, 2010.

[4] Yogesh K. Agarwal, Wilbert S. Aronow, James A. Levy, and David H. Spodick. Association of interatrial block with development of atrial fibrillation. *Am. J. Cardiol.*, 91:882, 2003.

[5] Robert H. Anderson and Anton E. Becker. *Cardiac Anatomy: An Integrated Text and Colour Atlas*. Gower Medical Publishing, London, 1980.

[6] Charles Antzelevitch, Pedro Brugada, Martin Borggrefe, Josep Brugada, Ramon Brugada, Domenico Corrado, Ihor Gussak, Herve LeMarec, Koonlawee Nademanee, Andres Ricardo Perez Riera, Wataru Shimizu, Eric Schulze-Bahr, Hanno Tan, and Arthur Wilde. Brugada syndrome; report of the second consensus conference. *Heart Rhythm*, 2(4):429–440, 2005.

[7] Andony Arrieula. *Méthodes numériques d'apprentissage pour faciliter la localisation des arythmies ventriculaires lors d'une procédure d'ablation*. PhD thesis, Université de Bordeaux, October 2022.

[8] Andony Arrieula, Hubert Cochet, Pierre Jaïs, Michel Haïssaguerre, and Mark Potse. In-silico evaluation of an iterative pace-mapping technique to guide catheter ablation of ventricular ectopy. In *Computing in Cardiology*, volume 46, Singapore, 2019. Computing in Cardiology.

[9] Andony Arrieula, Hubert Cochet, Pierre Jaïs, Michel Haïssaguerre, and Mark Potse. An improved iterative pace-mapping algorithm to detect the origin of premature ventricular contractions. In *Computing in Cardiology*, volume 47, page 62, Rimini, 2020. Computing in Cardiology.

[10] Andony Arrieula, Hubert Cochet, Pierre Jaïs, Michel Haïssaguerre, Nejib Zemzemi, and Mark Potse. In-silico data based machine learning technique predicts premature ventricular contraction origin coordinates. In *Computing in Cardiology*, volume 48. Computing in Cardiology, 2021.

[11] Takashi Ashihara and Natalia A. Trayanova. Asymmetry in membrane responses to electric shocks: Insights from bidomain simulations. *Biophys. J.*, 87:2271–2282, 2004.

[12] Travis M. Austin, Mark L. Trew, and Andrew J. Pullan. Solving the cardiac bidomain equations for discontinuous conductivities. *IEEE Trans. Biomed. Eng.*, 53(7):1265–1272, 2006.

[13] Ljuba Bacharova, Anton Mateasik, Rolf Krause, Frits W. Prinzen, Angelo Auricchio, and Mark Potse. The effect of reduced intercellular coupling on electrocardiographic signs of left ventricular hypertrophy. *J. Electrocardiol.*, 44:571–576, 2011.

[14] Roger C. Barr and Robert Plonsey. Propagation of excitation in idealized anisotropic two-dimensional tissue. *Biophys. J.*, 45:1191–1202, 1984.

[15] Roger C. Barr, Maynard Ramsey, III, and Madison S. Spach. Relating epicardial to body surface potential distributions by means of transfer coefficients based on geometry measurements. *IEEE Trans. Biomed. Eng.*, 24(1):1–11, 1977.

[16] Antoni Bayés de Luna, Velislav N. Batchvarov, and Marek Malik. The morphology of the electrocardiogram. In A. John Camm, Thomas F. Lüscher, and Patrick W. Serruys, editors, *The ESC Textbook of Cardiovascular Medicine*. Blackwell Publishing, 2006.

[17] Antonio Bayés de Luna, Pyotr G. Platonov, Francisco G. Cosio, Iwona Cygankiewicz, Carlos Pastore, Rafa Baranowski, Antoni Bayés-Genis, Josep Guindo, Xavier Viñolas, Javier Garcia-Niebla, Raimundo Barbosa, Shlomo Stern, and David Spodick. Interatrial blocks. A separate entity from left atrial enlargement: a consensus report. *J. Electrocardiol.*, 45:445–451, 2012.

[18] Laura Bear, Peter Huntjens, Mark Potse, Josselin Duchateau, Sylvain Ploux, and Remi Dubois. A novel method for deriving the 12-lead ECG from body surface potential maps. In Christine Pickett, Cristiana Corsi, Pablo Laguna, and Rob MacLeod, editors, *Computing in Cardiology*, volume 44, Rennes, France, 2017.

[19] G. W. Beeler and H. Reuter. Reconstruction of the action potential of ventricular myocardial fibres. *J. Physiol.*, 268:177–210, 1977.

[20] Mirza Faisal Beg, Patrick A. Helm, Elliot McVeigh, Michael I. Miller, and Raimond L. Winslow. Computational cardiac anatomy using MRI. *Magn. Res. Med.*, 52:1167–1174, 2004.

[21] Omer Berenfeld and Shimon Abboud. Simulation of cardiac activity and the ECG using a heart model with a reaction-diffusion action potential. *Med. Eng. Phys.*, 18(8):615–625, 1996.

[22] O. Bernus, B. van Eyck, H. Verschelde, and A. V. Panfilov. Transition from ventricular fibrillation to ventricular tachycardia: a simulation study on the role of Ca^{2+}-channel blockers in human ventricular tissue. *Phys. Med. Biol.*, 47:4167–4179, 2002.

[23] O. Bernus, R. Wilders, C. W. Zemlin, H. Verschelde, and A. V. Panfilov. A computationally efficient electrophysiological model of human ventricular cells. *Am. J. Physiol. Heart Circ. Physiol.*, 282:H2296–H2308, 2002.

[24] Olivier Bernus, Henri Verschelde, and Alexander V. Panfilov. Modified ionic models of cardiac tissue for efficient large scale computations. *Phys. Med. Biol.*, 47(11):1947–1959, 2002.

[25] R. Beyar and S. Sideman. A computer study of the left ventricular performance based on fiber structure, sarcomere dynamics, and transmural electrical propagation velocity. *Circ. Res.*, 55:358–375, 1984.

[26] Martin Biermann, Mohammad Shenasa, Martin Borggrefe, Gerhard Hindricks, Wilhelm Haverkamp, and Günter Breithardt. The interpretation of cardiac electrograms. In Mohammad Shenasa, Martin Borggrefe, and Günter Breithardt, editors, *Cardiac Mapping*, chapter 2. Blackwell, Oxford, UK, second edition, 2003.

[27] Martin J. Bishop and G. Plank. Bidomain ECG simulations using an augmented monodomain model for the cardiac source. *IEEE Trans. Biomed. Eng.*, 58:2297–2307, 2011.

[28] Martin J. Bishop and Gernot Plank. Representing cardiac bidomain bath-loading effects by an augmented monodomain approach: Application to complex ventricular models. *IEEE Trans. Biomed. Eng.*, 58:1066–1075, 2011.

[29] Oumayma Bouhamama, Mark Potse, Lisl Weynans, and Laura Bear. A patchwork method to improve the performance of current methods for solving the inverse problem of electrocardiography. *IEEE Trans. Biomed. Eng.*, 70:55–66, 2023.

[30] Martin Buist, Gregory Sands, Peter Hunter, and Andrew Pullan. A deformable finite element derived finite difference method for cardiac activation problems. *Ann. Biomed. Eng.*, 31:577–588, 2003.

[31] Martin L. Buist and Andrew J. Pullan. The effect of torso impedance on epicardial and body surface potentials: A modeling study. *IEEE Trans. Biomed. Eng.*, 50(7):816–824, 2003.

[32] Hassaan A. Bukhari, Flavio Palmieri, Julia Ramírez, Pablo Laguna, José Esteban Ruiz, Dina Ferreira, Mark Potse, Carlos Sánchez, and Esther Pueyo. Characterization of T wave amplitude, duration and morphology changes during hemodialysis: Relationship with serum electrolyte levels and heart rate. *IEEE Trans. Biomed. Eng.*, 68:2467–2478, 2021.

[33] Hassaan A. Bukhari, Carlos Sánchez, Mark Potse, Pablo Laguna, and Esther Pueyo. Monitoring of serum potassium and calcium levels in end-stage renal disease patients by ECG depolarization morphology analysis. *Sensors*, 22:2951, 2022.

[34] Hassaan A. Bukhari, Carlos Sánchez, Sabarathinam Srinivasan, Flavio Palmieri, Mark Potse, Pablo Laguna, and Esther Pueyo. Estimation of potassium levels in hemodialysis patients by T wave nonlinear dynamics and morphology markers. *Comp. Biol. Med.*, 143:105304, 2022.

[35] T. F. Chan, E. Gallopoulos, V. Simoncini, T. Szeto, and C. H. Tong. A quasi-minimal residual variant of the Bi-CGStab algorithm for nonsymmetric systems. *SIAM J. Sci. Comput.*, 15(2):338–347, 1994.

[36] Fatemeh Chegini, Algiane Froehly, Ngoc Mai Monica Huynh, Luca Pavarino, Mark Potse, Simone Scacchi, and Martin Weiser. Efficient numerical methods for simulating cardiac electrophysiology with cellular resolution. In *10th International Conference on Computational Methods for Coupled Problems in Science and Engineering*, Chania, Greece, June 2023.

[37] Peng-Sheng Chen, Kenneth M. Moser, Walter P. Dembitsky, William R. Auger, Pat O. Daily, Constance M. Calisi, Stuart W. Jamieson, and Gregory K. Feld. Epicardial activation and repolarization patterns in patients with right ventricular hypertrophy. *Circulation*, 83:104–118, 1991.

[38] Pablo A. Chiale, Julio Przyblyski, Rubén A. Laiño, M. Susana Halpern, Rubén A. Sánchez, Alfredo Gabrieli, Marcelo V. Elizari, and Mauricio B. Rosenbaum. Electrocardiographic changes evoked by ajmaline in chronic chagas' disease without manifest myocarditis. *Am. J. Cardiol.*, 49:14–20, 1982.

[39] Masaomi Chinushi, Minoru Tagawa, Hidehiro Kasai, Takashi Washizuka, Akira Abe, Hiroshi Furushima, and Yoshifusa Aizawa. Correlation between the effective refractory period and activation-recovery interval calculated from the intracardiac unipolar

electrogram of humans with and without dl-sotalol treatment. *Jpn. Circ. J.*, 65:702–706, 2001.

[40] P. Colli-Franzone, L. Guerri, and C. Viganotti. Oblique dipole layer potentials applied to electrocardiology. *J. Math. Biol.*, 17:93–124, 1983.

[41] P. Colli Franzone, L. F. Pavarino, S. Scacchi, and B. Taccardi. Determining recovery times from transmembrane action potentials and unipolar electrograms in normal heart tissue. In F. B. Sachse and G. Seemann, editors, *Proceedings of the Functional Imaging and Modeling of the Heart conference*, volume 4466 of *Lecture Notes in Computer Science*, pages 139–149. Springer, 2007.

[42] P. Colli Franzone, L. F. Pavarino, S. Scacchi, and B. Taccardi. Monophasic action potentials generated by bidomain modeling as a tool for detecting cardiac repolarization times. *Am. J. Physiol. Heart Circ. Physiol.*, 293:H2771–2785, 2007.

[43] Piero Colli-Franzone, Luciano Guerri, and Bruno Taccardi. Modeling ventricular excitation: axial and orthotropic anisotropy effects on wavefronts and potentials. *Math. Biosci.*, 188:191–205, 2004.

[44] Piero Colli-Franzone, Luciano Guerri, Carla Viganotti, Emilio Macchi, Silvana Baruffi, Santa Spaggiari, and Bruno Taccardi. Potential fields generated by oblique dipole layers modeling excitation wavefronts in the anisotropic myocardium; comparison with potential fields elicited by paced dog hearts in a volume conductor. *Circ. Res.*, 51(3):330–346, 1982.

[45] Philippe Comtois and Alain Vinet. Resetting and annihilation of reentrant activity in a model of a one-dimensional loop of ventricular tissue. *Chaos*, 12(3):903–922, 2002.

[46] Chantal E. Conrath and Tobias Opthof. Ventricular repolarization: An overview of (patho)physiology, sympathetic effects and genetic aspects. *Prog. Biophys. Mol. Biol.*, 92(3):269–307, 2006.

[47] Ruben Coronel, Simona Casini, Tamara T. Koopmann, Francien J. G. Wilms-Schopman, Arie O. Verkerk, Joris R. de Groot, Zahurul Bhuiyan, Connie R. Bezzina, Marieke W. Veldkamp, André C. Linnenbank, Allard C. van der Wal, Hanno L. Tan, Pedro Brugada, Arthur A. M. Wilde, and Jacques M. T. de Bakker. Right ventricular fibrosis and conduction delay in a patient with clinical signs of Brugada syndrome: a combined electrophysiologic, genetic, histopathologic and computational study. *Circulation*, 112:2769–2777, 2005.

[48] Ruben Coronel, Jacques M. T. de Bakker, Francien J. G. Wilms-Schopman, Tobias Opthof, André C. Linnenbank, Charly N. Belterman, and Michiel J. Janse. Monophasic action potentials and activation recovery intervals as measures of ventricular action potential duration: Experimental evidence to resolve some controversies. *Heart Rhythm*, 3:1043–1050, 2006.

[49] Ruben Coronel, Tobias Opthof, Jacques M. de Bakker, and Michiel J. Janse. The downslope of a positive T-wave of a local electrogram reflects remote activity. *Heart Rhythm*, 4:121, 2006. (letter).

[50] Ruben Coronel, Mark Potse, Michel Haïssaguerre, Nicolas Derval, Mathilde R. Rivaud, Veronique M. F. Meijborg, Matthijs Cluijtmans, Mélèze Hocini, and Bastiaan J. Boukens. Why ablation of sites with Purkinje activation is antiarrythmic: The interplay between fast activation and arrhythmogenesis. *Front. Physiol.*, 12:648396, 2021.

[51] Domenico Corrado, Cristina Basso, Gianfranco Buja, Andrea Nava, Lino Rossi, and Gaetano Thiene. Right bundle branch block, right precordial ST-segment elevation, and sudden death in young people. *Circulation*, 103:710–717, 2001.

[52] Yves Coudière, Yves Bourgault, and Myriam Rioux. Optimal monodomain approximations of the bidomain equations used in cardiac electrophysiology. *Math. Models Methods Appl. Sci.*, 24(6):1115–1140, 2014.

[53] Marc Courtemanche, Rafael J. Ramirez, and Stanley Nattel. Ionic mechanisms underlying human atrial action potential properties: insights from a mathematical model. *Am. J. Physiol. Heart Circ. Physiol.*, 275:H301–H321, 1998.

[54] Jacques M. T. de Bakker, Richard N. W. Hauer, and Timothy A. Simmers. Activation mapping: Unipolar versus bipolar recording. In Douglas P. Zipes and José Jalife, editors, *Cardiac Electrophysiology: From Cell to Bedside*, chapter 94, pages 1068–1078. Saunders, Philadelphia, PA, second edition, August 1994.

[55] José Di Diego, Jonathan Cordeiro, Robert J. Goodrow, Jeffrey M. Fish, Andrew C. Zygmunt, Guillermo Pérez, Fabiana Scornik, and Charles Antzelevitch. Ionic and cellular basis for the predominance of the Brugada syndrome phenotype in males. *Circulation*, 106:2004–2011, 2002.

[56] M. Malal Diallo, Mark Potse, Rémi Dubois, and Yves Coudière. Solving the ECGI problem with known location of scar regions. In *Computing in Cardiology*, Rimini, 2020. Computing in Cardiology.

[57] Emmanuel Drouin, Flavien Charpentier, Chantal Gauthier, Karine Laurent, and Herve Le Marec. Electrophysiologic characteristics of cells spanning the left ventricular wall of human heart: Evidence for presence of M cells. *J. Am. Coll. Cardiol.*, 26:185–192, 1995.

[58] Josselin Duchateau, Mark Potse, and Rémi Dubois. Spatially coherent activation maps for electrocardiographic imaging. *IEEE Trans. Biomed. Eng.*, 64:1149–1156, 2017.

[59] Dirk Durrer, R. Th. van Dam, G. E. Freud, M. J. Janse, F. L. Meijler, and R. C. Arzbaecher. Total excitation of the isolated human heart. *Circulation*, 41(6):899–912, 1970.

[60] Igor R. Efimov, Richard A. Gray, and Bradley J. Roth. Virtual electrodes and deexcitation: New insights into fibrillation induction and defibrillation. *J. Cardiovasc. Electrophysiol.*, 11:339–353, 2000.

[61] Vladimir G. Fast and André G. Kléber. Block of impulse propagation at an abrupt tissue expansion: evaluation of the critical strand diameter in 2- and 3-dimensional computer models. *Cardiovasc. Res.*, 30:449–459, 1995.

[62] G. Fischer, B. Tilg, R. Modre, G. J. M. Huiskamp, J. Fetzer, W. Rucker, and P. Wach. A bidomain model based BEM–FEM coupling formulation for anisotropic cardiac tissue. *Ann. Biomed. Eng.*, 28:1229–1243, 2000.

[63] Jeffrey M. Fish and Charles Antzelevitch. Cellular and ionic basis for the sex-related difference in the manifestation of the Brugada syndrome and progressive conduction disease phenotypes. *J. Electrocardiol.*, 36 Suppl.:173–179, 2003.

[64] Andrea Frustaci, Silvia G. Priori, Maurizio Pieroni, Cristina Chimenti, Carlo Napolitano, Ilaria Rivolta, Tomasso Sanna, Fulvio Bellocci, and Matteo Antonio Russo. Cardiac histological substrate in patients with clinical phenotype of Brugada syndrome. *Circulation*, 112:3680–3687, 2005.

[65] L. Geerts, P. Bovendeerd, K. Nicolay, and T. Arts. Characterization of the normal cardiac myofiber field in goat measured with MR-diffusion tensor imaging. *Am. J. Physiol. Heart Circ. Physiol.*, 283:H139–H145, 2002.

[66] Lior Gepstein, Gal Hayam, and Shlomo A. Ben-Haim. Activation-repolarization coupling in the normal swine endocardium. *Circulation*, 96:4036–4043, 1997.

[67] David B. Geselowitz. On the theory of the electrocardiogram. *Proc. IEEE*, 77(6):857–876, 1989.

[68] David B. Geselowitz. Description of cardiac sources in anisotropic cardiac muscle; application of the bidomain model. *J. Electrocardiol.*, 25 Suppl.:65–67, 1992.

[69] Ali Gharaviri, Simone Pezzuto, Mark Potse, Sander Verheule, Giulio Conte, Rolf Krause, Ulrich Schotten, and Angelo Auricchio. Left atrial appendage electrical isolation reduces atrial fibrillation recurrences: a simulation study. *Circ. Arrhythm. Electrophysiol.*, 14:105–106, 2021.

[70] Ali Gharaviri, Mark Potse, Rolf Krause, Angelo Auricchio, and Ulrich Schotten. Effect of sodium channel blockade on the 3-dimensional substrate of atrial fibrillation: a simulation study. In *EHRA Congress*, Barcelona, March 2018.

[71] Ali Gharaviri, Mark Potse, Sander Verheule, Rolf Krause, Angelo Auricchio, and Ulrich Schotten. Epicardial fibrosis explains increased transmural conduction in a computer model of atrial fibrillation. In *Computing in Cardiology*, volume 43, pages 237–240, Vancouver, Canada, 2016.

[72] Ali Gharaviri, Sander Verheule, Jens Eckstein, Mark Potse, Rolf Krause, Angelo Auricchio, Nico H. L. Kuijpers, and Ulrich Schotten. Effect of Na^+ channel blockade on the three-dimensional substrate of atrial fibrillation in a model of endo-epicardial dissociation and transmural conduction. *Europace*, 20 Suppl. 3:iii69–iii76, 2018.

[73] Ali Gharaviri, Sander Verheule, Jens Eckstein, Mark Potse, Pawel Kuklik, Nico H. L. Kuijpers, and Ulrich Schotten. How disruption of endo-epicardial electrical connections enhances endo-epicardial conduction during atrial fibrillation. *Europace*, 19:308–316, 2017.

[74] Ali Gharaviri, Sander Verheule, Mark Potse, Nico H. L. Kuijpers, and Ulrich Schotten. A computer model of endo-epicardial electrical dissociation and transmural conduction during atrial fibrillation. *Europace*, 14 (Suppl. 5):v10–16, 2012.

[75] Kazutaka Gima and Yoram Rudy. Ionic current basis of electrocardiographic waveforms; A model study. *Circ. Res.*, 90:889–896, 2002.

[76] Sanjeev B. Goyal and David H. Spodick. Electromechanical dysfunction of the left atrium associated with interatrial block. *Am. Heart J.*, 142:823–827, 2001.

[77] Larry S. Green, Bruno Taccardi, Philip R. Ershler, and Robert L. Lux. Epicardial potential mapping: Effects of conducting media on isopotential and isochrone distributions. *Circulation*, 84:2513–2521, December 1991.

[78] Ramesh M. Gulrajani. *Bioelectricity and Biomagnetism*. Wiley, New York, NY, 1998.

[79] Ramesh M. Gulrajani and Guy E. Mailloux. A simulation study of the effects of torso inhomogeneities on electrocardiographic potentials, using realistic heart and torso models. *Circ. Res.*, 52:45–56, 1983.

[80] Michel Haïssaguerre, Mélèze Hocini, Ghassen Cheniti, Josselin Duchateau, Frédéric Sacher, Stéphane Puyo, Hubert Cochet, Masateru Takigawa, Arnaud Denis, Ruairid Martin, Nicolas Derval, Pierre Bordachar, Philippe Ritter, Sylvain Ploux, Thomas Pambrun, Nicolas Klotz, Gregoire Massoullié, Xavier Pillois, Corentin Dallet, Jean-Jacques Schott, Solena Le Scouarnec, Michael J. Ackerman, David J. Tester, Olivier Piot, Jean-Luc Pasquié, Christophe Leclerc, Jean-Sylvain Hermida, Estelle Gandjbakhch, Philippe Maury, Louis Labrousse, Ruben Coronel, Pierre Jais, David Benoist, Edward Vigmond, Mark Potse, Richard Walton, Koonlawee Nademanee, Olivier Bernus, and Rémi Dubois. Localized structural alterations underlying a subset of unexplained sudden cardiac death. *Circ. Arrhythm. Electrophysiol.*, 11:e006120, 2018.

[81] Michel Haïssaguerre, Koonlawee Nademanee, Ghassen Cheniti, Mélèze Hocini, Josselin Duchateau, Antonio Frontera, Frédéric Sacher, Nicolas Derval, Arnaud Denis, Thomas Pambrun, Rémi Dubois, Pierre Jaïs, David Benoist, Richard D. Walton, Akihiko Nogami, Ruben Coronel, Mark Potse, and Olivier Bernus. Depolarization versus repolarization abnormality underlying inferolateral J-wave syndromes: New concepts in sudden cardiac death with apparently normal hearts. *Heart Rhythm*, 16:781–790, 2019.

[82] Rasmus Havmoller, Jonas Carlson, Fredrik Holmqvist, Alberto Herreros, Carl J. Meurling, Bertil Olsson, and Pyotr Platonov. Age-related changes in P wave morphology in healthy subjects. *BMC Cardiovasc. Disord.*, 7:22, 2007.

[83] Charles W. Haws and Robert L. Lux. Correlation between in vivo transmembrane action potential durations and activation-recovery intervals from electrograms. Effects of interventions that alter repolarization time. *Circulation*, 81:281–288, 1990.

[84] Craig S. Henriquez. Simulating the electrical behavior of cardiac tissue using the bidomain model. *CRC Crit. Rev. Biomed. Eng.*, 21:1–77, 1993.

[85] Craig S. Henriquez, Adam L. Muzikant, and Charles K. Smoak. Anisotropy, fiber curvature, and bath loading effects on activation in thin and thick cardiac tissue preparations: Simulations in a three-dimensional bidomain model. *J. Cardiovasc. Electrophysiol.*, 7:424–444, 1996.

[86] Craig S. Henriquez, Joseph V. Tranquillo, David Weinstein, Edward W. Hsu, and Christopher R. Johnson. Three-dimensional propagation in mathematic models: Integrative model of the mouse heart. In Douglas P. Zipes and José Jalife, editors, *Cardiac Electrophysiology; From Cell To Bedside*. Saunders, Philadelphia, PA, 4th edition, 2004.

[87] Bertil Hille. *Ion Channels of Excitable Membranes*. Sinauer Associates, Inc, Sunderland, MA, USA, 2001.

[88] S. Y. Ho and D. Sánchez-Quintana. The importance of atrial structure and fibers. *Clinical Anatomy*, 22:52–63, 2009.

[89] Siew Yen Ho, Robert H. Anderson, and Damián Sánchez-Quintana. Atrial structure and fibres: morphologic bases of atrial conduction. *Cardiovasc. Res.*, 54:325–336, 2002.

[90] Mélèze Hocini, Siew Y. Ho, Tokuhiro Kawara, André C. Linnenbank, Mark Potse, Dipen Shah, Pierre Jaïs, Michiel J. Janse, Michel Haïssaguerre, and Jacques M. T. de Bakker. Electrical conduction in canine pulmonary veins: Electrophysiological and anatomic correlation. *Circulation*, 105:2442–2448, 2002.

[91] A. L. Hodgkin and A. F Huxley. A quantitative description of membrane current and its application to conduction and excitation in nerve. *J. Physiol.*, 117:500–544, 1952.

[92] A. L. Hodgkin and W. A. H. Rushton. The electrical constants of a crustacean nerve fibre. *Proc. Roy. Soc. Lond. B*, 133(873):444–479, 1946.

[93] M. Hoke, B. Ross, R. Wickesberg, and B. Lütkenhöner. Weighted averaging – theory and application to electric response audiometry. *Electroenceph. and Clin. Neurophysiol.*, 57:484–489, 1984.

[94] Fredrik Holmqvist, Daniela Husser, Jari M. Tapanainen, Jonas Carlson, Raija Jurkko, Yunlong Xia, Rasmus Havmöller, Ole Kongstad, Lauri Toivonen, S. Bertil Olsson, and Pyotr G. Platonov. Interatrial conduction can be accurately determined using standard 12-lead electrocardiography: Validation of P-wave morphology using electroanatomic mapping in man. *Heart Rhythm*, 5:413–418, 2008.

[95] Fredrik Holmqvist, Pyotr Platonov, Jonas Carlson, Wojciech Zareba, Arthur J. Moss, and the MADIT II Investigators. Altered interatrial conduction detected in MADIT II patients bound to develop atrial fibrillation. *Ann. Noninvasive Electrocardiol.*, 14:268–275, 2009.

[96] Mark G. Hoogendijk, Mark Potse, and Ruben Coronel. Critical appraisal of the mechanism underlying J waves. *J. Electrocardiol.*, 46:390–394, 2013.

[97] Mark G. Hoogendijk, Mark Potse, André C. Linnenbank, Arie O. Verkerk, Hester M. den Ruijter, Shirley C. M. van Amersfoorth, Eva C. Klaver, Leander Beekman, Connie R. Bezzina, Pieter G. Postema, Hanno L. Tan, Annette G. Reimer, Allard C. van der Wal, Arend D. J. ten Harkel, Michiel Dalinghaus, Alain Vinet, Arthur A. M. Wilde, Jacques M. T. de Bakker, and Ruben Coronel. Mechanism of right precordial ST-segment elevation in structural heart disease: Excitation failure by current-to-load mismatch. *Heart Rhythm*, 7:238–248, 2010.

[98] Mark G. Hoogendijk, Mark Potse, Alain Vinet, Jacques M. T. de Bakker, and Ruben Coronel. ST-segment elevation by current-to-load mismatch: An experimental and computational study. *Heart Rhythm*, 8:111–118, 2011.

[99] Rok Hren and B. Milan Horáček. Value of simulated body surface potential maps as templates in localizing sites of ectopic activation for radiofrequency ablation. *Physiol. Meas.*, 18:373–400, 1997.

[100] Geertjan Huiskamp. Simulation of depolarization in a membrane-equations-based model of the anisotropic ventricle. *IEEE Trans. Biomed. Eng.*, 45(7):847–855, 1998.

[101] Yan Huo, Fredrik Holmqvist, Jonas Carlson, Thomas Gaspar, Gerhard Hindricks, Christopher Piorkowski, Andreas Bollmann, and Pyotr G. Platonov. Variability of P-wave morphology predicts the outcome of circumferential pulmonary vein isolation in patients with recurrent atrial fibrillation. *J. Electrocardiol.*, 48:218–225, 2015.

[102] S. Jesus and H. Rix. High resolution ECG analysis by an improved signal averaging method and comparison with a beat-to-beat approach. *J. Biomed. Eng*, 10:25–32, 1988.

[103] Tomoyuki Kabutoya, Shizukiyo Ishikawa, Joji Ishikawa, Satoshi Hoshide, Kazuomi Kario, and the JMS Cohort Study Investigators Group. P-wave morphologic characteristics predict cardiovascular events in a community-dwelling population. *Ann. Noninvasive Electrocardiol.*, 17:252–259, 2012.

[104] Michał Kania, Yves Coudière, Hubert Cochet, Pierre Jaïs, and Mark Potse. Prediction of the exit site of ventricular tachycardia based on different ECG lead systems. In Christine Pickett, Cristiana Corsi, Pablo Laguna, and Rob MacLeod, editors, *Computing in Cardiology*, volume 44, Rennes, France, 2017.

[105] Victoriya Kashtanova, Ibrahim Ayed, Andony Arrieula, Mark Potse, Patrick Gallinari, and Maxime Sermesant. Deep learning approach for cardiac electrophysiology model correction. In *Medical Imaging with Deep Learning*, July 2022.

[106] Ruth Nicholson Klepfer, Christopher R. Johnson, and Robert S. MacLeod. The effects of inhomogeneities and anisotropies on electrocardiographic fields: A 3-D finite-element study. *IEEE Trans. Biomed. Eng.*, 44(8):706–719, 1997.

[107] Paul Kligfield, Leonard S. Gettes, James J. Bailey, Rory Childers, Barbara J. Deal, E. William Hancock, Gerard van Herpen, Jan A. Kors, Peter Macfarlane, David M. Mirvis, Olle Pahlm, Pentti Rautaharju, and Galen S. Wagner. Recommendations for the standardization and interpretation of the electrocardiogram; Part I: The electrocardiogram and its technology; A scientific statement from the American Heart Association Electrocardiography and Arrhythmias Committee, Council on Clinical Cardiology; the American College of Cardiology Foundation; and the Heart Rhythm Society. *Heart Rhythm*, 4:394–412, 2007.

[108] Paul Kligfield and Peter M. Olgin. Prevalence and clinical implications of improper filter settings in routine electrocardiography. *Am. J. Cardiol.*, 99:711–713, 2007.

[109] Dorian Krause, Mark Potse, Thomas Dickopf, Rolf Krause, Angelo Auricchio, and Frits W. Prinzen. Hybrid parallelization of a large-scale heart model. In Rainer Keller, David Kramer, and Jan-Philipp Weiss, editors, *Facing the Multicore-Challenge II*, volume 7174 of *Lecture Notes in Computer Science*, pages 120–132, Berlin, 2012. Springer.

[110] Martin W. Krueger, Kawal Rhode, Frank M. Weber, David U. J. Keller, Dennis Caulfield, Gunnar Seemann, Benjamin R. Knowles, Reza Razavi, and Olaf Dössel. Patient-specific volumetric atrial models with electrophysiological components: A comparison of simulations and measurements. *Biomed. Tech.*, 55 (Suppl. 1):54–57, 2010.

[111] P. Langley and A. Murray. Analysis of the atrial repolarisation phase of the electrocardiogram in health and in atrial fibrillation. *Computers in Cardiology*, 34:785–788, 2007.

[112] Theo A. R. Lankveld, Stef Zeemering, Harry J. G. M. Crijns, and Ulrich Schotten. The ECG as a tool to determine atrial fibrillation complexity. *Heart*, 100:1077–1084, 2014.

[113] I. J. Legrice, P. J. Hunter, and B. H. Smaill. Laminar structure of the heart: a mathematical model. *Am. J. Physiol. Heart Circ. Physiol.*, 272:H2466–H2476, 1997.

[114] L. Joshua Leon and B. Milan Horáček. Computer model of excitation and recovery in the anisotropic myocardium. I. Rectangular and cubic arrays of excitable elements. *J. Electrocardiol.*, 24(1):1–15, 1991.

[115] M. D. Lesh, M. Pring, and J. F. Spear. Cellular uncoupling can unmask dispersion of action potential duration in ventricular myocardium. A computer modeling study. *Circ. Res.*, 65(5):1426–1440, 1989.

[116] Gui-Rong Li, Jianlin Feng, Lixia Yue, and Michel Carrier. Transmural heterogeneity of action potentials and I_{to1} isolated from the human right ventricle. *Am. J. Physiol. Heart Circ. Physiol.*, 275:H369–H377, 1998.

[117] G. T. Lines, M. L. Buist, P. Grøttum, A. J. Pullan, J. Sundnes, and A. Tveito. Mathematical models and numerical methods for the forward problem in cardiac electrophysiology. *Comput. Vis. Sci.*, 5:215–239, 2003.

[118] Glenn Terje Lines, Per Grøttum, and Aslak Tveito. Modeling the electrical activity of the heart; A bidomain model of the ventricles embedded in a torso. *Comput. Vis. Sci.*, 5:195–213, 2003.

[119] Michel Lorange and Ramesh M. Gulrajani. A computer heart model incorporating anisotropic propagation: I. Model construction and simulation of normal activation. *J. Electrocardiol.*, 26(4):245–261, 1993.

[120] Ching-Hsing Luo and Yoram Rudy. A dynamic model of the cardiac ventricular action potential; I. Simulations of ionic currents and concentration changes. *Circ. Res.*, 74(6):1071–1096, jun 1994.

[121] Peter W. Macfarlane, Charles Antzelevitch, Michel Haissaguerre, Heikki V. Huikuri, Mark Potse, Raphael Rosso, Frederic Sacher, Jani T. Tikkanen, Hein Wellens, and Gan-Xin Yan. The early repolarization pattern; a consensus paper. *J. Am. Coll. Cardiol.*, 66:470–477, 2015.

[122] Peter W. Macfarlane and T. D. Veitch Lawrie. The normal electrocardiogram and vectorcardiogram. In Peter W. Macfarlane, Adriaan van Oosterom, Michiel Janse, Paul Kligfield, John Camm, and Olle Pahlm, editors, *Comprehensive Electrocardiology*, volume 2. Springer, 2012.

[123] Robert S. MacLeod, Bruno Taccardi, and Robert L. Lux. The influence of torso inhomogeneities on epicardial potentials. In *Computers in Cardiology*, pages 793–796, Piscataway, NJ, 1994. IEEE Press.

[124] R. E. McAllister, D. Noble, and R. W. Tsien. Reconstruction of the electrical activity of cardiac Purkinje fibres. *J. Physiol.*, 251:1–59, 1975.

[125] Richard McFee and Franklin D. Johnston. Electrocardiographic leads; I. introduction. *Circulation*, 8:554–568, 1953.

[126] Veronique M. F. Meijborg, Mark Potse, Chantal E. Conrath, Charly N. W. Belterman, Jacques M. T. de Bakker, and Ruben Coronel. Reduced sodium current in the lateral ventricular wall induces inferolateral J-waves. *Front. Physiol.*, 7:365, 2016.

[127] Carlos Mendez, William J. Mueller, John Merideth, and Gordon K. Moe. Interaction of transmembrane potentials in canine Purkinje fibers and at Purkinje fiber-muscle junctions. *Circ. Res.*, 24:361–372, 1969.

[128] Marianna Meo, Mark Potse, Stéphane Puyo, Laura Bear, Mélèze Hocini, Michel Haïssaguerre, and Rémi Dubois. Non invasive assessment of spatiotemporal organization

of ventricular fibrillation through principal component analysis. In Christine Pickett, Cristiana Corsi, Pablo Laguna, and Rob MacLeod, editors, *Computing in Cardiology*, volume 44, Rennes, France, September 2017.

[129] Paola G. Meregalli, Arthur A. M. Wilde, and Hanno L. Tan. Pathophysiological mechanisms of Brugada syndrome: Depolarization disorder, repolarization disorder, or more? *Cardiovasc. Res.*, 67(3):367–378, 2005. (review).

[130] C. Kay Millar, Fany A. Kralios, and Robert L. Lux. Correlation between refractory periods and activation-recovery intervals from electrograms: effects of rate and adrenergic interventions. *Circulation*, 72:1372–1379, 1985.

[131] Walter T. Miller, III and David B. Geselowitz. Simulation studies of the electrocardiogram; I. The normal heart. *Circ. Res.*, 43(2):301–315, 1978.

[132] Walter T. Miller, III and David B. Geselowitz. Simulation studies of the electrocardiogram; II. ischemia and infarction. *Circ. Res.*, 43(2):315–323, 1978.

[133] Toshihisa Miyazaki, Hideo Mitamura, SHunichiro Miyoshi, Kyoko Soejima, Yoshifusa Aizawa, and Satoshi Ogawa. Autonomic and antiarrhythmic drug modulation of ST segment elevation in patients with Brugada syndrome. *J. Am. Coll. Cardiol.*, 27:1061–1070, 1996.

[134] M. Mohr and B. Vanrumste. Comparing iterative solvers for linear systems associated with the finite difference discretisation of the forward problem in electroencephalographic source analysis. *Med. Biol. Eng. Comput.*, 41:75–84, 2003.

[135] Adam L. Muzikant and Craig S. Henriquez. Paced activation mapping reveals organization of myocardial fibers: A simulation study. *J. Cardiovasc. Electrophysiol.*, 8:281–294, 1997.

[136] Adam L. Muzikant and Craig S. Henriquez. Bipolar stimulation of a three-dimensional bidomain incorporating rotational anisotropy. *IEEE Trans. Biomed. Eng.*, 45(4):449–462, 1998.

[137] Adam L. Muzikant, Edward W. Hsu, Patrick D. Wolf, and Craig S. Henriquez. Region specific modeling of cardiac muscle: Comparison of simulated and experimental potentials. *Ann. Biomed. Eng.*, 30:867–883, 2002.

[138] Satoshi Nagase, Kengo Fukushima Kusano, Hiroshi Morita, and Tohru Ohe. Reply: Repolarization measurement in Brugada syndrome. *J. Am. Coll. Cardiol.*, 52:674–675, 2008. (letter).

[139] Uyên Châu Nguyên, Mark Potse, François Regoli, Maria Luce Caputo, Giulio Conte, Romina Murzilli, Stefano Muzzarelli, Tiziano Moccetti, Frits W. Prinzen, Rolf Krause, and Angelo Auricchio. An in-silico analysis of the effect of heart position and orientation on the ECG morphology and vectorcardiogram parameters in patients with heart failure and intraventricular conduction defects. *J. Electrocardiol.*, 48:617–625, May 2015.

[140] Bjørn Fredrik Nielsen, Tomas Syrstad Ruud, Glenn Terje Lines, and Aslak Tveito. Optimal monodomain approximations of the bidomain equations. *Appl. Math. Comput.*, 184:276–290, 2007.

[141] Denis Noble and Yoram Rudy. Models of cardiac ventricular action potentials: iterative interaction between experiment and simulation. *Phil. Trans. Roy. Soc. London; Phys. Sc.*, 359:1127–1142, 2001.

[142] Masahiro Ogawa, Koichiro Kumagai, Marta Vakulenko, Tomoo Yasuda, Carin Siegerman, Alan Garfinkel, Peng-Sheng Chen, and Keijiro Saku. Reduction of P-wave duration and successful pulmonary vein isolation in patients with atrial fibrillation. *J. Cardiovasc. Electrophysiol.*, 18:931–938, 2007.

[143] Michele Orini, Peter Taggart, and Pier D. Lambiase. In-vivo human sock-mapping validation of a simple model that explains unipolar electrogram morphology in relation to conduction-repolarization dynamics. *J. Cardiovasc. Electrophysiol.*, 29:990–997, 2018.

[144] Jiapu Pan and Willis J. Tompkins. A real-time QRS detection algorithm. *IEEE Trans. Biomed. Eng.*, 32(3):230–236, March 1985.

[145] Elisa Passini, Oliver J. Britton, Hua Rong Lu, Jutta Rohrbacher, An N. Hermans, David J. Gallacher, Robert J. H. Greig, Alfonso Bueno-Orovio, and Blanca Rodriguez. Human *In Silico* drug trials demonstrate higher accuracy than animal models in predicting clinical pro-arrhythmic cardiotoxicity. *Front. Physiol.*, 8:668, 2017.

[146] Heidi A. P. Peeters, Arne SippensGroenewegen, Eric F. D. Wever, Mark Potse, Marcel C. G. Daniëls, Cornelis A. Grimbergen, Richard N. W. Hauer, and Etienne O. Robles de Medina. Electrocardiographic identification of abnormal ventricular depolarization and repolarization in patients with idiopathic ventricular fibrillation. *J. Am. Coll. Cardiol.*, 31(6):1406–1413, May 1998.

[147] Heidi A. P. Peeters, Arne SippensGroenewegen, Eric F. D. Wever, Hemanth Ramanna, André C. Linnenbank, Mark Potse, Cornelis A. Grimbergen, Norbert M. van Hemel, Richard N. W. Hauer, and Etienne O. Robles de Medina. Clinical application of an integrated 3-phase mapping technique for localization of the site of origin of idiopathic ventricular tachycardia. *Circulation*, 99:1300–1311, March 1999.

[148] R. Christian Penland, David M. Harrild, and Craig S. Henriquez. Modeling impulse propagation and extracellular potential distributions in anisotropic cardiac tissue using a finite volume element discretization. *Comput. Visual. Sci*, 4:215–226, 2002.

[149] A. Peper, R. Jonges, T. G. Losekoot, and C. A. Grimbergen. Recording of surface His-Purkinje potentials. *Med. Biol. Eng. Comput.*, 23(4):365–376, 1985.

[150] Stefan Peters, Martina Trümmel, Stefan Denecke, and Brigitte Koehler. Results of ajmaline testing in patients with arrhythmogenic right ventricular dysplasia cardiomyopathy. *Int. J. Cardiol.*, 95:207–210, 2004.

[151] Simone Pezzuto, Peter Kaľavský, Mark Potse, Frits W. Prinzen, Angelo Auricchio, and Rolf Krause. Evaluation of a rapid fully anisotropic model for ECG simulation. *Front. Physiol.*, 8:265, 2017.

[152] H. V. Pipberger, R. C. Arzbaecher, A. S. Berson, S. A. Briller, D. A. Brody, N. C. Flowers, D. B. Geselowitz, E. Lepeschkin, G. C. Oliver, O. H. Schmitt, and M. Spach. Recommendations for standardization of leads and specifications for instruments in electrocardiography and vectorcardiography. *Circulation*, 52 Suppl.:11–31, 1975.

[153] Gernot Plank, L. Joshua Leon, Shane Kimber, and Edward J. Vigmond. Defibrillation depends on conductivity fluctuations and the degree of disorganization in reentry patterns. *J. Cardiovasc. Electrophysiol.*, 16:205–216, 2005.

[154] Gernot Plank, Lufang Zhou, Joseph L. Greenstein, Sonia Cortassa, Raimond L. Winslow, Brian O'Rourke, and Natalia A. Trayanova. From mitochondrial ion channels to arrhythmias in the heart: computational techniques to bridge the spatio-temporal scales. *Phil. Trans. Roy. Soc. A.*, 366:3381–3409, 2008.

[155] Pyotr G. Platonov. P-wave morphology: Underlying mechanisms and clinical implications. *Ann. Noninvasive Electrocardiol.*, 17:161–169, 2012.

[156] R. Plonsey and D. Fleming. *Bioelectric Phenomena*. McGraw-Hill, New York, 1969.

[157] Robert Plonsey and Roger C. Barr. Current flow patterns in two-dimensional anisotropic bisyncytia with normal and extreme conductivities. *Biophys. J.*, 45:557–571, 1984.

[158] Andrew E. Pollard, Mary Jo Burgess, and Kenneth W. Spitzer. Computer simulations of three-dimensional propagation in ventricular myocardium; effects of intramural fiber rotation and inhomogeneous conductivity on epicardial activation. *Circ. Res.*, 72(744–756), 1993.

[159] M. Potse, R. Hoekema, A. C. Linnenbank, A. SippensGroenewegen, J. Strackee, J. M. T. de Bakker, and C. A. Grimbergen. Conversion of left ventricular endocardial positions from patient-independent co-ordinates into biplane fluoroscopic projections. *Med. Biol. Eng. Comput.*, 40(1):41–46, 2002.

[160] Mark Potse. Subendocardial ischemia must be global or severe to cause significant primary ST depression in the ECG. In *36th Int. Con. Electrocardiol.*, Wroclaw, Poland, June 2009. (abstract).

[161] Mark Potse. Scalable and accurate ECG simulation for reaction-diffusion models of the human heart. *Front. Physiol.*, 9:370, 2018.

[162] Mark Potse, Luca Cirrottola, and Algiane Froehly. A practical algorithm to build geometric models of cardiac muscle structure. In *8th European Congress on Computational Methods in Applied Sciences and Engineering (ECCOMAS)*, Oslo, Norway, June 2022.

[163] Mark Potse, Ruben Coronel, Stéphanie Falcao, A.-Robert LeBlanc, and Alain Vinet. The effect of lesion size and tissue remodeling on ST deviation in partial-thickness ischemia. *Heart Rhythm*, 4(2):200–206, 2007.

[164] Mark Potse, Ruben Coronel, A.-Robert LeBlanc, and Alain Vinet. Modeling transport of interstitial potassium in regional myocardial ischemia: effect on the injury current. In *Proc. 29th Annu. Int. Conf. IEEE EMBS*, pages 6330–6333, Lyon, France, 2007.

[165] Mark Potse, Ruben Coronel, A.-Robert LeBlanc, and Alain Vinet. The role of extracellular potassium transport in computer models of the ischemic zone. *Med. Biol. Eng. Comput.*, 45(12):1187–1199, 2007.

[166] Mark Potse, Ruben Coronel, Tobias Opthof, and Alain Vinet. The positive T wave. *Anatol. J. Cardiol.*, 7 Suppl. 1:164–167, 2007. (Proc. 34th Int. Con. Electrocardiol.).

[167] Mark Potse, Ruben Coronel, Tobias Opthof, and Alain Vinet. Simulating T-wave parameters of local extracellular electrograms with a whole-heart bidomain reaction-diffusion model: Size matters! In *Proc. 29th Annu. Int. Conf. IEEE EMBS*, pages 6644–6647, Lyon, France, 2007.

[168] Mark Potse, Bruno Dubé, Jacques Richer, Alain Vinet, and Ramesh M. Gulrajani. A comparison of monodomain and bidomain reaction-diffusion models for action potential propagation in the human heart. *IEEE Trans. Biomed. Eng.*, 53(12):2425–2435, 2006.

[169] Mark Potse, Bruno Dubé, and Alain Vinet. Cardiac anisotropy in boundary-element models for the electrocardiogram. *Med. Biol. Eng. Comput.*, 47:719–729, 2009.

[170] Mark Potse, Dorian Krause, Ljuba Bacharova, Rolf Krause, Frits W. Prinzen, and Angelo Auricchio. Similarities and differences between ECG signs of left bundle branch block and left-ventricular uncoupling. *Europace*, 14 (Suppl. 5):v33–v39, 2012.

[171] Mark Potse, Dorian Krause, Wilco Kroon, Romina Murzilli, Stefano Muzzarelli, François Regoli, Enrico Caiani, Frits W. Prinzen, Rolf Krause, and Angelo Auricchio. Patient-specific modelling of cardiac electrophysiology in heart-failure patients. *Europace*, 16:iv56–iv61, 2014.

[172] Mark Potse, Theo A. R. Lankveld, Stef Zeemering, Pieter C. Dagnelie, Coen D. A. Stehouwer, Ronald M. Henry, André C. Linnenbank, Nico H. L. Kuijpers, and Ulrich Schotten. P-wave complexity in normal subjects and computer models. *J. Electrocardiol.*, 49:545–553, 2016.

[173] Mark Potse, André C. Linnenbank, and Cornelis A. Grimbergen. Software design for analysis of multichannel intracardial and body surface electrocardiograms. *Comp. Meth. Progr. Biomed.*, 69:225–236, 2002.

[174] Mark Potse, André C. Linnenbank, Heidi A. P. Peeters, Arne SippensGroenewegen, and Cornelis A. Grimbergen. Continuous localization of cardiac activation sites using a database of multichannel ECG recordings. *IEEE Trans. Biomed. Eng.*, 47(5):682–689, May 2000.

[175] Mark Potse, Emmanuelle Saillard, Denis Barthou, and Yves Coudière. Feasibility of whole-heart electrophysiological models with near-cellular resolution. In *Computing in Cardiology*, Rimini, September 2020. Computing in Cardiology.

[176] Mark Potse, Pascal F. H. M. van Dessel, André C. Linnenbank, Norbert M. van Hemel, Cornelis A. Grimbergen, and Jacques M. T. de Bakker. Properties of unipolar electrograms recorded with a multielectrode basket catheter. *J. Electrocardiol.*, 37:1–10, 2004.

[177] William H. Press, Saul A. Teukolsky, William T. Vetterling, and Brian P. Flannery. *Numerical Recipes in C; The Art of Scientific Computing*. Cambridge University Press, Cambridge, UK, second edition, 1992.

[178] Leo Priebe and Dirk J. Beuckelmann. Simulation study of cellular electric properties in heart failure. *Circ. Res.*, 82:1206–1223, 1998.

[179] Ingemar Ragnemalm. Neighborhoods for distance transformations using ordered propagation. *CVGIP: Image Understanding*, 56(3):399–409, 1992.

[180] Gwladys Ravon, Yves Coudière, Mark Potse, and Rémi Dubois. Impact of the endocardium in a parameter optimization to solve the inverse problem of electrocardiography. *Front. Physiol.*, 9:1946, 2019.

[181] Gwladys Ravon, Rémi Dubois, Yves Coudière, and Mark Potse. A parameter optimization to solve the inverse problem in electrocardiography. In Michaela Pop and Graham Wright, editors, *Functional Imaging and Modeling of the Heart*. Springer, June 2017.

[182] Blanca Rodríguez, Li Li, James C. Eason, Igor R. Efimov, and Natalia A. Trayanova. Differences between left and right ventricular chamber geometry affect cardiac vulnerability to electric shocks. *Circ. Res.*, 97:168–175, 2005.

[183] Stephan Rohr and B. M. Salzberg. Characterization of impulse propagation at the microscopic level across geometrically defined expansions of excitable tissue: Multiple site optical recording of transmembrane voltage (MSORTV) in patterned growth heart cell cultures. *J. Gen. Physiol.*, 104:287–309, 1994.

[184] J. P. Roos, R. Th. van Dam, and D. Durrer. Epicardial and intramural excitation of normal heart in six patients 50 years of age and older. *Br. Heart J.*, 30:630–637, 1968.

[185] Bradley J. Roth. Action potential propagation in a thick strand of cardiac muscle. *Circ. Res.*, 68:162–173, 1991.

[186] Bradley J. Roth. Electrical conductivity values used with the bidomain model of cardiac tissue. *IEEE Trans. Biomed. Eng.*, 44:326–328, 1997.

[187] Bradley J. Roth. Influence of a perfusing bath on the foot of the cardiac action potential. *Circ. Res.*, 86:e19–22, 2000.

[188] Stanley Rush and Hugh Larsen. A practical algorithm for solving dynamic membrane equations. *IEEE Trans. Biomed. Eng.*, 25(4):389–392, 1978.

[189] Yousef Saad. *Iterative Methods for Sparse Linear Systems*. PWS publishing, New York, 1996. Second edition published by SIAM, Philadelphia, 2003.

[190] Hasan I. Saleheen and Kwong T. Ng. New finite difference formulations for general inhomogeneous anisotropic bioelectric problems. *IEEE Trans. Biomed. Eng.*, 44(9):800–809, 1997.

[191] Carlos Sánchez, Gabriele D'Ambrosio, Francesco Maffessanti, Enrico G. Caiani, Frits W. Prinzen, Rolf Krause, Angelo Auricchio, and Mark Potse. Sensitivity analysis of ventricular activation and electrocardiogram in tailored models of heart-failure patients. *Med. Biol. Eng. Comput.*, 56:491–504, 2018.

[192] Betty I. Sasyniuk and Carlos Mendez. A mechanism for reentry in canine ventricular tissue. *Circ. Res.*, 28:3–15, 1971.

[193] Pierre Savard, René Cardinal, Réginald Nadeau, and J. Andrew Armour. Epicardial distribution of ST segment and T wave changes produced by stimulation of intrathoracic ganglia or cardiopulmonary nerves in dogs. *J. Auton. Nerv. Syst.*, 34:47–58, 1991.

[194] Otto H. Schmitt. Biological information processing using the concept of interpenetrating domains. In K. N. Leibovic, editor, *Information Processing in The Nervous System*, pages 325–331, New York, 1969. Springer.

[195] M. T. Schram, S. J. Sep, C. J. van der Kallen, P. C. Dagnelie, A. Koster, N. Schaper, R. M. Henry, and C.D. Stehouwer. The Maastricht Study: an extensive phenotyping study on determinants of type 2 diabetes, its complications and its comorbidities. *Eur. J. Epidemiol.*, 29:439–451, 2014.

[196] Peter Sonneveld. CGS, a fast Lanczos-type solver for nonsymmetric linear systems. *SIAM J. Sci. Stat. Comput.*, 10:35–52, 1989.

[197] Leif Sörnmo, Elin Trägøardh Johansson, and Michael B. Simson. The signal-averaged electrocardiogram. In Peter W. MacFarlane, Adriaan van Oosterom, Olle Pahlm, Paul Kligfield, Michiel Janse, and John Camm, editors, *Comprehensive Electrocardiology*, volume 4, pages 1793–1821. Springer, 2011.

[198] Madison S. Spach, Roger C. Barr, Gerald A. Serwer, J. Mailen Kootsey, and Edward A. Johnson. Extracellular potentials related to intracellular action potentials in the dog Purkinje system. *Circ. Res.*, 30(5):505–519, May 1972.

[199] Bruce M. Steinhaus. Estimating cardiac transmembrane activation and recovery times from unipolar and bipolar extracellular electrograms: A simulation study. *Circ. Res.*, 64(3):449–462, 1989.

[200] Daniel D. Streeter, Jr, Henry M. Spotnitz, Dali P. Patel, John Ross, and Edmund H. Sonnenblick. Fiber orientation in the canine left ventricle during diastole and systole. *Circ. Res.*, 24:339–347, 1969.

[201] Borys Surawicz and Satoshi Saito. Exercise testing for detection of myocardial ischemia in patients with abnormal electrocardiograms at rest. *Am. J. Cardiol.*, 41:943–951, 1978.

[202] Bruno Taccardi, Emilio Macchi, Robert L. Lux, Philip R. Ershler, Santa Spaggiari, Silvana Baruffi, and Yonild Vyhmeister. Effect of myocardial fiber direction on epicardial potentials. *Circulation*, 90:3076–3090, December 1994.

[203] Peter Taggart, Peter M. I. Sutton, Tobias Opthof, Ruben Coronel, Richard Trimlett, Wilfred Pugsley, and Panny Kallis. Transmural repolarisation in the left ventricle in humans during normoxia and ischaemia. *Cardiovasc. Res.*, 50:454–462, 2001.

[204] Nolwenn Tan, Laura Bear, Mark Potse, Stéphane Puyo, Marianna Meo, and Remi Dubois. Analysis of signal-averaged electrocardiogram performance for body surface recordings. In *Computing in Cardiology*, volume 46, Singapore, June 2019. Computing in Cardiology.

[205] K. H. W. J. ten Tusscher, D. Noble, P. J. Noble, and A. V. Panfilov. A model for human ventricular tissue. *Am. J. Physiol. Heart Circ. Physiol.*, 286:H1573–H1589, 2004.

[206] K. H. W. J. ten Tusscher and A. V. Panfilov. Alternans and spiral breakup in a human ventricular tissue model. *Am. J. Physiol. Heart Circ. Physiol.*, 291:H1088–H1100, 2006.

[207] Arun Thangamani, Tiago Trevisan Jost, Vincent Loechner, Stéphane Genaud, and Bérenger Bramas. Lifting code generation of cardiac physiology simulation to novel compiler technology. In *Proceedings of the 21st ACM/IEEE International Symposium on Code Generation and Optimization*, CGO 2023, pages 68–80, New York, NY, USA, February 2023. Association for Computing Machinery.

[208] Natalia Trayanova and Felipe Aguel. Computer simulations of cardiac defibrillation: a look inside the heart. *Comput. Vis. Sci.*, 4:259–270, 2002.

[209] Tiago Trevisan Jost, Arun Thangamani, Raphaël Colin, Vincent Loechner, Stéphane Genaud, and Bérenger Bramas. GPU code generation of cardiac electrophysiology simulation with MLIR. In José Cano, Marios D. Dikaiakos, George A. Papadopoulos, Miquel Pericàs, and Rizos Sakellariou, editors, *Euro-Par 2023: Parallel Processing*, pages 549–563, Cham, August 2023. Springer Nature Switzerland.

[210] Mark Trew, Ian Le Grice, Bruce Smaill, and Andrew Pullan. A finite volume method for modeling discontinuous electrical activation in cardiac tissue. *Ann. Biomed. Eng.*, 33(5):590–602, 2005.

[211] Marie-Claude Trudel, Bruno Dubé, Mark Potse, Ramesh M. Gulrajani, and L. Joshua Leon. Simulation of propagation in a membrane-based computer heart model with parallel processing. *IEEE Trans. Biomed. Eng.*, 51(8):1319–1329, 2004.

[212] Raymond Tukkie, Peter Sogaard, Jim Vleugels, Irma K. L. M. de Groot, Arthur A. M. Wilde, and Hanno L. Tan. Delay in right ventricular activation contributes to Brugada syndrome. *Circulation*, 109:1272–1277, 2004.

[213] Leslie Tung. *A Bi-Domain Model for Describing Ischemic Myocardial D-C Potentials*. PhD thesis, MIT, Cambridge MA, USA, 1978.

[214] H. A. van der Vorst. Bi-CGSTAB: A fast and smoothly converging variant of Bi-CG for the solution of nonsymmetric linear systems. *SIAM J. Sci. Stat. Comput.*, 13:631–644, 1992.

[215] Pascal F. H. M. van Dessel, Norbert M. van Hemel, Jacques M. T. de Bakker, André C. Linnenbank, Mark Potse, Emile R. Jessurun, Arne SippensGroenewegen, and Eric F. D. Wever. Relation between body surface mapping and endocardial spread of ventricular activation in postinfarction heart. *J. Cardiovasc. Electrophysiol.*, 12:1232–1241, 2001.

[216] A. van Oosterom. Genesis of the T wave as based on an equivalent surface source model. *J. Electrocardiol.*, 34 Suppl.:217–227, 2001.

[217] Adriaan van Oosterom and Vincent Jacquemet. Genesis of the P wave: Atrial signals as generated by the equivalent double layer source model. *Europace*, 7 Suppl 2:S21–S29, 2005.

[218] Harold V. M. van Rijen, Toon A. B. van Veen, Marjan J. A. van Kempen, Francien J. G. Wilms-Schopman, Mark Potse, Olaf Krueger, Klaus Willecke, Habo J. Jongsma, and Jacques M. T. de Bakker. Impaired conduction in the bundle branches of mouse hearts lacking the gap junction protein connexin40. *Circulation*, 103:1591–1598, 2001.

[219] Bernard Victorri, Alain Vinet, Fernand A. Roberge, and Jean-Pierre Drouhard. Numerical integration in the reconstruction of cardiac action potentials using Hodgkin–Huxley-type models. *Comp. Biomed. Res.*, 18:10–23, 1985.

[220] E. J. Vigmond, R. Weber dos Santos, A. J. Prassl, M. Deo, G. Plank, and S. Bauer. Solvers for the cardiac bidomain equations. *Prog. Biophys. Mol. Biol.*, 96:3–18, 2007.

[221] Edward J. Vigmond, Felipe Aguel, and Natalia A. Trayanova. Computational techniques for solving the bidomain equations in three dimensions. *IEEE Trans. Biomed. Eng.*, 49(11):1260–1269, 2002.

[222] Edward J. Vigmond, Vincent Tsoi, Ya-Lin Yin, Pierre Pagé, and Alain Vinet. Estimating atrial action potential duration from electrograms. *IEEE Trans. Biomed. Eng.*, 56:1546–1555, 2009.

[223] Alain Vinet, Dante R. Chialvo, Donald C. Michaels, and José Jalife. Nonlinear dynamics of rate-dependent activation in models of single cardiac cells. *Circ. Res.*, 67:1510–1524, 1990.

[224] Paul G. A. Volders, Karin R. Sipido, Edward Carmeliet, Roel L. H. M. G. Spätjens, Hein J. J. Wellens, and Marc A. Vos. Repolarizing K^+ currents I_{TO1} and I_{Ks} are larger in right than left canine ventricular midmyocardium. *Circulation*, 99:206–210, 1999.

[225] Galen S. Wagner. *Marriott's Practical Electrocardiography*. Williams & Wilkins, Baltimore, Maryland, USA, 9th edition, 1994.

[226] Rodrigo Weber dos Santos, Gernot Plank, Steffen Bauer, and Edward J. Vigmond. Parallel multigrid preconditioner for the cardiac bidomain model. *IEEE Trans. Biomed. Eng.*, 51(11):1960–1968, 2004.

[227] Daniel L. Weiss, Gunnar Seemann, and Olaf Dössel. The end of T wave need not coincide with final repolarization in tissue: a simulation study. *Heart Rhythm*, 4 Suppl.:S159, 2007. (abstract).

[228] David Western, Ben Hanson, and Peter Taggart. Measurement bias in activation-recovery intervals from unipolar electrograms. *Am. J. Physiol. Heart Circ. Physiol.*, 308:H331–338, 2015.

[229] John P. Wikswo, Todd A. Wisialowski, William A. Altemeier, Jeffrey R. Balser, Harry A. Kopelman, and Dan M. Roden. Virtual cathode effects during stimulation of cardiac muscle; two-dimensional in vivo experiments. *Circ. Res.*, 68:513–530, 1991.

[230] World Health Organization. World health statistics 2018. `http://www.who.int/whosis`, 2018.

[231] R. F. Wyatt, M. J. Burgess, A. K. Evans, R. L. Lux, J. A. Abildskov, and T. Tsutsumi. Estimation of ventricular transmembrane action potential durations and repolarization times from unipolar electrograms. *Am. J. Cardiol.*, 47 (Part II):488, 1981. (abstract).

[232] Gan-Xin Yan and Charles Antzelevitch. Cellular basis for the Brugada syndrome and other mechanisms of arrhythmogenesis associated with ST-segment elevation. *Circulation*, 100:1660–1666, 1999.

[233] Arthur M. Yue. The controversy over measurement of activation recovery intervals continues. *Heart Rhythm*, 4:120–121, 2006. (letter).

[234] Arthur M. Yue. Repolarization measurement in Brugada syndrome. *J. Am. Coll. Cardiol.*, 52:674, 2008. (letter).

[235] Arthur M. Yue, John R. Paisey, Steve Robinson, Tim R. Betts, Paul R. Roberts, and John M. Morgan. Determination of human ventricular repolarization by noncontact mapping; validation with monophasic action potential recordings. *Circulation*, 110:1343–1350, 2004.

[236] Nejib Zemzemi, Cecile Dobrzynski, Laura Bear, Mark Potse, Corentin Dallet, Yves Coudière, Remi Dubois, and Josselin Duchateau. Effect of the torso conductivity heterogeneities on the ECGI inverse problem solution. In *Computing in Cardiology*, volume 42, pages 233–236, Nice, France, 2015.

[237] Sven Zumhagen, Tilmann Spieker, Julia Rolinck, Hideo A. Baba, Günter Breithardt, Werner Böcker, Lars Eckhardt, Matthias Paul, Thomas Wichter, and Eric Schulze-Bahr. Absence of pathognomonic or inflammatory patterns in cardiac biopsies from patients with brugada syndrome. *Circ. Arrhythmia and Electrophysiol.*, 2:16–23, 2009.